DESIGN AND EXPERIMENTAL EVALUATION OF A DYNAMICALLY BALANCED OVER-CONSTRAINED PLANAR 6R PARALLEL MANIPULATOR

A Thesis Submitted to
the Graduate School of Engineering and Sciences of
İzmir Institute of Technology
in Partial Fulfillment of the Requirements for Degree of

MASTER OF SCIENCE

in Mechanical Engineering

by
Merve ÖZKAHYA

July 2019
İZMİR

We approve the thesis of **Merve ÖZKAHYA**

Examining Committee Members:

Assoc. Prof. Dr. Gökhan KİPER
Department of Mechanical Engineering, İzmir Institute of Technology

Prof. Dr. Serhan ÖZDEMİR
Department of Mechanical Engineering, İzmir Institute of Technology

Asst. Prof. Dr. Volkert van der Wijk
Department of Precision and Microsystems Engineering, Delft University of Technology

19 July 2019

Assoc. Prof. Dr. Gökhan KİPER
Supervisor, Department of Mechanical Engineering, İzmir Institute of Technology

Assoc. Prof. Dr. M. İ. Can DEDE
Co-Supervisor, Department of Mechanical Engineering, İzmir Institute of Technology

Prof. Dr. Sedat Akkurt
Head of the Department of Mechanical Engineering

Prof. Dr. Aysun SOFUOĞLU
Dean of the Graduate School of Engineering and Sciences

ACKNOWLEDGMENTS

First of all, I would like to thank my supervisor Dr. Gökhan Kiper for giving me opportunity to work in his laboratory when I was a 3rd year undergraduate student, and later for his patience, support and guidance during my thesis works. I also would like to thank my co-advisor Dr. M. İ. Can Dede for his attention, contributions in parts of this study. Furthermore, I am very thankful to Dr. Volkert van der Wijk for his contributions regarding my test studies.

I would like to thank the members of Rasim Alizade Mechatronics Laboratory and Robotic Laboratory for their help. A special thanks goes foremost to my project mate, Emre Uzunoğlu, who provided invaluable guidance, shared idea about all my works and motivated me when I lost my faith in myself.

I am extremely grateful to my family (Mrs. Sevda Özkahya, Mr. Özgür Özkahya and Ms. Tuğçe Özkahya) for their love, caring, understanding and sacrifices for educating and preparing me for my future. Their presence gave me strength in all circumstances and at any time.

This thesis study would not have been completed without the support of my dear friend, Mr. Bahadır Öztürk who was always there, and opened up his home when I had to work late.

I would like to especially thank to my friends who were with me during the thesis; Mr. Murat Demirel, Mr. N. Çağhan Kirişçi, Ms. Kadriye Çağla Dilsiz, Mrs. Gizem Ersavaş.

I wish to thank various people for their contribution to this thesis; Prof. Dr. Metin Tanoğlu and his research group, for their valuable technical support on the material tests; Prof. Dr. Alper Taşdemirci and Mr. Semih Berk Seven, for their help in offering us the use of measuring instruments; Prof. Dr. Serhan Özdemir for his supportive comments on the thesis.

I would also like to thank Dr. Tolga Doğan and Fibermak Composites Company for informing about and providing composite materials. I would like to extend my thanks

to Mr. Ender Koç from Bias Mühendislik Company for his help in finite element analysis studies and providing facilities of their office.

This project is financial supported by Turkish Scientific and Technological Research Council (TÜBİTAK) 1001 project with no. 116M272 and entitled “Methodologies for Increasing the Positioning Accuracy of High-Acceleration Parallel Robots Used in Industrial Applications”.

ABSTRACT

DESIGN AND EXPERIMENTAL EVALUATION OF A DYNAMICALLY BALANCED OVER-CONSTRAINED PLANAR 6R PARALLEL MANIPULATOR

With the development of the industry, the number of robots used in the production line is increasing day by day. Particularly, it is known that parallel robots are better in terms of positioning accuracy compared to serial robots based on the stretching of robot arms. In parallel mechanisms, there are many factors such as calibration, stability and dynamic balancing of the mechanism affecting positioning accuracy. The aim of this thesis is to dynamically balancing parallel mechanisms to improve positioning accuracy.

In high acceleration applications, the shaking force and moment are the factors that cause vibration in the base of the mechanism. These vibrations can be reduced by designing dynamically balanced mechanisms. In this thesis, over- and simply constrained 6R mechanisms are designed for dynamic balancing studies and prototypes are produced. The counter mass method was used to balance the mechanism dynamically. The design of the masses was made according to the mass information received from the model designed in the computer aided drawing program and the parts of the mechanisms were updated according to their actual mass values after they were produced. The design of the masses is designed according to the mass information from CAD model and the parts of the mechanisms are updated according to their actual mass values after they are produced.

Dimensional measurements were taken by FARO Prime Arm device due to faults that may arise from the production in the parts of the mechanism after production. Then the mechanism was assembled. Before carrying out the balancing tests, calibration studies affecting the positioning accuracy of the over-constrained mechanism were carried out. Finally, the mechanism is activated balanced and unbalanced and the acceleration effect of the 6-axis accelerometer is obtained experimentally.

ÖZET

DİNAMİK DENGELİ FAZLA KISITLI DÜZLEMSEL 6R MANİPÜLATÖRÜNÜN TASARIMI VE DENEYSEL ÖLÇÜMLERİ

Endüstrinin gelişmesi ile birlikte üretim hattında kullanılan robotların sayısı da günden güne artmaktadır. Özellikle paralel robotların konumlama hassasiyeti konusunda seri robotlara göre robot kollarında oluşan esnemeler baz alındığında daha iyi olduğu bilinmektedir. Paralel mekanizmalarda konumlama hassasiyetini etkileyen mekanizmanın kalibrasyonu, direngenliği, dinamik dengelenmesi gibi birçok faktör vardır. Bu tezin amacı da konumlama hassasiyetini geliştirmek için paralel mekanizmaların dinamik olarak dengelenmesidir.

Yüksek ivmeli uygulamalarda, sarsma kuvveti ve momenti mekanizmanın kaidesinde titreşime neden olan etkenlerdir. Bu titreşimler, dinamik dengeli mekanizmalar tasarlanarak azaltılabilir. Bu tez çalışmasında, fazla ve normal kısıtlı 6 kol paralel mekanizmaları dinamik dengeleme çalışmaları için tasarlanmış ve prototipleri üretilmiştir. Mekanizmayı dinamik dengelemek için karşıt kütle yöntemi kullanılmıştır. Kütlelerin tasarımı, mekanizmaların bilgisayar destekli çizim programında tasarlanan modelinden alınan kütle bilgisine göre tasarlanmış ve mekanizmaların parçaları üretildikten sonra gerçek kütle değerlerine göre güncellenmiştir.

Üretim sonrasında mekanizmanın uzuvlarında üretimden kaynaklanabilecek hatalar nedeniyle boyutsal ölçümler FARO Prime Arm cihazı ile alınmıştır. Daha sonra mekanizmanın montajı yapılmıştır. Dengeleme testlerine geçmeden önce fazla kısıtlı mekanizmanın konumlama hassasiyetine etki eden kalibrasyon çalışmaları gerçekleştirilmiştir. Son olarak fazla kısıtlı mekanizma dengelenmiş ve dengelenmemiş halde çalıştırılmış ve 6 eksen ivmeölçer ile kaideye etki eden titreşim bilgisi deneysel olarak elde edilmiştir.

TABLE OF CONTENTS

LIST OF FIGURES

Figure **Page**

Figure **Page**

Figure **Page**

Figure **Page**

Figure **Page**

LIST OF TABLES

Table **Page**

CHAPTER 1

INTRODUCTION

The Robot Institute of America (Todd, 1986) presents the term “industrial robot” as “a reprogrammable and multifunctional manipulator, devised for the transport of materials, parts, tools or specialized systems, with varied and programmed movements, with the aim of carrying out varied tasks”. George Devol designed the first industrial robot called as Unimate for a mechanical arm patented in 1954. In 1961, Joseph Engelberger established Unimation Inc company and presented the Unimate 1900 series (Figure 1.1) which was used to produce automotive parts on the product line of General Motors, and thus is the first mass produced robotic arm for factory automation (Engelberger, 1980).

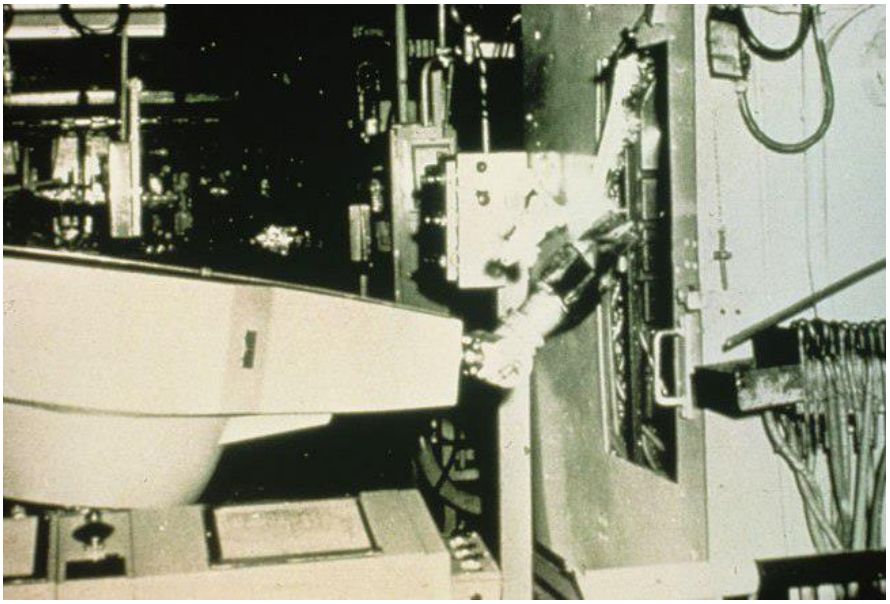

Figure 1.1. The first industrial robot, the Unimate at GM (General Motors).
(Source: International Federation of Robotics (IFR), Robot History, n.d.)

Robots can be classified according to several properties such as their degrees of freedom (dof), kinematic structure, workspace geometry, and motion characteristics (Tsai, 1999). According to kinematic structure, robots are investigated in two types: serial

robot which consists of an open loop chains (Figure 1.2 (a)) and parallel robot formed from closed-loop kinematic chains (Figure 1.2 (b)).

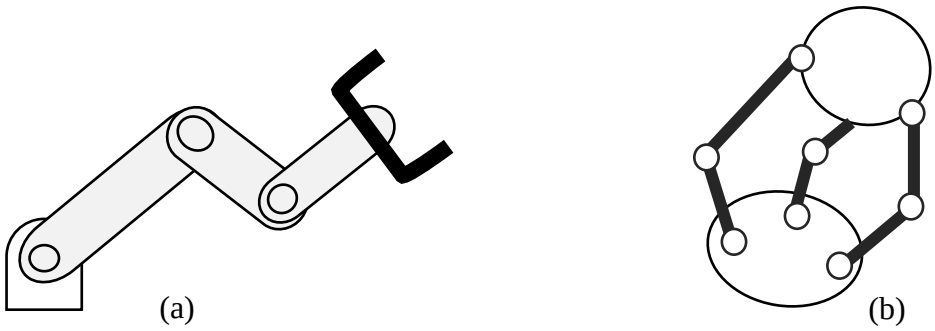

Figure 1.2. Schematic view of: (a) serial robot, (b) parallel robot.

Serial robots were utilized in the industry earlier and are more common than parallel robots. Some examples are presented in (Kurfess, 2005). The Versatran (Figure 1.3 (a)), the first cylindrical robot was produced by American Machine and Foundry at the Ford factory in 1962. The first commercially existing microcomputer controlled industrial robot, The Tomorrow Tool (Figure 1.3 (b)) was developed by Richard Hohn at Cincinnati Milacron Corporation in 1973. PUMA (Figure 1.3 (c)) was developed for assembly by Unimation and Vicarm with support of General Motors in the late 1970s.

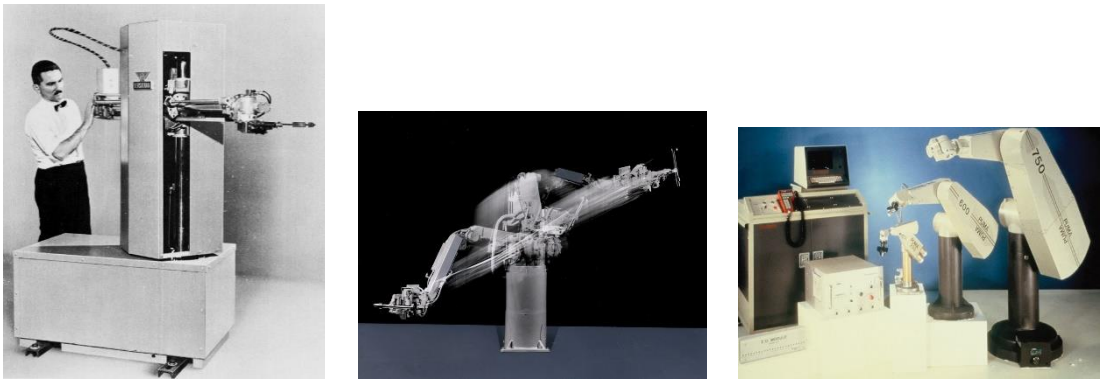

Figure 1.3. Earlier serial robot examples in the industry, (a) The Versatran (Source: Johnson and Milenkovic, 2013), (b) The Tomorrow Tool, T3 (Source: IFR, Robot History, n.d.), (c) PUMA (Source: IFR, Robot History, n.d.).

The first industrial parallel robot (Figure 1.4) was designed as a position controlling apparatus to hold a spray gun by Willard L. V. Pollard. The apparatus was

considered to require small amount of energy consumption and has a large workspace (Pollard, 1942). Although he received an acceptance from patent application in 1942, the parallel robot was never constructed.

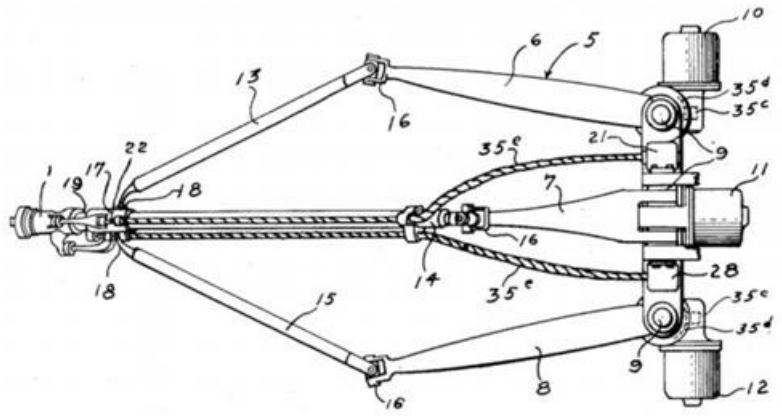

Figure 1.4. The first industrial parallel robot, spray gun apparatus, by Willard L. V. Pollard. (Source: Pollard, 1942)

In 1947, Gough demonstrated that a 6-dof parallel robot could perform the positioning and the orientating of the moving platform to test tire wear and tear. The moving platform has hexagonal shape and a ball-and-socket joint is used to attach links with all vertices of hexagonal platform. The other end of the link is connected to the fix platform by a universal joint. In 1955, Gough presented the first practical prototype of parallel robot (Figure 1.5) on the mentioned idea (Merlet, 2006).

The second precursor name is D. Stewart who presented an idea of the 6-dof parallel robot platform for a flight simulator in 1965 (Stewart, 1965). But the robot has a triangular platform (Figure 1.6 (a)) unlike Gough's platform and all vertices are connected to legs with spherical joints. Each leg is fixed to the ground by a universal joint. In the same years, Klaus Cappel studied an available conventional 6-dof vibration systems. He also developed the octahedral hexapod parallel robot as a motion simulator (Figure 1.6 (b)) and it was patented in 1967. Nowadays, Gough's platform is still used for flight simulators.

For a popular recent design of parallel by robot is proposed Clavel in 1990. The aim of the proposed robot is to have better repeatability of position than known industrial parallel robots to pick light weight at high speeds. It is called a delta robot and has three

dof which provides three translational movements. The parallelograms in Figure 1.7 (a) do not allow angular movements of the platforms (Clavel, 1990).

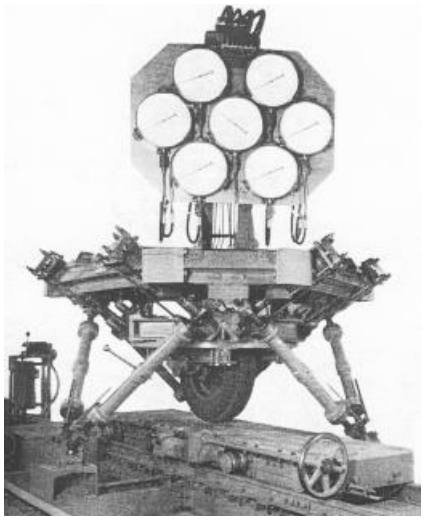

Figure 1.5. The first octahedral hexapod, Gough platform.
(Source: Merlet, 2006)

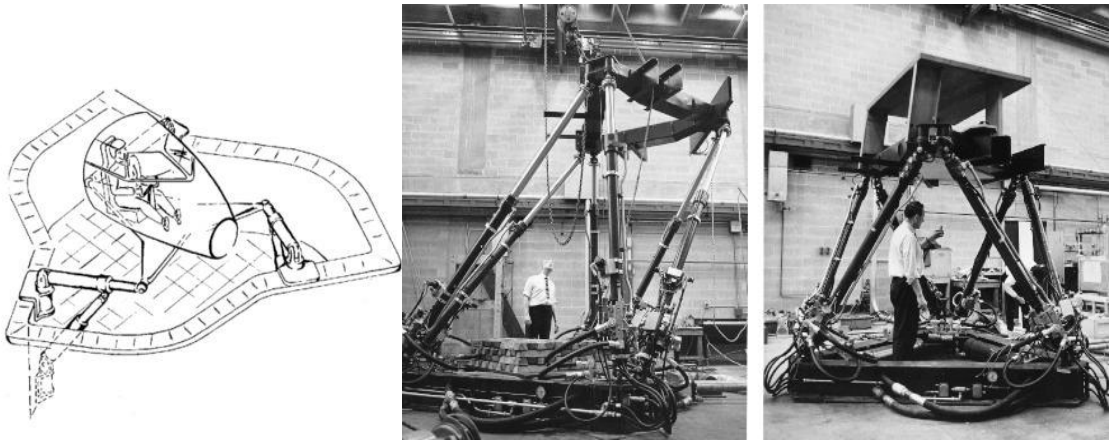

(a) (b)

Figure 1.6. The flight simulator by (a) Stewart (Source: Stewart, 1965), (b) Cappel (Source: Bonev, 2003).

Delta robots have been used in the industry for many purposes. Demaurex company used delta robots for four applications which are named as Pack-Placer, Line-Placer, Top-Placer, Presto. Elekta company manufactured a delta robot which carries a heavy (20 kg) microscope in surgical application (Bonev, 2001). In 1999, ABB Flexible Automation presented IRB 340 FlexPicker delta robot based on three sectors which are the food, pharmaceutical and electronics industries (Bonev, 2001). In 1999, ABB Flexible

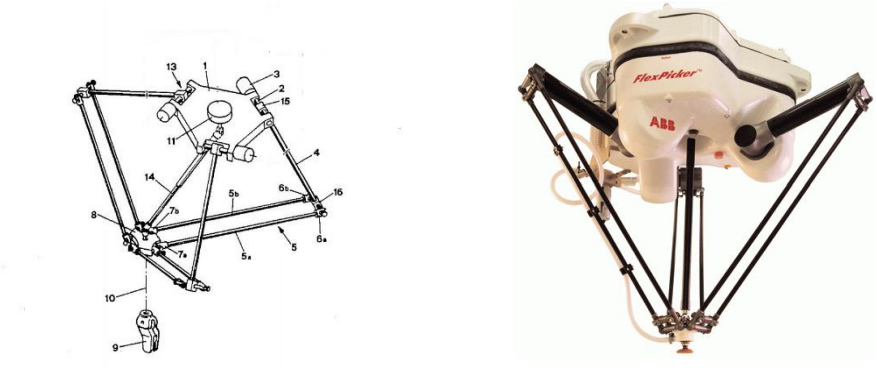

(a) (b)

Figure 1.7. (a) First patented Delta Robot by Clavel (Source: Clavel, 1990), (b) ABB FlexPicker (Source: Bonev, 2001).

Automation presented IRB 340 FlexPicker delta robot based on three sectors which are the food, pharmaceutical and electronics industries (Bonev, 2001). In 2000, the Krause&Mauser Group published a patent about a delta robot with linear drives to be used as a milling machine (Holy, 2000).

Parallel robots have more advantages than serial robots in terms of stiffness, high load/weight ratio, low inertia (Patel, 2012), the performance at high speed, positioning accuracy (Briot and Bonev, 2007). Because, parallel robot arms share the error caused by positioning accuracy or load carried by end-effector.

As can be seen from the given examples, the use of parallel robots in industry has started to become widespread in recent decades. It has also been the focus of academic studies. In the thesis, the design, manufacturing and testing of two different planar parallel robots are investigated to position the end-effector. Both planar parallel robots have a kinematic structure based on a 5-bar mechanism, but one of them has over-constrained kinematic structure, whereas the other has simply constrained kinematic structure.

Over-constrained mechanisms are the mechanisms which do not satisfy the Grübler-Kutzbach mobility criterion is as follows (Waldron, 1979):

$$F = \lambda(l - j - 1) + \sum_{i=1}^{i} f_i$$

where λ is the dof of space (λ=3 for planar and spherical space, λ=6 for spatial space), l is the number of links, j is the number of joints and f_i is the dof of the i^{th} joint.

The real dof of an over-constrained mechanism is more than the value computed with the mobility formula. An over-constrained parallelogram mechanism is shown in Figure 1.8 as an example. The mobility formula is as follows:

$$F = 3(5-6-1) + \sum_{i=1}^{6} 1 = 0$$

Although the dof is computed as 0, the mechanism actually works with 1-dof when the necessary parallelism condition is satisfied. Over-constrained mechanisms always possess a special geometrical condition.

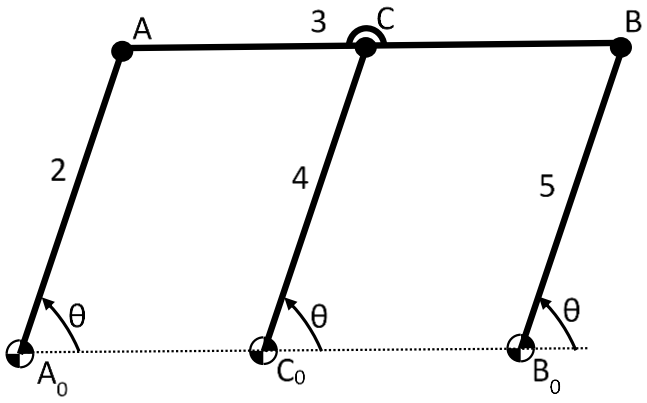

Figure 1.8. An over-constrained parallelogram mechanism.

1.1. Motivation of The Thesis

As mentioned in the previous section, serial robots have poor behaviour for positioning accuracy. On the other hand, parallel robots show better performance in terms of positioning accuracy under high load and high acceleration conditions. Therefore, use of parallel robots in the industry has increased. With the demand provided by this increase, studies on parallel robots have gained importance in industry and academia. Although it is known that parallel robots are a good option for positioning accuracy and high speed applications, there are several problems to be addressed to achieve the desired results in applications.

In order develop convenient methods for solving these problems, parallel robots should be evaluated in many subjects such as energy efficiency, ease of balancing,

positioning accuracy and repeatability, model complexity, controllability, and ease of calibration.

Another motivation of this thesis is to examine the simply constrained and over-constrained parallel mechanisms to be used in industrial applications, especially in terms of ease of balancing and their constructional design to increase the positioning accuracy of the end-effector.

1.2. Aim of The Thesis

The aim of the thesis is to investigate and device proper methodology to enhance positioning accuracy of a planar parallel mechanism. Regarding this, an over-constrained 2-dof planar mechanism is chosen for investigation with experimental studies. To achieve this, studies carried out in this thesis comprise of design, manufacturing, dynamic balancing and statical calibration of proposed mechanism. It is aimed to show the effects of balancing on mechanism by comparing the results between the unbalanced over-constrained mechanism and the balanced over-constrained mechanism.

The objectives of the thesis are as follows:

- To derive dynamic model of the mechanism
- To design and manufacture prototype of the mechanism
- To calibrate the mechanism
- To perform tests under static and dynamic conditions

In addition, the design criteria of the over-constrained 2-dof planar mechanism are determined as follows:

- The planar mechanism should have 2-dof to locate the end-effector point
- The workspace size: 100 mm x 150 mm rectangular workspace
- 5 g (g: gravitational acceleration) maximum acceleration of the end-effector point
- 5 kg payload positioned at the end-effector link

1.3. Outline of the Thesis

In the thesis, there are 7 Chapters: Introduction, Literature Survey, Determination of the Kinematic Structure and Dynamic Force Analysis of the Mechanism, CAD Model of the Mechanisms, Prototype of the Mechanisms, Tests and Conclusions.

In Chapter 2, literature review of planar 2-dof parallel robots and balancing of mechanisms are presented.

In Chapter 3, alternatives of 2-dof planar mechanism are evaluated with the studies in the literature. These alternatives are compared according to their advantages and disadvantages, which are suitable for the over- and simply constrained mechanisms. Kinematic and dynamic models are presented for the selected mechanisms.

In Chapter 4, the design of the mechanism parts is explained in groups along with their CAD models. Then, the assembly CAD model of the mechanisms are presented. Finally, the design of balancing masses is presented according to mass information obtained from the CAD models.

In Chapter 5, purchased and manufactured components are presented. The balancing masses are updated according to manufactured parts. Prototypes of the mechanisms are assembled and presented. Dimensional and mass measurements are taken from the produced parts in order to modify the parameters in the computer model.

In Chapter 6, calibration studies are performed on the over-constrained mechanism. Lastly, the setup and steps of balancing test are clarified, and the results are discussed in terms of vibrations measured on the base and the moving platform.

In Chapter 7, the results and potential further studies are discussed.

CHAPTER 2

LITERATURE SURVEY

This chapter includes a literature survey on theoretical and practical studies for especially planar 2-dof parallel manipulators. In addition, over-constrained mechanism examples and its properties are presented. Lastly, balancing of mechanisms and available prototypes of the balanced mechanisms are explained.

2.1. Planar 2-DoF Parallel Robots

The comparison of serial and parallel robots has been done in terms of workspace size, rigidity, positioning accuracy and speeds/forces in many theoretical studies. In these comparison studies usually 2-dof planar parallel manipulators are preferred due to their simpler structure compared to spatial manipulators with several dofs. Asada and Youcef-Toumi (1984), published a paper about analysis and design of a five-bar linkage as an alternative for 2-dof serial robots. They mentioned that a serial robot has motors at each joint. For 2-dof serial robots, the weight of second motor is carried by the first motor. Also, the reaction torque which is created by the second motor, affects the first motor. The planar five-bar parallel robot has two motors which can be fixed to the base. Therefore, it is found as a better solution instead of the serial robot. After that dynamic analysis and experiments that are made with the prototype, a lower dissipation of power is obtained compared to the serial robot under the same conditions (the same motors and workspace).

McCloy (1990) also compared a serial manipulator with two different parallel manipulators in terms of workspace, dynamic behaviour (speeds, forces and power) and stiffness. RR (R: revolute joint) is selected as a serial manipulator, whereas RRRPR and RRRRR planar five-bar linkages are selected as parallel manipulators. The results show that RR has larger stiffness; RRRPR consumes the least amount of power but RRRRR has similar power dissipation to it; RRRRR has larger workspace. Wenger et al. (1999) compared topologies of planar serial and parallel mechanisms to be used for machine

tools with regards to some performance criteria. RR and PP serial mechanisms and Biglide (PRRRP), Bipod (PRRRP) and five-bar (RRRRR) parallel mechanisms are selected to be examined. In terms of accuracy, load carrying capacity and working at high speed, 5R linkage has better performance than the other mechanisms.

Kumar (1992) investigated a planar 5-R linkage (as an example for parallel robot) from the point of special configurations which bring about a singularity in the control algorithm. The special configuration means that the mechanism gains or loses one or more dof when it passes through the configuration. Wide range of special configurations, which is associated with uncertainty and stationary singularities, is obtained. Screw theory is used to improve a general method for the instantaneous kinematic analysis of robot types. The method is utilized to find the singularity points.

Alıcı also implemented a method on planar parallel five-bar linkage to obtain singularity configurations (2000). As a result, a practical approach is proposed for trajectory planning and design of the mechanism to develop its workspace. Zhou and Ting (2005), presented a study about path generation without singularity for five-bar slider-crank parallel manipulators (RRRPR) (an underlined joint means that the joint is actuated). They show that if link length dimensions and slider input range are conveniently selected, singularities are not seen in the workspace or the singularities can be prevented via proper path generation process.

Gao et al. (1998) presented a solution to see relationship between the link lengths of 2-dof planar parallel manipulators and performance criteria for control of the manipulator. The solution is based on the global performance index which was previously defined by Gosselin and Angeles (1991).

Alıcı (2002) proposed a method to perform inverse kinematics of a five-bar planar parallel manipulator for the control in joint space and trajectory planning. The method is based on Sylvester's dialytic elimination method which reduces a system of equations to a single variable polynomial.

Cervantes et al. (2010) worked on the control design of a five-bar parallel robot (RRRRR). The control design is taken into consideration with trajectory planning and singularity avoidance. It is modeled as a nonlinear dynamic optimization problem which is solved using a constraint-handling differential evolution algorithm.

Liu et al. (2004) presented a novel 2-dof translational manipulator in terms of kinematic/dynamic analysis and dimensional synthesis. The mechanism is based on a PRRRP kinematic structure together with two parallelogram loops (Figure 2.1 (a)). The mechanism has two translational dof and the orientation is kept constant due to the parallelogram loops. A prototype of the manipulator (Figure 2.1 (b)) was built as a machine tool at Tsinghua University.

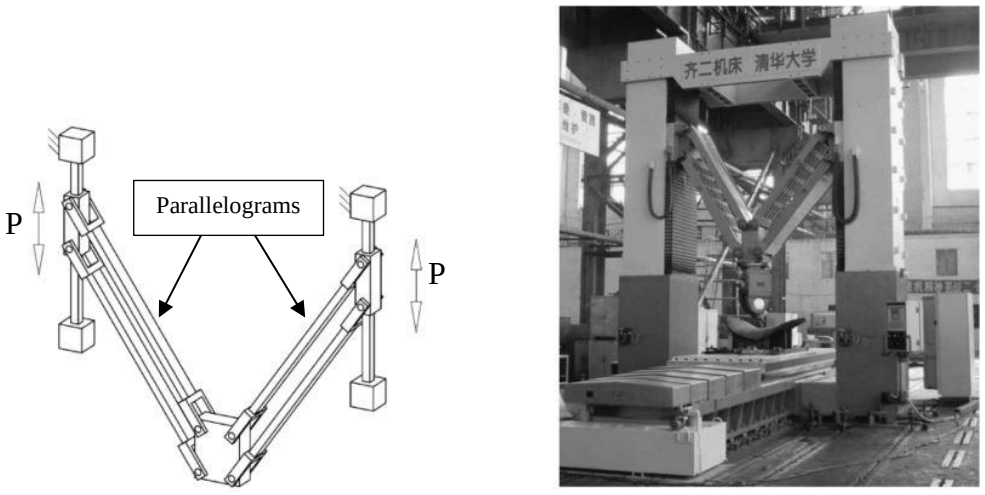

(a) (b)

Figure 2.1. 2-dof translational manipulator's, (a) Kinematic structure, (b) prototype by Tsinghua University (Source: Liu et al., 2004).

In another study (Wang et al., 2015) is published on the dynamic characteristics of a 2-DOF redundant parallel manipulator which has same kinematic structure with the mentioned robot in (Liu et al., 2004). The manipulator is redundant because of extra set of links attached between the base and the platform (Figure 2.2). The dynamic characteristics are investigated with the natural frequency and displacement response to compare the redundant parallel manipulator with its non-redundant version in the similar physical condition. The results of simulation demonstrate that the redundant parallel manipulator has higher the natural frequency and smaller displacement responses compared to its non-redundant version.

Mitsubishi Electric introduced the RP series micro working robot which is called as double-SCARA robot in the literature (Figielski, 2007). There are three types of RP series robots which are RP-1AH, RP-3AH, RP-5AH (Figure 2.3 (a)-(b)) and they are different from each other in terms of load capacity, arm lengths and workspace. The robot

are used for micro-assembly and process applications in the industry. The RP-5AH type robot is investigated to develop its optimal workspace by Figielski (2007). Distal links and proximal links of the RP-5AH robot have different size and hence that the workspace has holes. An approach based on switching working modes is used to cross Type-1 singularities (the end-effector loses one or more dof) for obtaining optimal workspace. Therefore, they proposed that all link lengths of the mechanism should be equal each other.

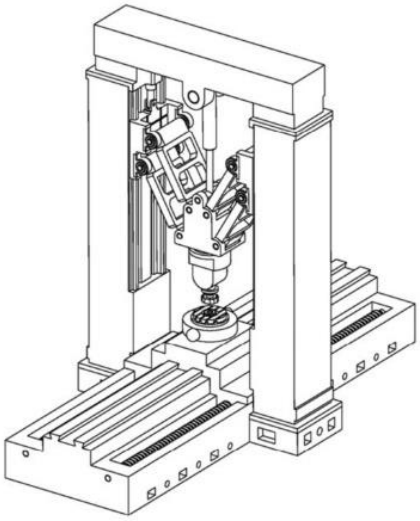

Figure 2.2. The 2-DOF redundant parallel manipulator.
(Source: Wang et al., 2015)

DexTAR was proposed to see the results in practice in (Compas et al., 2010). DexTAR (RRRRR) has same link lengths for four links as mentioned before. CAD model (Figure 2.4 (a)) and design details can be found in (Compas et al., 2010). A prototype of DexTAR (Figure 2.4 (b)) was manufactured to show effects of use of switching working modes approach (presented in (Figielski, 2007). The experimental results on the prototype show that the approach provides an approximately 30% increase in workspace compared to RP-5AH. Kinematic calibration method using all working modes (Joubair et al.,2012) and minimum-time trajectory planning and control of DexTAR (Bourbonnais et al., 2015) are also presented.

The Parvus miniaturized robot (Figure 2.5) has the same kinematic structure with DexTAR, but, it has very small workspace because it is designed for micro-production lines. The most significant thing is positioning accuracy of the Parvus. Burisch et al.

(2007) indicate the development of the Parvus in terms of drive system, mechanical design, analysis of workspace and control system.

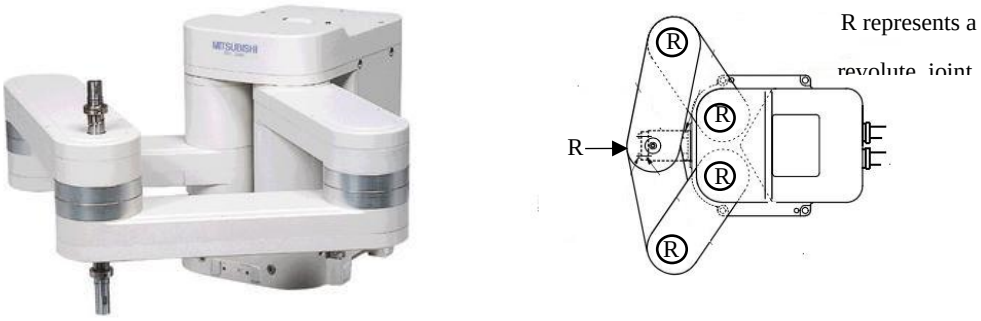

(a) (b)

Figure 2.3. (a) Mitsubishi Electric RP series robot; (b) schematic view of the robot. (Source: Standard Specifications Manual, n.d.)

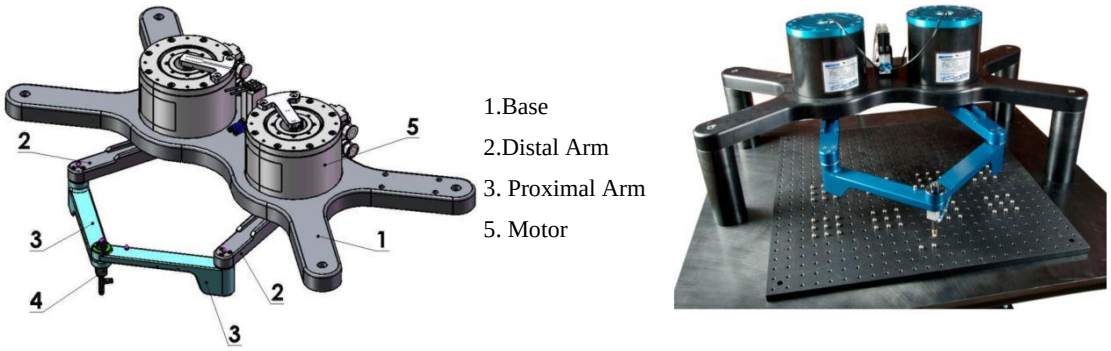

(a) (b)

Figure 2.4. (a) CAD model of DexTAR; (b) prototype of DexTAR. (Source: Compas et al., 2010)

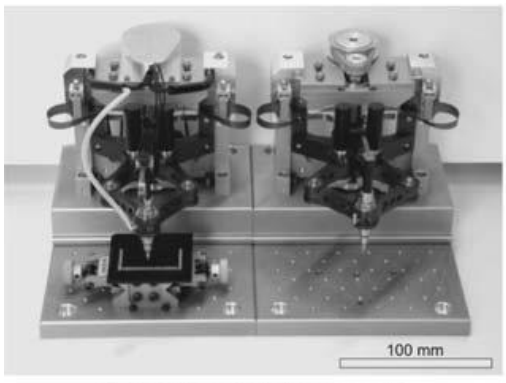

Figure 2.5. Parvus-miniaturized robot. (Source: Burisch et al., 2007)

The five-bar linkage can be modified with addition of parallelogram loops to construct a planar version of a Delta robot, which is named as a Diamond robot (Figure 2.6 (a)). Huang et al. studied trajectory planning of this robot to minimize operation time (Huang et al., 2007) and presented an approach for the optimal control design (Huang et al., 2015). The approach is formulated as a multi-objective optimization problem which is performed based on dynamic performance indices and angular constraints.

A mechanism proposed as an alternative to Diamond robot has four RR chains (Figure 2.6 (b)) between the base and the platform instead of two RR chains (Pierrot et al., 2011). Two of the chains are actuated and others are passive. The passive chains support the platform to work in a plane and reduce the vibration in the perpendicular direction. The mechanism is called as Par2 and its prototype is built for some experiments. The results show that it can work at an acceleration of 400 m/s^2 and is ten times stiffer than the available mechanisms.

Li-xin and Yong-gang (2014) examined joint clearance effects on the dynamic performance of a Diamond robot. In this work, it is shown that the joint clearance influences the dynamic behaviour of the manipulator such as vibration and dynamic accuracy of the end-effector. Two methods are proposed to decrease effect of the joint clearance which are to use a preload springs between the distal link and the proximal link and to develop variation of the inertial load for avoidance of “separation-leap-impact” situations with using a convenient kinematic law.

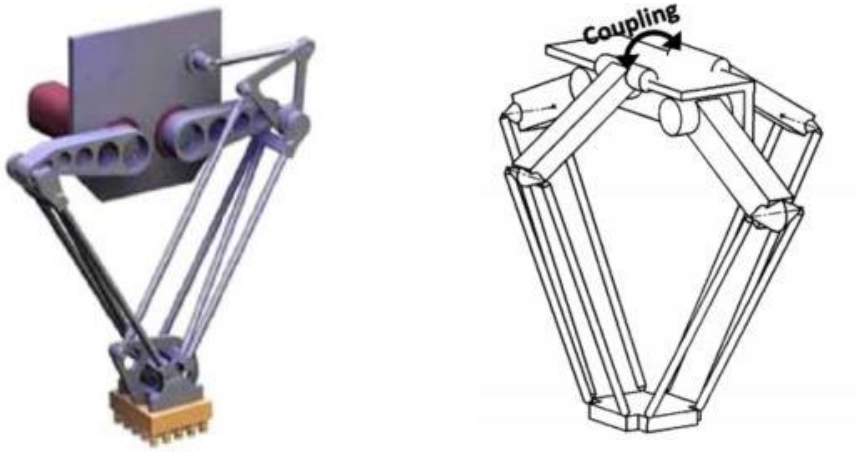

(a) (b)

Figure 2.6. (a) Dimond (Delta) robot; (b) Par2 robot.
(Source: Pierrot et al., 2011)

Helm et al. (2006) patented a planar parallel manipulator for planar positioning. The manipulator is called the PARAPLACER and has PRRRP kinematic structure (Figure 2.7). The PARAPLACER aims to perform assembly tasks at high speed. Its prototype is established at IWF (Institute of Machine Tools and Production Technology). A new approach for getting larger workspace for the PARAPLACER is published (Hesseleach et al., 2003). In this approach the tool center point passes through singularities rather than avoiding the singularities.

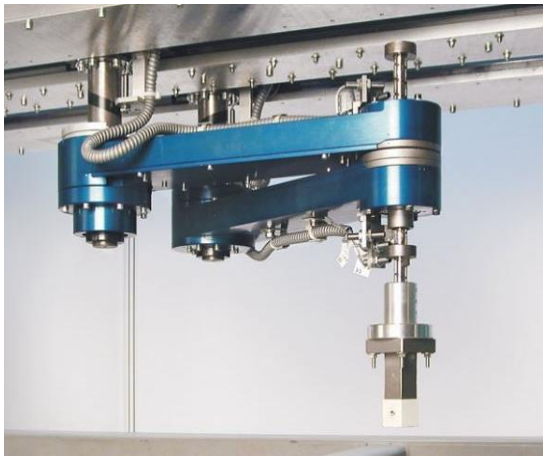

Figure 2.7. The PARAPLACER.
(Source: Hesseleach et al., 2003)

Brooks Automation Inc. supplies double-SCARA arm parallel robots to the industry. These robots have different configurations in terms of connection of the two arms. They are used in some application like tool automation in semiconductor water processing, flat panel display production. MagnaTran7 (Cox et al., 2011) and MagnaTran8 (Pietrantonio et al., 2013) are presented with details of their design and advantages (Figure 2.8). These robots have direct-drive technology and this provides advantages to reduce vibration, backlash and to increase positional repeatability.

Several studies have been presented for improvements in conventional laser cutting machines. Dede et al. (2013) searched on kinematically redundant planar laser cutting machine. It is pointed out that conventional planar laser cutting machine cannot achieve high acceleration values. It is necessary to reduce inertial forces while preserving the desired precision values. Kinematically redundant hybrid mechanisms (macro-micro mechanism) have been developed commercially in order to achieve high acceleration motion.

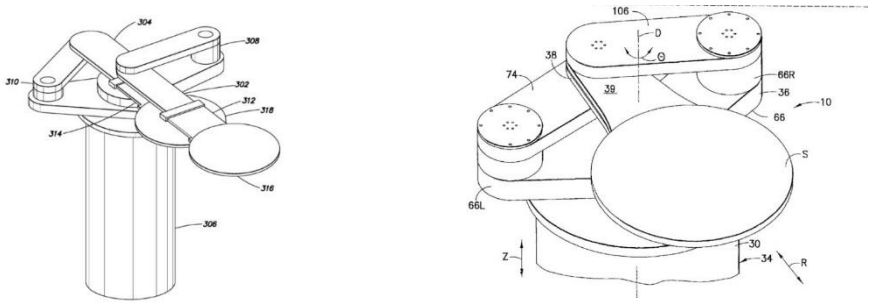

(a) (b)

Figure 2.8. Double-SCARA arm parallel robots supplied by Brook Automation Inc: (a) MagnaTran7 (Source: Cox et al., 2011), (b) MagnaTran8 (Source: Pietrantonio et al., 2013).

An asymmetric planar 5R mechanism (Figure 2.9) was proposed in order to easily connect the end-effector to one of the distal links (Kiper et al., 2015). Firstly, kinematic model of the mechanism is obtained to determine the workspace and the transmission angle was selected as a performance index to determine the dexterous workspace. Then determination of link lengths is explained according to the obtained dexterous workspace. Lastly, it is was observed that as the transmission angle moves away from 90^0, the torque value needed to perform same task is increased.

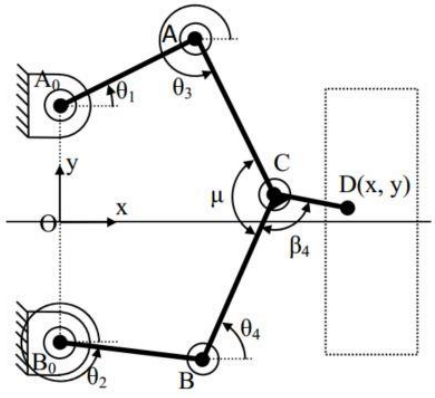

Figure 2.9. The planar 5R mechanism.
(Source: Kiper et al., 2015)

A new micro mechanism (Figure 2.10) was proposed for laser cutting applications in (Dede et al., 2016). It is a 2-dof over-constrained 6R mechanism that has parallelogram loops to keep the platform orientation constant. If one of the parallelogram loops is

removed, the mechanism becomes simply constrained. This paper is generally composed of design of the over-constrained 6R mechanism, calibration process of macro-micro mechanism, trajectory planning algorithm and benchmark tests. At the end of the studies, maximum acceleration of 3.5 g, positioning accuracy of ±37 μm/m and repeatability of ±26 μm are obtained. In addition, it was found that the task completion duration is decreased by 6 times compared to the conventional machines.

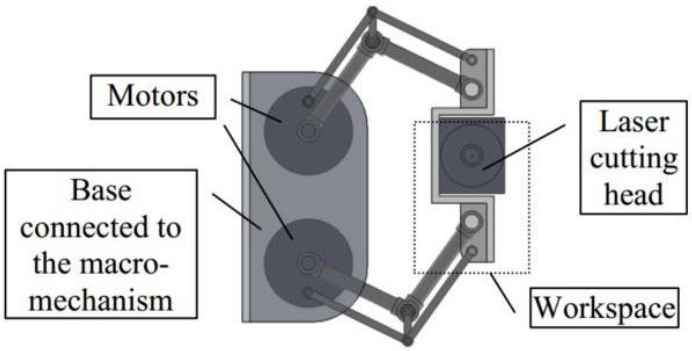

Figure 2.10. The over-constrained 6R mechanism CAD model.
(Source: Dede et al., 2016)

2.2. Balancing of Mechanisms

Balancing of machinery is a common problem for high-speed machinery. Balancing can be examined in two types which are static balancing and dynamic balancing. If the potential energy of the system is stationary at all times when the system is under the effect of a conservative force, it is said to be a statically balanced system (Ebert-Uphoff et al., 2000). When resultant of reaction forces and moments of the system due to inertial forces and moments are zero, the system can be said to be dynamically balanced. If reaction forces are zero, the system is called as shaking force balanced system. On the other hand, if reaction moments are zero, the system called as shaking moment balanced system (Wijk, 2014). A dynamically balanced system is already statically balanced.

For dynamically unbalanced mechanisms, undesired vibrations occur due to reaction forces acting on the base during the operation. The mentioned vibrations can lead to undesired results in applications which require high precision. For this reason, the

reaction forces of the mechanisms are aimed to be decreased or reduced to zero in order to eliminate vibrations.

In the literature, there are some balancing techniques which can be collected in general titles as counter-mass balancing, spring balancing, using duplicated mechanisms, active balancing and designing the mechanism as inherently balanced. The evolution of the theory on the balancing of mechanisms as a historical review was presented in (Arekelian et al., 2000). The review includes most theoretical and experimental works in detail up to 2000.

2.2.1. Static Balancing

The ways of obtaining the statically balanced mechanism are to add counterweight, spring and others (can be applicable all potential energy storage elements). Herder (2001) developed methods for statically balanced mechanism with using just linear springs. He pointed out that if static balancing is performed with springs, the system is more lightweight and compact. Moreover, the constructional details developed for the methods are also included in this study.

In the study (Lin et al., 2012), it is aimed to develop a design method for statically balanced planar articulated manipulators which are balanced with spring installation. All acceptable configurations of spring installations can be decided by the design method for any n-link planar articulated manipulator. The design optimization of spring configuration on statically balanced planar articulated manipulators is also discussed in (Lee and Chen, 2014). They considered that using minimum number of springs might not be sufficient for the resulting spring installation and also the choice of a suitable spring constant can be difficult in practice. They compared 2-DOF planar articulated balancing manipulator with and without the minimum number of springs in the end. They suggest additional springs fitted in between consecutive links in order to allow the adjustment of the attachment points of the springs and decrease the spring constants of some specific springs.

Optimum force balancing is addressed with mass distribution and a single elastic element for a five-bar parallel manipulator in (Alıcı and Shirinzadeh, 2003). The purpose of the study is to select suitable mass distribution of links, the size and attachment points

of the elastic element. Only one spring is used among distal links of the manipulator (Figure 2.11) as an elastic element. Also, a non-linear programming method is used in the selection of the mass distributions of the links, spring size and attachment points to ensure that the manipulator is optimum with respect to the bearing and ground forces.

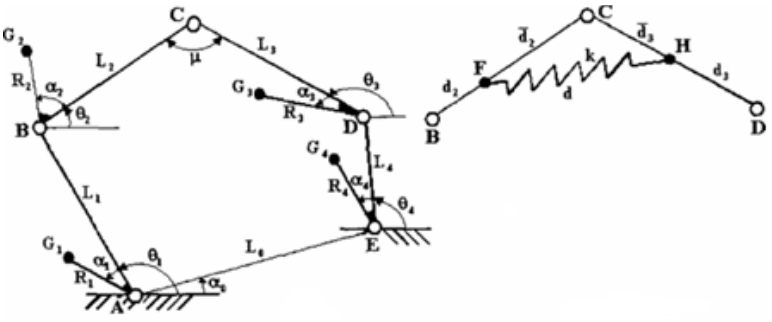

Figure 2.11. (a) Five-bar RRRRR manipulator, (b) Spring among distal links. (Source: Alıcı and Shirinzadeh, 2003).

Another study presents static balancing of a 6-dof parallel manipulator (Russa et al, 2005). This paper presents a method using counterweights with smart design of pantographs. With this method, the global center of mass for any configuration of the manipulators can be made stationary.

Static balancing of a four-bar linkage and its cognates is presented in (Deepak and Ananthasuresh, 2012) (Figure 2.12). Three techniques are applied to statically balance a zero-free-length spring-loaded four-bar linkage. The study is a starting point for the design of statically balanced systems which involves inherent and possibly more complex elastic loads.

2.2.2. Dynamic Balancing

Lowen et al. collected the balancing method of shaking force and shaking moment to obtain the available literature in (1968) and (1983). In (Lowen et al., 1968), the vectors (Berkof and Lowen, 1969), cam methods, duplicate mechanism method, minimum number of counterweights method. The balancing of shaking moment could not be developed in those years. Also, partial balancing methods are presented which are

harmonic or order balancing and addition of springs. In (Lowen et al., 1983), some counter-mass balancing methods are investigated in detail for planar and spatial mechanisms in terms of force and moment balancing of mechanisms such as full force balancing, full force and partial moment balancing etc.

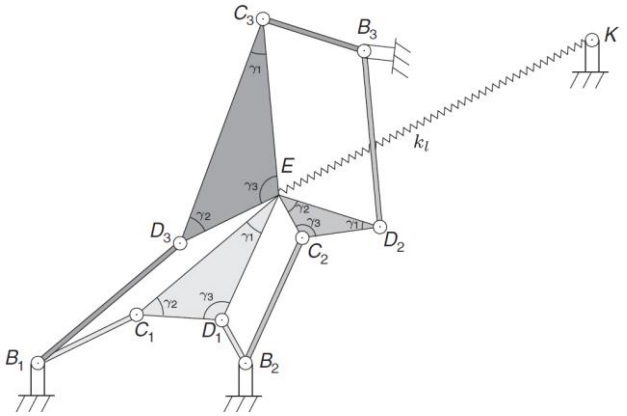

Figure 2.12. The cognates of a four-bar mechanism with a spring.
(Source: Deepak and Ananthasuresh, 2012)

Shaking forces and moments are a significant problem in high-speed machinery. Briot et al. (2012) suggested a solution for the problem of shaking force balancing of high-speed manipulators which is based on the optimal control of the center of masses of the links. This new method is applied for two and three link serial manipulators with different trajectories. Their results show that the reduction of shaking force is 77% for the presented case study. Arakelian and Smith published a review paper with new examples for shaking forces and moments of mechanisms in (Arekelian and Smith, 2005).

Angeles and Lee (Angeles and Lee, 1988) presented an approach for the dynamic balancing of holonomic mechanical systems. Then, a novel formulation of the dynamic balancing of five-bar linkages is presented in (Ilia and Sinatra, 2009) based on (Angeles and Lee, 1988). The dynamic balancing conditions of five-bar linkages are expressed with twelve linkage parameters and the resulting model is used for an optimum design problem. Buganza and Acevedo also presented the dynamic balancing of a five-bar mechanism as an optimization problem (2011). In this study, passive balancing method is used to create a dynamically balanced mechanism. The dynamic equations are obtained by using the Virtual Power Method.

Alici and Shirinzadeh performed a solution of the optimum dynamic balancing where a 2-DOF parallel manipulator is used as an example (2004) (Figure 2.13). An optimization approach is suggested based on the minimization of the sum-squared values of bearing forces, driving torques, shaking moment and the deviation of the angular momentum in order to to reduce any forces, moments transmitted to the base. In (Alıcı and Shirinzadeh, 2006), optimum dynamic balancing of a 2-DOF parallel manipulator is performed based on senitivity analysis. The purpose is completely to eliminate shaking forces and minimize shaking moments by using the optimization approach. Also, this paper includes a procedure which is developed for a high dof (> 2) mechanisms.

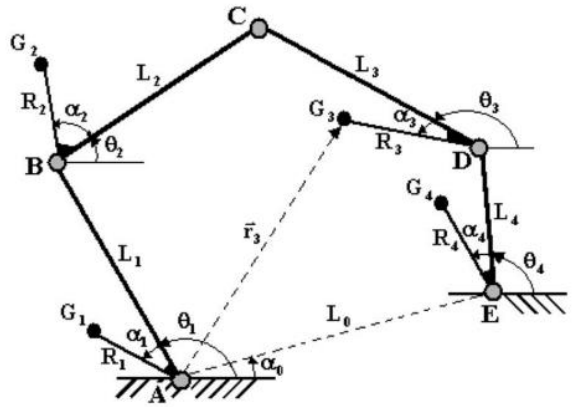

Figure 2.13. Five-bar manipulator with mass center location parameters.
(Source: Alıcı and Shirinzadeh, 2006)

In (Wu et al., 2007), the dynamic characteristics of a planar 2-DOF purely translational parallel manipulator which is part of a hybrid machine are presented (Figure 2.14 (a)). The dynamic model is derived using the Newton-Euler approach. Firstly, the optimal motion of the cutting tool is given to the system and the effect of the counterweights is showed. Based on this effect, the mass of counterweight is decided. The oscillation which results from cutting force is investigated with dynamic simulation. In the milling process, the oscillation of cutting force is an important factor which results in vibration. Finally, the derivation of the inverse dynamics of the parallel manipulator and necessary additional counterweights are presented. In the detailed design, two cover sheets and four brackets are fixed on the machine tool to reduce the vibration (Figure 2.14 (b)).

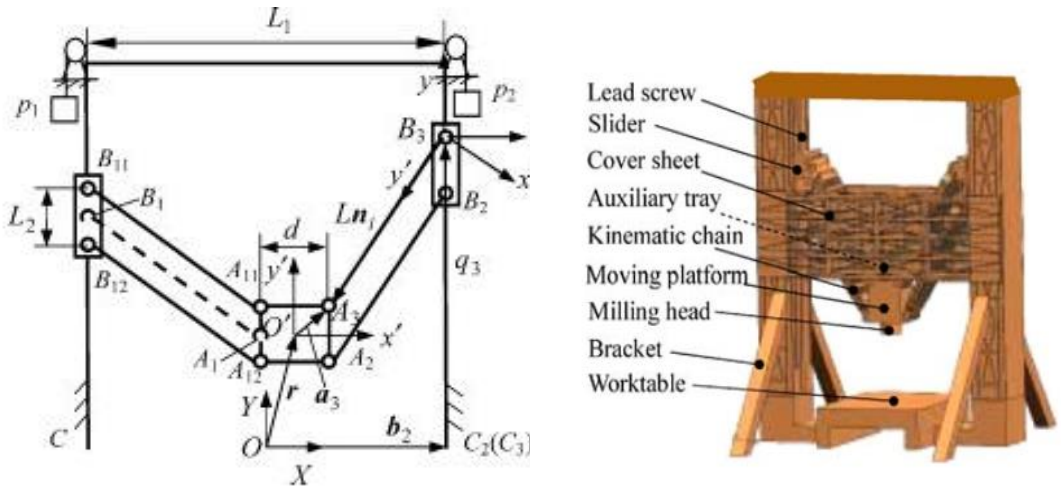

(a) (b)

Figure 2.14. 2-dof planar translational manipulator's (a) kinematic model, (b) prototype. (Source: Wu et al., 2007).

The generic formulations of shaking force and shaking moments are presented for planar mechanisms in (Chaudhary and Saha, 2008). Two mechanisms are taken into consideration which are a four-bar linkage and a multiloop mechanism that is used in carpet scraping machine for cleaning carpets (Figure 2.15). When comparing the analytical results available for the force balancing, the validation of the proposed method is performed.

Wu and Gosselin (2007) presented the dynamic balancing of multi-DOF parallel mechanisms (with multiple legs) by investigating dynamically equivalent set of point masses (two, three or four point masses). That is, the mass and inertia of the moving platform is dynamically replaced by point masses. Locations of point masses are at the point of attachment of the legs to the platform. The design of reactionless 3-DOF 3-RRR parallel manipulators is presented in terms of two approaches (Arekelian and Smith, 2008).

Another method is presented for the complete dynamic balancing of 3-DOF planar parallel manipulators by Gosselin and Ricard (2000). The aim of this article is to perform dynamically balanced 3-DOF planar parallel manipulators without adding unnecessary constraints or additional mechanical elements. Therefore, special legs are used which are formed from dynamically balanced four-bar loops (Figure 2.16).

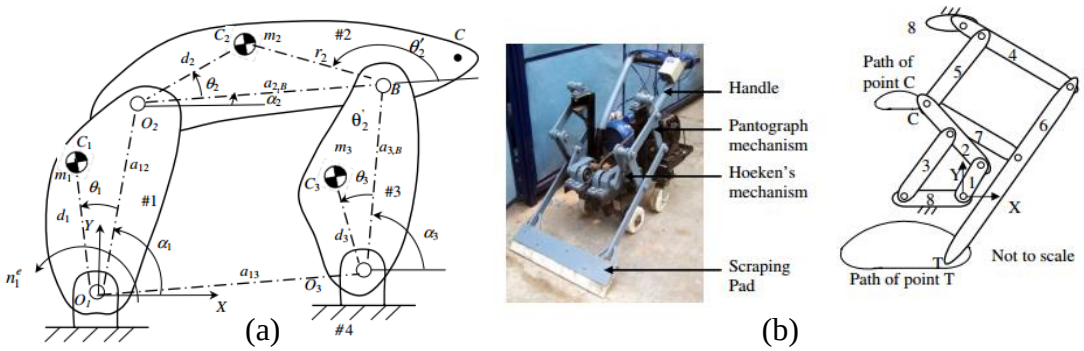

Figure 2.15. (a) A four-bar mechanism, (b) Carpet scraping machine and its multiloop mechanism representation (Source: Chaudhary and Saha, 2008).

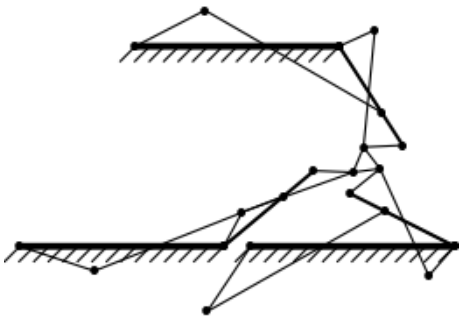

Figure 2.16. Reactionless planar 3-DOF parallel manipulator with four-bar legs. (Source: Gosselin and Ricard, 2000)

Van Der Wijk published several studies about the balancing of mechanisms in the past years (2012; 2009; 2009; 2009; 2009; 2011; 2013). Although dynamic balancing provides many advantages, it has a disadvantage about increasing mass of mechanisms. Two of the the studies (2012; 2009) are to compare principles of dynamic balancing according to additional mass and inertia. These principles are duplicate mechanisms, separate counter-rotation and counter-rotary counter-masses. The principle of duplicate mechanism means that the mechanism is dynamically balanced with addition of its axial and mirror symmetric mechanisms. The separate counter-rotation principle is to add two different masses. One of them is rotatable for the moment balance. The counter-rotary counter-mass principle balances the mechanism with a mass which is rotatable at the same time. Examinations of the principles in the papers (2012) and (2009) are realized on the pendulum and the double pendulum, respectively. As a result of these papers, the principle of duplicate mechanisms is the best choice or the low mass and inertia. But it is necessary to consider in terms of foot-print of the mechanism as well. When the total

mass relation is considered, the counter-rotary counter-mass principle is more convenient than the separate counter-rotation.

The principles are investigated to obtain low mass and inertia values for different mechanisms such as a five-bar planar mechanism (RRRRR), slider-crank and etc. (Wijk, 2009). Moreover, (Wijk and Herder, 2009) shows synthesis of dynamically balanced mechanisms by using counter-rotary counter-mass. A balanced double pendulum is used to create other mechanisms like 2-DOF and 3-DOF planar mechanisms.

Another study investigates some effects and makes suggestions for the design of dynamically balanced mechanisms in consideration of low mass and inertia in (Wijk and Herder, 2009). The investigated effects are the balancing structure, parameters, design space and workspace of the mechanism.

A generic method is proposed to evaluate the general shaking force balance conditions of parallel manipulators which are considered as whole mechanism instead of link by link (Wijk et al., 2011). The linear momentum equations are derived as a first step for this method. Then, these equations are put in the velocity loop closure equations to basically obtain the general shaking force conditions. In this paper, the method is applied on a 4-RRR parallel manipulator which is a redundant planar 3-DOF manipulator (Figure 2.17).

The design and experimental evaluation of dynamically balanced redundant planar 4-RRR parallel manipulator is presented in (Wijk et al., 2013). After the derivation of direct and inverse kinematics and dynamics model of the manipulator, prototypes of balanced and unbalanced mechanism are examined to compare in terms of shaking force at 3g and 10.3g (g: gravitational acceleration). The results of experimental tests show 97% lower shaking force and 96% lower shaking moment.

Foucault and Gosselin (2004) presented synthesis, design and prototyping of a planar 3-dof reactionless parallel mechanism. Reactionless mechanism means dynamically balanced mechanism. The parallel mechanism is designed by using 5-bar linkage as a leg (Figure 2.18). The trajectory of the platform is observed and its displacement is measured to see the influence of shaking force.

There is a patent (Menschaar et al., 2006) for the dynamic balancing of a planar five-bar parallel manipulator. If all links of five-bar mechanism have same length and the two fixed revolute joints are coincident with each other, the force balancing becomes

simple and the passive moment balancing is possible. A schematic representation is shown in Figure 2.19.

Another patent is filed for delta robot by Herder and Wijk in (2012). The pantographs which can be seen in Figure 2.20 are attached to the base in parallel to the proximal link. They are used to support counter-masses. Thanks to pantographs and counter-masses, the delta robot is dynamically balanced.

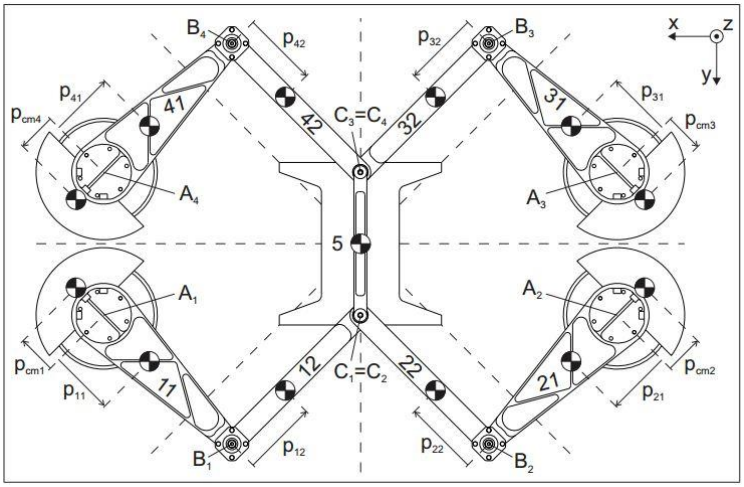

Figure 2.17. Redundant planar 4-RRR parallel manipulator.
(Source: Wijk et al., 2013)

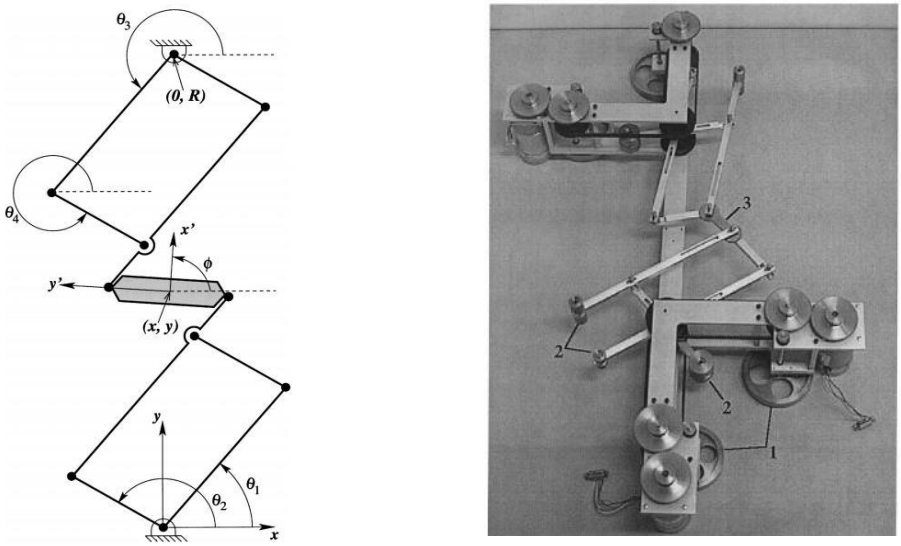

(a) (b)

Figure 2.18. (a) Kinematic structure, (b) prototype of the mechanism.
(Source: Foucault and Gosselin, 2004)

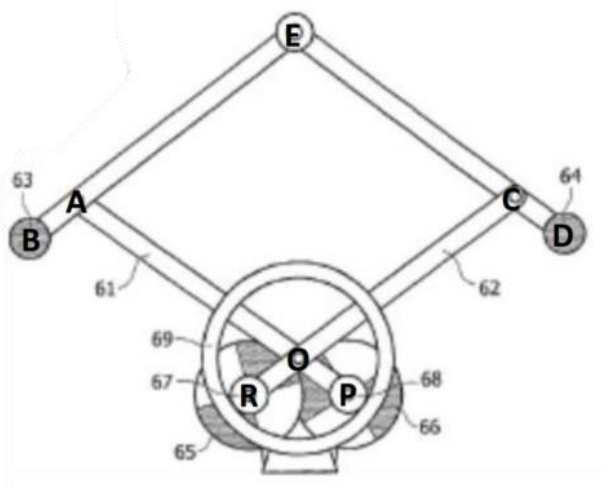

Figure 2.19. A dynamically balanced planar five-bar parallel manipulator.
(Source: Menschaar et al., 2006)

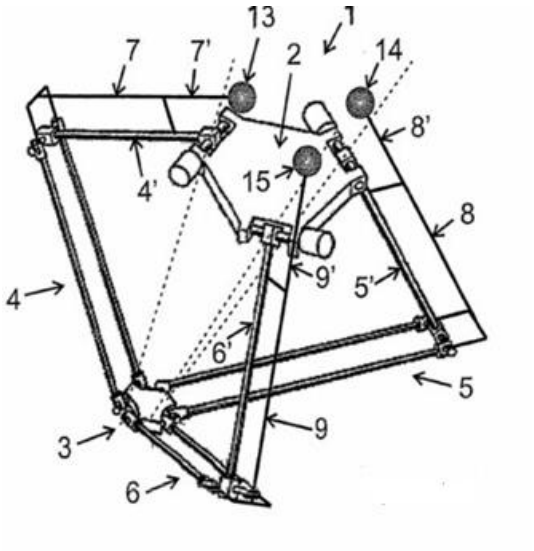

Figure 2.20. Balanced Delta Robot.
(Source: Herder and Wijk, 2012)

CHAPTER 3

DETERMINATION OF THE KINEMATIC STRUCTURE AND DYNAMIC FORCE ANALYSIS OF THE MECHANISM

In this Chapter, the 2- dof mechanism alternatives are evaluated according to their advantages. Then, the kinematic model of the selected mechanism is constructed. Force balancing equations are constructed to obtain force balancing masses. Lastly, dynamic model is generated using two different method. The formulations were obtained based on the studies in SanTez project no: 01668.STZ.2012-2.

3.1. Conceptual Design of the Mechanism

In this section, alternatives of mechanisms are investigated for some selected simply and over-constrained 2-dof mechanisms. Each mechanism should perform planar motion to locate the end-effector. Therefore, after planar 2-dof mechanisms are examined in general, simply and over-constrained mechanism alternatives are presented.

3.1.1. 2-dof Planar Mechanism Alternatives

If a planar mechanism has only revolute and prismatic joints, has 2-dof and and comprises a single loop, it consists of 5 links and 5 joints. Preferably it should not have more than two prismatic (P) joints. In this way, thirty-two possible alternatives of the mechanisms are obtained for combinations which have 0P, 1P and 2P. The number of alternatives can be firstly reduced to twenty by eliminating mirror linkages (e.g.: RRRPP and PPRRR) (McCloy, 1990). Six mechanism alternatives (Figure 3.1) remain after consideration of some conditions:

- Actuators have to be mounted on the base.

- An actuated joint should not carry the weight of other actuated joint. (e.g.: RPRRR first revolute joint carries the weight of prismatic joint and it is not convenient)
- If prismatic joints are used, they must be actuated because passive prismatic joints have friction and accuracy problems.

With the conditions, the remaining six alternatives are presented in Figure 3.1.

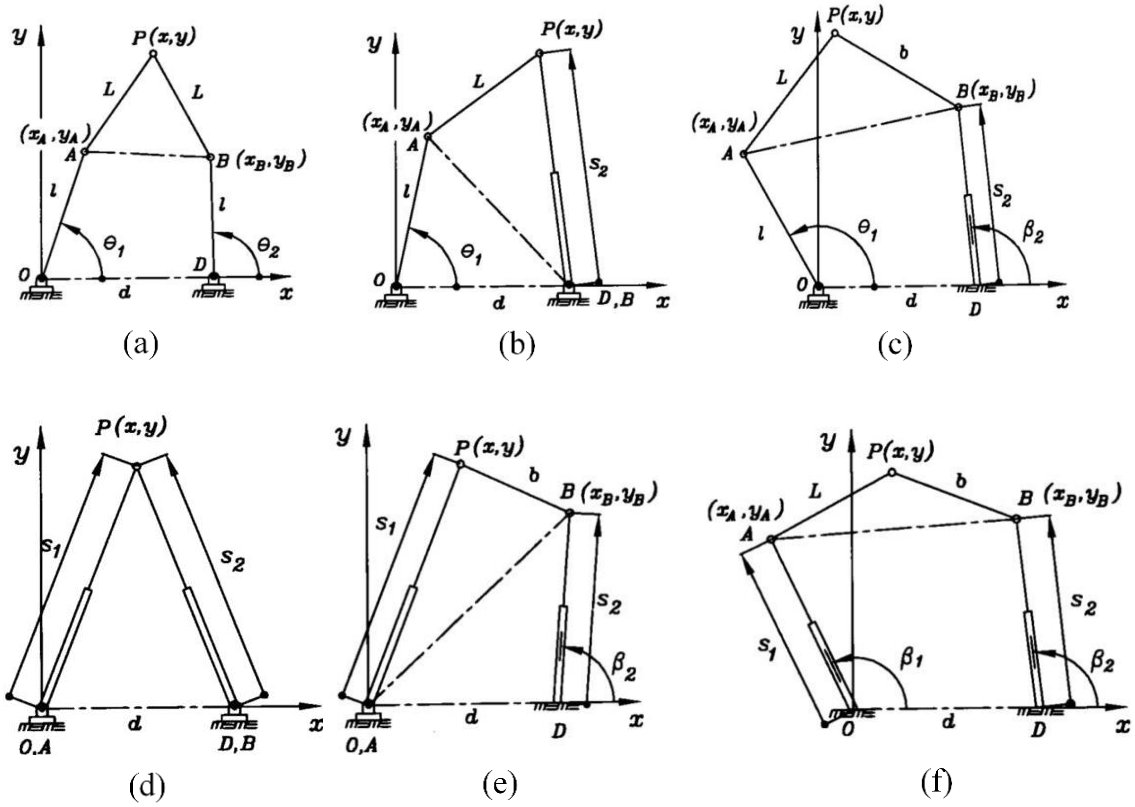

Figure 3.1. Kinematic structures of the six mechanism alternatives: (a) RRRRR, (b) RRRPR, (c) RRRRP, (d) RPRRP, (e) RPRPR, (f) PRRRP (Source: Cervantes-Sanchez and Rendon Sanchez, 1999).

Cervantes-Sanchez and Rendon-Sanchez (1999) showed a way to find workspace for all six alternatives, while Alıcı (2000) presented a method based on Jacobian matrices to determine singular configurations.

Some alternatives should be eliminated for which a prismatic joint is carried by a revolute joint. Actuators are linear actuators which are located on a moving arm for this structure. In this situation, high inertia is observed which is not suitable for high speed parallel mechanisms. Moreover, when consideration of workspace symmetry, basic kinematic equation and ease of balancing, the remaining alternatives are RRRRR and

PRRRP. There are many studies on the investigation of the two mechanism in the literature. PRRRP is more rigid and can reach to high speed values. Schütz et al. (2010) compared the two mechanisms in terms of compactness and singularity analysis based on forward and inverse kinematic Jocabian matrices in the same workspace area. It is showed that a smaller size of RRRRR can work in the same workspace. Therefore, RRRRR mechanism can have a relatively light weight. Furthermore, it shows better accuracy, stiffness and force transmission behaviour and less motor torque requirement. Thus, it is suitable for high speed applications. On the other hand, PRRRP mechanism has better potential of high speed and high velocity transmission (the ratio between speed of end effector and speed of actuator). It can be said that it is a convenient mechanism for pick-and-place applications.

RRRRR (5R) kinematic structure is selected in this thesis in order to be able to keep the platform orientation constant and ease of balancing. In the next subsection, alternatives of simply and over-constrained mechanisms based on the 5R mechanism are presented.

3.1.1.1. Simply Constrained Mechanism Alternatives

1) General 5R Mechanism

The mechanism which can be seen in Figure 3.2 (a) is actuated from A_0 and B_0 fixed revolute joints. Input variables are θ_1 and θ_2 angles and θ_3 and θ_4 are passive joint variables. "E" point represents the end-effector. Link length of $|A_0A|$ and $|AE|$ are respectively equal to $|B_0B|$ and $|BE|$ for a symmetric workspace. If the mechanism is evaluated in terms of constructional design, there is no problem about fixed revolute joint connections and the base link design. However, it is difficult to assemble the end-effector to the point "E". In this situation, the end-effector orientation is not controlled and it requires some auxiliary mechanisms such as a timing belt-pulley system to fix the end-effector orientation.

2) 5R Mechanism with Coincident Fixed Axes

Fixed revolute joints are coincident at point "O" (Figure 3.2 (b)). The lengths of link 1, 2, 3 and 4 can be selected as equal each other due to easier balancing (Menschaar et al.,2006). Although this special case has simpler kinematic structure than the general

case, the detail of motor connections is relatively complicated due to coincident fixed revolute joints. The axes of the motors can be different from the revolute joint axes by using a geared connection between the motor and joint axes.

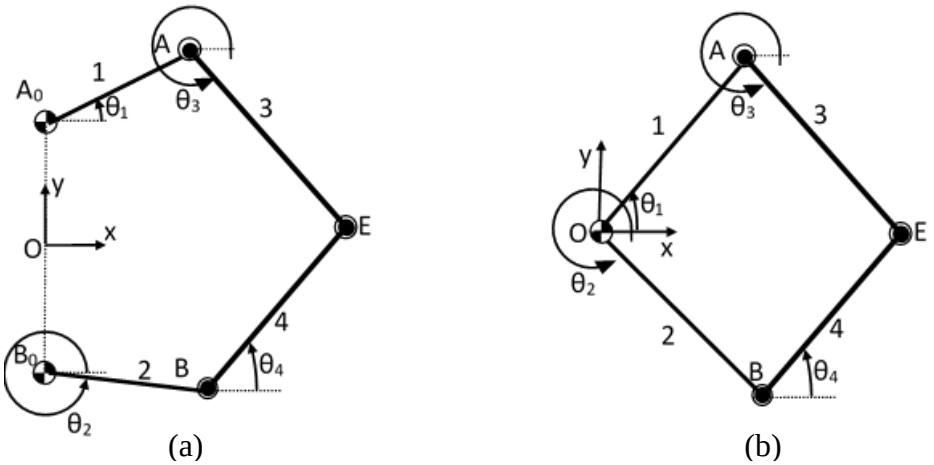

Figure 3.2. (a) General 5R mechanism, (b) 5R mechanism with coincident fixed axes.

3) 6R mechanisms with additional parallelogram loops

The construction of base and end-effector is simpler than 5R mechanisms for 6R mechanisms. Because, unlike 5R mechanisms, there is no coincident axis. However, in order to reduce the increased dof, parallelogram loops are placed in at least one side arm so that the end-effector orientation is fixed. The other option is to use timing belt-pulley system instead of parallelogram loops. But there tensioning the belts is a problem. If the belt is over-tensioned, excessive joint forces are observed. If the belt is less tensioned, there will be vibrations and backlash due to flexibility.

Placing the parallelogram loops in one arm (Figure 3.3 (a)) is sufficient for kinematic constraints. For symmetric mass distribution, parallelogram loops can be placed in both arms, but the mechanism will be an overcontrained mechanism. To prevent the over-constrained mechanism structure, one of the R joints can be replaced with a pin-in-slot joint ("L" joint in Figure 3.3 (b)). Also, link 11 can be removed to prevent over-constraint. Both mechanisms in Figure 3.3 are kinematically equivalent to the 5R mechanism with coincident fixed joint axes shown in Figure 3.2 (b). The disadvantage of the 6R mechanism alternatives is to use more number of links/joints and increased inertia values.

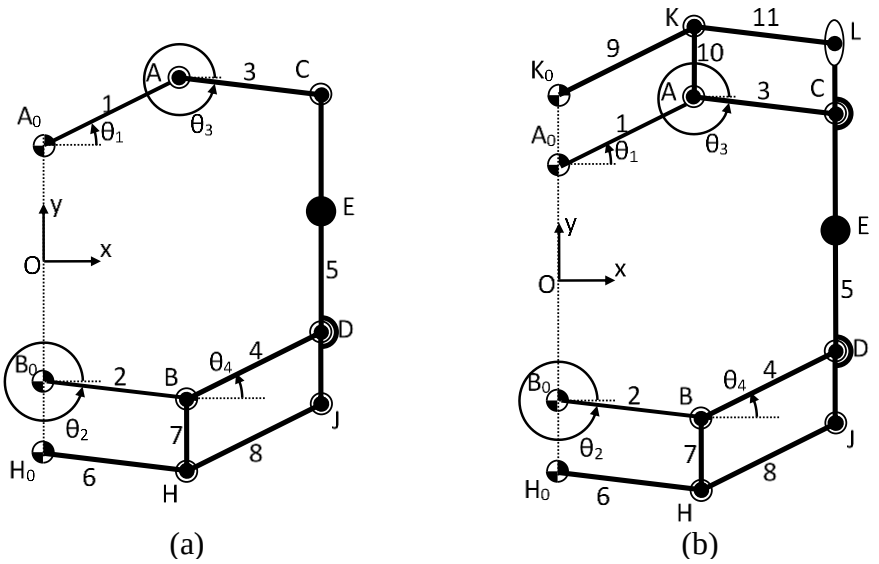

(a) (b)

Figure 3.3. (a) Simply constrained 6R mechanism with two parallelogram loops, (b) simply constrained 6R mechanism with a pin-in-slot joint.

3.1.1.2. Over-constrained Mechanism Alternatives

The only over-constrained mechanism alternative is an over-constrained 6R mechanism (Figure 3.4) $|A_0B_0|$ must be equal to |CD|. The dimensions of links 1, 2, 3, 4 are equal. When the link lengths of the links in parallel are not identical (due to manufacturing errors, joint backlash, etc.) there is no analytical inverse kinematic solution due to over-constrained. Also, the force analysis cannot be performed solely based on equilibrium equations of rigid bodies. Hidden robot analogy can be used for the control and calibration (Dede et al., 2016). So, the kinematic equivalent of the over-constrained 6R mechanism is 5R mechanism in Figure 3.2 (b).

The following criteria are taken into account to select a simply constrained mechanism:

1) Ease of balancing and mathematical model
2) To have similar construction of the over-constrained mechanism to compare the results
3) Structural simplicity
4) To keep the orientation of the end-effector constant
5) Structural symmetry
6) Kinematic equivalence

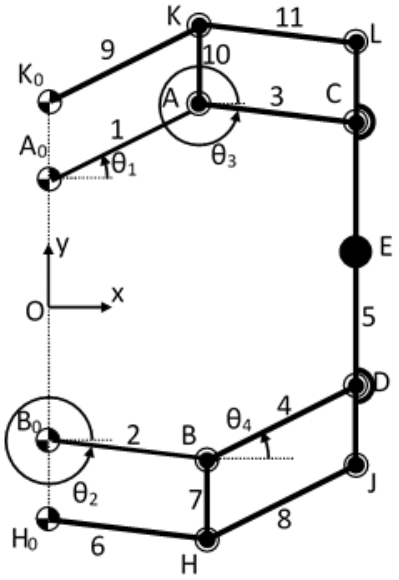

Figure 3.4. Over-constrained 6R mechanism.

The general 5R mechanism (Figure 3.2 (a)) has disadvantage about criterion (1). The coincident fixed axes 5R mechanism (Figure 3.2 (b)) is advantageous in terms of criteria (1), (5), (6), but it possesses constructional complexity about assembly of motors and the end-effector in terms of criteria (3) and (4). Although the 6R mechanism with 2 or 3 parallelogram loops (Figure 3.3 (a)) is disadvantageous in terms of criterion (5), it is possible to provide the balancing of mass. Moreover, it has more advantage than other alternatives about criterion (2). Therefore, it is enough to design a mechanism for over-constrained and simply constrained mechanisms and the 6R mechanism with 3 parallelogram loops is selected as a simply constrained mechanism. To obtain the simply constrained mechanism, one link of a parallelogram loop is removed.

3.2. Kinematic Model

In this section, forward and inverse kinematic models are derived for the selected over-constrained 6R mechanism. It is assumed that the assembly mode of the mechanism does not change for both forward and inverse kinematics. A parametric study of these models is created by integrating to Microsoft Excel environment.

Two mechanism kinematic structures are given in Figure 3.5 to explain how to solve the kinematic model of the over-constrained mechanism. There are no kinematic

analytical solutions of over-constrained mechanisms. Therefore, hidden robot analogy is used to solve it. The 5R mechanism with coincident fixed joint axes (Figure 3.5 (a)) is used to derive the kinematic model of over-constrained 6R mechanism due to kinematic equivalence. The outputs from the kinematic model are then used for the force balancing model and the dynamic model. The link lengths numbered 1, 2, 3 and 4 are identical as in the over-constrained mechanism.

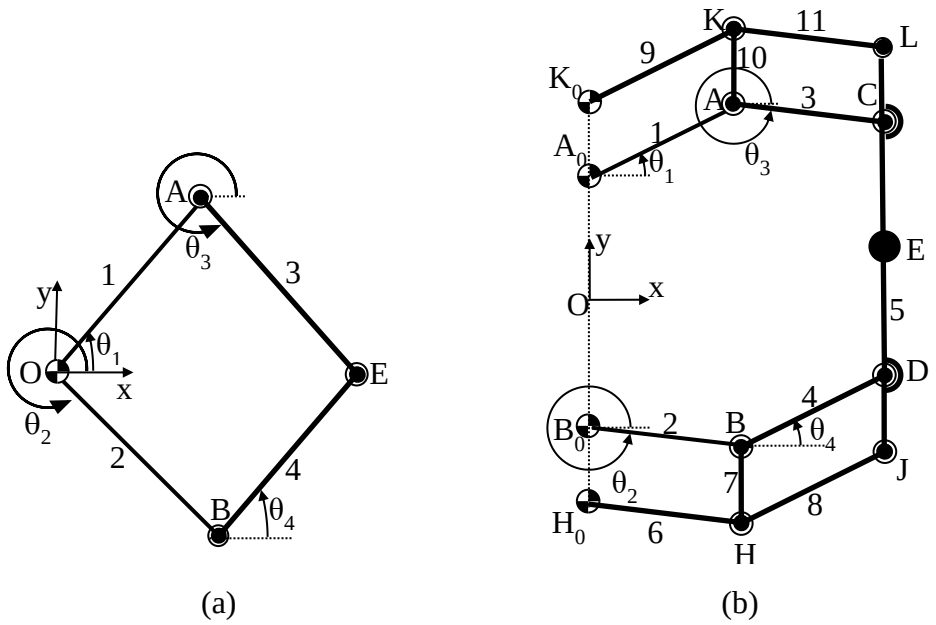

Figure 3.5. Kinematic structure of: (a) The coincident Fixed Axes 5R, (b)The over-constrained 6R mechanism.

3.2.1. Forward Kinematics

For this model, θ_1, θ_2, ω_1, ω_2 and α_1, α_2 are the inputs to find E(x,y), V_{Ex}, V_{Ey}, a_{Ex}, a_{Ey}. Firstly, θ_3 and θ_4 are calculated from the group of Equation 3.1 (mag and ang functions respectively give the magnitude and angle of a vector with given horizontal and vertical components):

$$|OA| = |OB| = |AE| = |BE| = r$$

$$\overrightarrow{OA} = re^{i\theta_1},\ \overrightarrow{OB} = re^{i\theta_2}$$

$$\vec{s} = \overrightarrow{AB} = r(e^{i\theta_2} - e^{i\theta_1})$$

$$
\begin{aligned}
s = \left|\vec{s}\right| &= \mathrm{mag}\left[r(\cos\theta_2 - \cos\theta_1), r(\sin\theta_2 - \sin\theta_1)\right]\phi \\
\measuredangle\vec{s} &= \mathrm{ang}\left[r(\cos\theta_2 - \cos\theta_1), r(\sin\theta_2 - \sin\theta_1)\right] \\
\eta &= \mathrm{ang}\cos(r, s, r) \\
\theta_3 &= \phi + \eta,\ \overrightarrow{OE} = \overrightarrow{OA} + re^{i\theta_3} \\
\theta_4 &= \measuredangle\overrightarrow{BE} = \mathrm{ang}[(\overrightarrow{OE} - \overrightarrow{OB})_x, (\overrightarrow{OE} - \overrightarrow{OB})_y].
\end{aligned}
\tag{3.1}
$$

Loop Closure Equation:

$$
\overrightarrow{OA} + \overrightarrow{AE} = \overrightarrow{OB} + \overrightarrow{BE} \Rightarrow r(e^{i\theta_1} + e^{i\theta_3}) = r(e^{i\theta_2} + e^{i\theta_4}) \tag{3.2}
$$

Velocity Loop Equation:

$$
e^{i\theta_3}\omega_3 - e^{i\theta_4}\omega_4 = e^{i\theta_2}\omega_2 - e^{i\theta_1}\omega_1 \tag{3.3}
$$

Complex conjugate of Equation 3.3:

$$
e^{-i\theta_3}\omega_3 - e^{-i\theta_4}\omega_4 = e^{-i\theta_2}\omega_2 - e^{-i\theta_1}\omega_1 \tag{3.4}
$$

Using Caramer's Rule, angular velocities are found in Equation 3.5:

$$
\begin{aligned}
\omega_3 &= \frac{\begin{vmatrix} e^{i\theta_2}\omega_2 - e^{i\theta_1}\omega_1 & -e^{i\theta_4} \\ e^{-i\theta_2}\omega_2 - e^{-i\theta_1}\omega_1 & -e^{-i\theta_4} \end{vmatrix}}{\begin{vmatrix} e^{i\theta_3} & -e^{i\theta_4} \\ e^{-i\theta_3} & -e^{-i\theta_4} \end{vmatrix}} = \frac{-\sin(\theta_1 - \theta_4)\omega_1 + \sin(\theta_2 - \theta_4)\omega_2}{\sin(\theta_3 - \theta_4)} \\
\omega_4 &= \frac{\begin{vmatrix} e^{i\theta_3} & e^{i\theta_2}\omega_2 - e^{i\theta_1}\omega_1 \\ e^{-i\theta_3} & e^{-i\theta_2}\omega_2 - e^{-i\theta_1}\omega_1 \end{vmatrix}}{\begin{vmatrix} e^{i\theta_3} & -e^{i\theta_4} \\ e^{-i\theta_3} & -e^{-i\theta_4} \end{vmatrix}} = \frac{-\sin(\theta_1 - \theta_3)\omega_1 + \sin(\theta_2 - \theta_3)\omega_2}{\sin(\theta_3 - \theta_4)}
\end{aligned}
\tag{3.5}
$$

Kinematic Singularities: $\theta_3 = \theta_4$ or $\theta_3 = \theta_4 + \pi$.

The velocity of end-effector can be written with known θ_3, θ_4, ω_3, ω_4 in Equation 3.6;

$$
\begin{aligned}
V_{Ex} + V_{Ey} &= ir(e^{i\theta_1}\omega_1 + e^{i\theta_3}\omega_3) \\
&= -r(\sin\theta_1\omega_1 + \sin\theta_3\omega_3) + ir(\cos\theta_1\omega_1 + \cos\theta_3\omega_3)
\end{aligned}
\tag{3.6}
$$

Acceleration Loop Equation:

$$e^{i\theta_3}\alpha_3 - e^{i\theta_4}\alpha_4 = e^{i\theta_2}(\alpha_2 + i\omega_2^{\,2}) - e^{i\theta_1}(\alpha_1 + i\omega_1^{\,2}) - i(e^{i\theta_3}\omega_3^{\,2} - e^{i\theta_4}\omega_4^{\,2}) \quad (3.7)$$

Complex Conjugate of Equation 3.7:

$$e^{-i\theta_3}\alpha_3 - e^{-i\theta_4}\alpha_4 = e^{-i\theta_2}(\alpha_2 - i\omega_2^{\,2}) - e^{-i\theta_1}(\alpha_1 - i\omega_1^{\,2}) + i(e^{-i\theta_3}\omega_3^{\,2} - e^{-i\theta_4}\omega_4^{\,2}) \quad (3.8)$$

For the rest of the formulations for conciseness c and s stand for cosine and sine, respectively. Using Cramer's Rule, α_3 and α_4 are calculated in Equation 3.9 and 3.10:

$$\alpha_3 = \frac{\begin{vmatrix} e^{i\theta_2}(\alpha_2 + i\omega_2^{\,2}) - e^{i\theta_1}(\alpha_1 + i\omega_1^{\,2}) - i(e^{i\theta_3}\omega_3^{\,2} - e^{i\theta_4}\omega_4^{\,2}) & -e^{i\theta_4} \\ e^{-i\theta_2}(\alpha_2 - i\omega_2^{\,2}) - e^{-i\theta_1}(\alpha_1 - i\omega_1^{\,2}) + i(e^{-i\theta_3}\omega_3^{\,2} - e^{-i\theta_4}\omega_4^{\,2}) & -e^{-i\theta_4} \end{vmatrix}}{\begin{vmatrix} e^{i\theta_3} & -e^{i\theta_4} \\ e^{-i\theta_3} & -e^{-i\theta_4} \end{vmatrix}} \quad (3.9)$$

$$\alpha_3 = \frac{-s(\theta_1 - \theta_4)\alpha_1 + s(\theta_2 - \theta_4)\alpha_2 - c(\theta_1 - \theta_4)\omega_1^{\,2} + c(\theta_2 - \theta_4)\omega_2^{\,2} - c(\theta_3 - \theta_4)\omega_3^{\,2} + \omega_4^{\,2}}{s(\theta_3 - \theta_4)}$$

$$\alpha_4 = \frac{\begin{vmatrix} e^{i\theta_3} & e^{i\theta_2}(\alpha_2 + i\omega_2^{\,2}) - e^{i\theta_1}(\alpha_1 + i\omega_1^{\,2}) - i(e^{i\theta_3}\omega_3^{\,2} - e^{i\theta_4}\omega_4^{\,2}) \\ e^{-i\theta_3} & e^{-i\theta_2}(\alpha_2 - i\omega_2^{\,2}) - e^{-i\theta_1}(\alpha_1 - i\omega_1^{\,2}) + i(e^{-i\theta_3}\omega_3^{\,2} - e^{-i\theta_4}\omega_4^{\,2}) \end{vmatrix}}{\begin{vmatrix} e^{i\theta_3} & -e^{i\theta_4} \\ e^{-i\theta_3} & -e^{-i\theta_4} \end{vmatrix}} \quad (3.10)$$

$$\alpha_4 = \frac{-s(\theta_1 - \theta_3)\alpha_1 + s(\theta_2 - \theta_3)\alpha_2 - c(\theta_1 - \theta_3)\omega_1^{\,2} + c(\theta_2 - \theta_3)\omega_2^{\,2} - \omega_3^{\,2} + c(\theta_3 - \theta_4)\omega_4^{\,2}}{s(\theta_3 - \theta_4)}$$

The acceleration of end-effector can be written with known θ_3, θ_4, ω_3, ω_4, α_3, α_4 in Equation 3.11;

$$\begin{aligned} a_{Ex} + ia_{Ey} &= r[i(e^{i\theta_1}\alpha_1 + e^{i\theta_3}\alpha_3) - (e^{i\theta_1}\omega_1^{\,2} + e^{i\theta_3} + \omega_3^{\,2})] \\ &= r[-(s\theta_1\alpha_1 + s\theta_3\alpha_3 + c\theta_1\omega_1^{\,2} + c\theta_3\omega_3^{\,2}) \\ &\quad + i(c\theta_1\alpha_1 + c\theta_3\alpha_3 - s\theta_1\omega_1^{\,2} + s\theta_3\omega_3^{\,2})] \end{aligned} \quad (3.11)$$

3.2.2. Inverse Kinematics

When E(x,y), V_{Ex}, V_{Ey}, a_{Ex}, a_{Ey}, are given, θ_1, θ_2, ω_1, ω_2, α_1, α_2 are found. θ_1 and θ_2 are calculated from the group of Equation 3.12:

$$\overrightarrow{s_{1,2}} = \overrightarrow{OE} = x + iy,\ s_{1,2} = \left|\overrightarrow{s_{1,2}}\right| = \text{mag}(x, y), \phi_{1,2} = \measuredangle\overrightarrow{s_{1,2}} = \text{ang}(x, y)$$
$$\eta_{1,2} = \measuredangle\text{EOA or}\measuredangle\text{EOB} = \text{ang}(r, s_{1,2}, r) \tag{3.12}$$
$$\theta_1 = \phi_{1,2} + \eta_{1,2},\ \theta_3 = \text{ang}(x - r\cos\theta_1, y - r\sin\theta_1)$$
$$\theta_2 = \phi_{1,2} - \eta_{1,2}, \theta_4 = \text{ang}(x - r\cos\theta_2, y - r\sin\theta_2)$$

The angular speeds ω_1 and ω_3 are calculated with using Cramer's rule from Equations 3.13-14.

$$\begin{aligned} ir(e^{i\theta_1}\omega_1 + e^{i\theta_3}\omega_3) &= V_{Ex} + iV_{Ey} \\ -ir(e^{-i\theta_1}\omega_1 + e^{-i\theta_3}\omega_3) &= V_{Ex} - iV_{Ey} \end{aligned} \tag{3.13}$$

$$\begin{aligned} \omega_1 &= \frac{\begin{vmatrix} V_{Ex} + iV_{Ey} & ire^{i\theta_3} \\ V_{Ex} - iV_{Ey} & -ire^{i\theta_3} \end{vmatrix}}{\begin{vmatrix} ire^{i\theta_1} & ire^{i\theta_3} \\ -ire^{-i\theta_1} & -ire^{-i\theta_3} \end{vmatrix}} = -\frac{c\theta_3 V_{Ex} + s\theta_3 V_{Ey}}{rs(\theta_1 - \theta_3)} \\ \omega_3 &= \frac{\begin{vmatrix} ire^{i\theta_1} & V_{Ex} + iV_{Ey} \\ -ire^{-i\theta_1} & V_{Ex} - iV_{Ey} \end{vmatrix}}{\begin{vmatrix} ire^{i\theta_1} & ire^{i\theta_3} \\ -ire^{-i\theta_1} & -ire^{-i\theta_3} \end{vmatrix}} = \frac{c\theta_1 V_{Ex} + s\theta_1 V_{Ey}}{rs(\theta_1 - \theta_3)} \end{aligned} \tag{3.14}$$

The same solution is also used for ω_2, ω_4:

$$\begin{aligned} ia(e^{i\theta_2}\omega_2 + e^{i\theta_4}\omega_4) &= V_{Ex} + iV_{Ey} \\ \omega_2 = -\frac{c\theta_4 V_{Ex} + s\theta_4 V_{Ey}}{rs(\theta_2 - \theta_4)}, \omega_4 &= \frac{c\theta_2 V_{Ex} + s\theta_2 V_{Ey}}{rs(\theta_2 - \theta_4)} \end{aligned} \tag{3.15}$$

The angular accelerations α_1 and α_3 are calculated with Equation 3.16, the acceleration equation of end-effector and its complex conjugate; Equation 3.17, Cramer Rule's for α_1; Equation 3.18, Cramer Rule's for α_3:

$$\begin{aligned} ir(e^{i\theta_1}\alpha_1 + e^{i\theta_3}\alpha_3) &= a_{Ex} + ia_{Ey} + r(e^{i\theta_1}\omega_1^2 + e^{i\theta_3}\omega_3^2) \\ -ir(e^{-i\theta_1}\alpha_1 + e^{-i\theta_3}\alpha_3) &= a_{Ex} - ia_{Ey} + r(e^{-i\theta_1}\omega_1^2 + e^{-i\theta_3}\omega_3^2) \end{aligned} \tag{3.16}$$

$$\alpha_1 = \frac{\begin{vmatrix} a_{Ex} + ia_{Ey} + r(e^{i\theta_1}\omega_1^2 + e^{i\theta_3}\omega_3^2) & ire^{i\theta_3} \\ a_{Ex} - ia_{Ey} + r(e^{-i\theta_1}\omega_1^2 + e^{-i\theta_3}\omega_3^2) & -ire^{-i\theta_3} \end{vmatrix}}{\begin{vmatrix} ire^{i\theta_1} & ire^{i\theta_3} \\ -ire^{-i\theta_1} & -ire^{-i\theta_3} \end{vmatrix}}$$

$$= -\frac{c\theta_3 a_{Ex} + s\theta_3 a_{Ey} + r[c(\theta_1 - \theta_3)\omega_1^2 + \omega_3^2]}{rs(\theta_1 - \theta_3)} \tag{3.17}$$

$$\alpha_3 = \frac{\begin{vmatrix} ire^{i\theta_1} & a_{Ex} + ia_{Ey} + r(e^{i\theta_1}\omega_1^2 + e^{i\theta_3}\omega_3^2) \\ -ire^{-i\theta_1} & a_{Ex} - ia_{Ey} + r(e^{-i\theta_1}\omega_1^2 + e^{-i\theta_3}\omega_3^2) \end{vmatrix}}{\begin{vmatrix} ire^{i\theta_1} & ire^{i\theta_3} \\ -ire^{-i\theta_1} & -ire^{-i\theta_3} \end{vmatrix}}$$

$$= \frac{c\theta_1 a_{Ex} + s\theta_1 a_{Ey} + r[\omega_1^2 + c(\theta_1 - \theta_3)\omega_3^2]}{rs(\theta_1 - \theta_3)} \tag{3.18}$$

The same solution is also used for α_2, α_4:

$$ir(e^{i\theta_2}\alpha_2 + e^{i\theta_4}\alpha_4) = a_{Ex} + ia_{Ey} + r(e^{i\theta_2}\omega_2^2 + e^{i\theta_4}\omega_4^2)$$

$$\alpha_2 = -\frac{c\theta_4 a_{Ex} + s\theta_4 a_{Ey} + r[c(\theta_2 - \theta_4)\omega_2^2 + \omega_4^2]}{rs(\theta_2 - \theta_4)} \tag{3.19}$$

$$\alpha_4 = \frac{c\theta_2 a_{Ex} + s\theta_2 a_{Ey} + r[\omega_2^2 + c(\theta_2 - \theta_4)\omega_4^2]}{rs(\theta_2 - \theta_4)}$$

3.3. Force Balancing Equations

The mechanism can be balanced in order to reduce the effect of vibrations caused by the shaking forces acting on the base due to inertial forces. In order to simplify the force balancing model of the over-constrained mechanism, a lumped mass model is formed to deal with parallel links and include shafts, bearings, bolts, nuts etc. The link numbers can be followed from Figure 3.5 (b). Firstly, link-9 (or link-6) is lumped on link-1 (or link-2) (Figure 3.6 (a)). Mass of link-1 and link-9 can be safely added and considered as lumped mass m_{11} (or m_{21}), because they remain parallel to each other, so they have the same velocity direction and hence the associated linear momentum expressions are additive. The total mass m_{11} and common center of mass of all associated links are

measured in Solidworks (Figure 3.6 (a)) and the distance of the center of mass to its rotation center, p_1, is evaluated. Then, link-11 and link-10 (or link-8 and link-7) are lumped on link-3 (or link-4) as m_{12} (or m_{22}) (Figure 3.6 (b)) with the similar considerations. Thus, two set of lumped masses, m_{11} and m_{12} (or m_{21} and m_{22}), are obtained for two parallelogram loops per each side of the over-constrained mechanism. Everything connected to the platform are shown as m_5 which is at the geometric center of the platform. Thus, m_{11}, m_{12}, m_{21}, m_{22} and m_5 are obtained to calculate the balancing masses (m_{bmi}). The mechanism is simplified in this way and the equivalent model for force balancing is shown in Figure 3.7. Due to symmetrical construction of the manipulator, $m_{11} = m_{21} = m_1$ and $m_{12} = m_{22} = m_2$. P_{ij} represent the lumped mass centers of links, whereas P_{bmi} represent the mass centers of balancing masses for i, j = 1, 2.

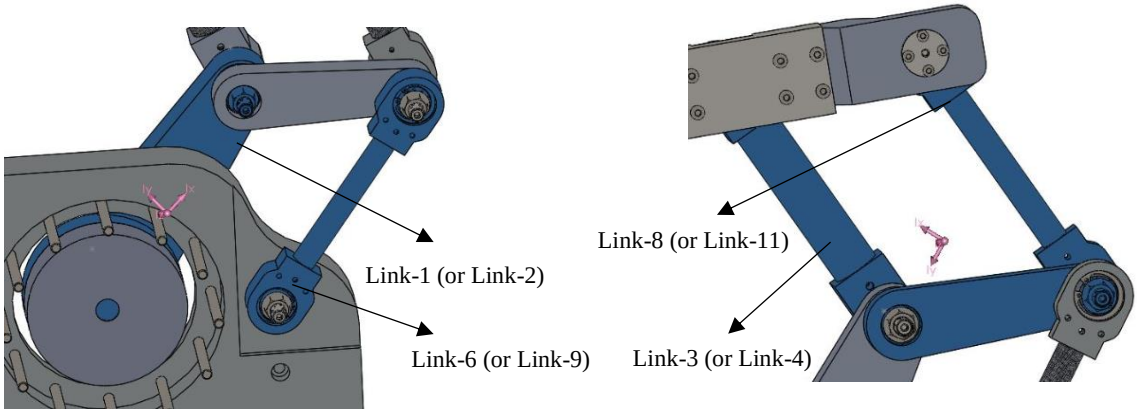

Figure 3.6. SolidWorks view of (a) the masses lumped as m_{11} (or m_{21}), (b) the masses lumped as m_{12} (or m_{22}).

When the total linear momentum of the mechanism is equated to zero, the shaking forces are balanced. The balancing masses (m_{bmi}) and their locations (P_{bmi}) are obtained from the linear momentum equations. The positions and velocities of the link mass centers are derived with respect to coordinate axes of the mechanism in Equations 3.20-24. Linear momentum equation is firstly expressed with the link masses and velocity terms in Equations 3.25-26. Then, the positions and velocities of the balancing masses are derived with respect to coordinate axes of the mechanism in Equations 3.27-28.

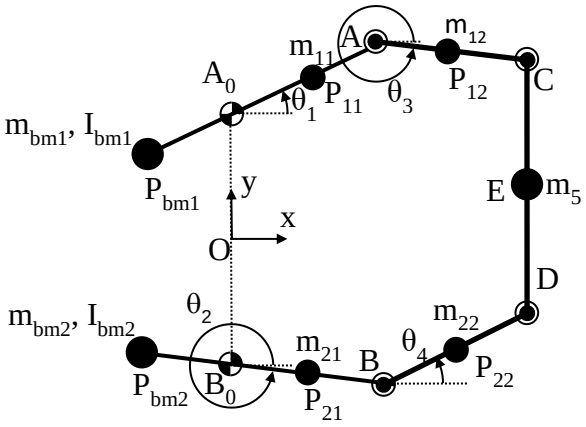

$|A_0P_{bm1}| = |B_0P_{bm2}| = p_{bm}$

$|A_0B_0| = |CD| = a$

$|A_0P_{11}| = |B_0P_{21}| = p_1$

$|AP_{12}| = |BP_{22}| = p_2$

$m_{11} = m_{21} = m_1$

$m_{12} = m_{22} = m_2$

$m_{bm1} = m_{bm2} = m_{bm}$

Figure 3.7. The force balancing model of the mechanism.

Linear momentum equation is then expressed with the balancing masses and velocity terms in Equations 29-30. Thus, the required mass of balancing masses and their locations can be calculated when Equation 3.26 is equated to Equation 3.30 to obtain the balancing condition expressed in Equation 3.31. In Equations 3.20-31, $\vec{r}$ represents the position of mass center in complex number form; $\bar{r}$ represents the position of mass center in matrix form; $\dot{\bar{r}}$ represents the velocity of mass center in matrix form; $\bar{L}$ represents the total linear momentum.

$$\vec{r}_5 = re^{i\theta_1} + re^{i\theta_2} \Rightarrow \bar{r}_5 = \begin{bmatrix} rc\theta_1 + rc\theta_2 \\ rs\theta_1 + rs\theta_2 \end{bmatrix} \Rightarrow \dot{\bar{r}}_5 = \begin{bmatrix} -rs\theta_1\dot{\theta}_1 - rs\theta_2\dot{\theta}_2 \\ rc\theta_1\dot{\theta}_1 + rc\theta_2\dot{\theta}_2 \end{bmatrix} \tag{3.20}$$

$$\overrightarrow{r_{P_{11}}} = p_1e^{i\theta_1} \Rightarrow \overline{r_{P_{11}}} = \begin{bmatrix} p_1c\theta_1 \\ p_1s\theta_1 \end{bmatrix} \Rightarrow \dot{\overline{r}}_{P_{11}} = \begin{bmatrix} -p_1s\theta_1\dot{\theta}_1 \\ p_1c\theta_1\dot{\theta}_1 \end{bmatrix} \tag{3.21}$$

$$\overrightarrow{r_{P_{21}}} = p_1e^{i\theta_2} \Rightarrow \overline{r_{P_{21}}} = \begin{bmatrix} p_1c\theta_2 \\ p_1s\theta_2 \end{bmatrix} \Rightarrow \dot{\overline{r}}_{P_{21}} = \begin{bmatrix} -p_1s\theta_2\dot{\theta}_2 \\ p_1c\theta_2\dot{\theta}_2 \end{bmatrix} \tag{3.22}$$

$$\overrightarrow{r_{P_{12}}} = re^{i\theta_1} + p_2e^{i\theta_2} \Rightarrow \overline{r_{P_{12}}} = \begin{bmatrix} rc\theta_1 + p_2c\theta_2 \\ rs\theta_1 + p_2s\theta_2 \end{bmatrix} \Rightarrow \dot{\overline{r}}_{P_{12}} = \begin{bmatrix} -rs\theta_1\dot{\theta}_1 - p_2s\theta_2\dot{\theta}_2 \\ rc\theta_1\dot{\theta}_1 + p_2c\theta_2\dot{\theta}_2 \end{bmatrix} \tag{3.23}$$

$$\overrightarrow{r_{P_{22}}} = re^{i\theta_2} + p_2e^{i\theta_1} \Rightarrow \overline{r_{P_{22}}} = \begin{bmatrix} rc\theta_2 + p_2c\theta_1 \\ rs\theta_2 + p_2s\theta_1 \end{bmatrix} \Rightarrow \dot{\overline{r}}_{P_{22}} = \begin{bmatrix} -rs\theta_2\dot{\theta}_2 - p_2s\theta_1\dot{\theta}_1 \\ rc\theta_2\dot{\theta}_2 + p_2c\theta_1\dot{\theta}_1 \end{bmatrix} \tag{3.24}$$

$$\bar{L} = m_1 \dot{\bar{r}}_{P_{11}} + m_2 \dot{\bar{r}}_{P_{12}} + m_5 \dot{\bar{r}}_5 + m_1 \dot{\bar{r}}_{P_{21}} + m_2 \dot{\bar{r}}_{P_{22}} \tag{3.25}$$

$$\bar{L} = \begin{bmatrix} (-m_1 p_1 - (m_2 + m_5) r - m_2 p_2) s\theta_1 \\ (m_1 p_1 + (m_2 + m_5) r + m_2 p_2) c\theta_1 \end{bmatrix} \dot{\theta}_1 + \begin{bmatrix} (-m_2 p_2 - (m_5 + m_2) r - m_1 p_1) s\theta_2 \\ (m_2 p_2 + (m_5 + m_2) r + m_1 p_1) c\theta_2 \end{bmatrix} \dot{\theta}_2 \tag{3.26}$$

$$\overrightarrow{r_{P_{bm1}}} = p_{bm} e^{i\theta_1} \Rightarrow \overline{r_{P_{bm1}}} = \begin{bmatrix} p_{bm} c\theta_1 \\ p_{bm} s\theta_1 \end{bmatrix} \Rightarrow \dot{\overline{r}}_{P_{bm1}} = \begin{bmatrix} -p_{bm} s\theta_1 \dot{\theta}_1 \\ p_{bm} c\theta_1 \dot{\theta}_1 \end{bmatrix} \tag{3.27}$$

$$\overrightarrow{r_{P_{bm2}}} = p_{bm} e^{i\theta_2} \Rightarrow \overline{r_{P_{bm2}}} = \begin{bmatrix} p_{bm} c\theta_2 \\ p_{bm} s\theta_2 \end{bmatrix} \Rightarrow \dot{\overline{r}}_{P_{bm2}} = \begin{bmatrix} -p_{bm} s\theta_2 \dot{\theta}_2 \\ p_{bm} c\theta_2 \dot{\theta}_2 \end{bmatrix} \tag{3.28}$$

$$\bar{L} = m_{bm1} \dot{\bar{r}}_{P_{bm1}} + m_{bm2} \dot{\bar{r}}_{P_{bm2}} \tag{3.29}$$

$$\bar{L} = \begin{bmatrix} -m_{bm} p_{bm} s\theta_1 \\ m_{bm} p_{bm} c\theta_1 \end{bmatrix} \dot{\theta}_1 + \begin{bmatrix} -m_{bm} p_{bm} s\theta_2 \\ m_{bm} p_{bm} c\theta_2 \end{bmatrix} \dot{\theta}_2 \tag{3.30}$$

$$m_1 p_1 + (m_2 + m_5) r + m_2 p_2 = m_{bm} p_{bm} \tag{3.31}$$

Since the mechanism is symmetrical with respect to the x-axis, Equation 3.30 holds for either of the balancing masses $m_{bm1} = m_{bm2} = m_{bm}$ with the same distance parameter p_{bm}.

3.4. Dynamic Model

Two different analytical models have been created for the dynamic model by using the vector dynamics and Lagrange method in order to compare and ensure the correctness of the results. The over-constrained 6R mechanism is stiffer and symmetrical, but the reaction forces cannot be calculated with the vector dynamics because of over-constraint. Therefore, the dynamic models are derived for the simply constrained mechanism (Figure 3.8). The mass distribution of links and the mass for the balancing of mechanism (m_{bm1}, m_{bm2}) are shown in Figure 3.7 and are explained in detail in Section 3.3 Masses of links 2 and 6 are lumped on link 2, whereas masses of links 4 and 8 are lumped on link 4.

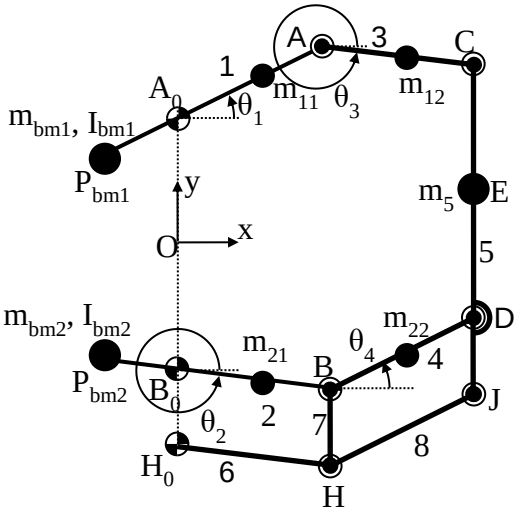

$$|A_0A| = |AC| = |B_0B| = |BD| = |H_0H| = r$$
$$|B_0H_0| = |BH| = |DJ|$$
$$|OA_0| = |OB_0| = |EC| = |ED| = a/2$$
$$|A_0P_{bm2}| = |B_0P_{bm2}| = p$$
$$\angle A_0B_0H_0 = \angle CDJ$$

Figure 3.8. Simply constrained 6R mechanism.

3.4.1. Vector Dynamics

The force equilibrium equations are derived to calculate the required motor torque and the reaction forces under the influence of high inertial forces with drawing free body diagrams of the mechanism (Figure 3.9).

Dynamic equilibrium equations:

For Link 1 in Equation 3.32:

$$\begin{aligned} F_{01x} &= F_{13x} + m_{bm1}a_{1x} + m_{11}a_{11x} \\ F_{01y} &= F_{13y} + m_{bm1}a_{1y} + m_{11}a_{11y} \\ T_1 &= (p_{bm1}m_{bm1}a_{1x} - p_{11}m_{11}a_{11x} - rF_{13x})s\theta_1 \\ &\quad - (p_{bm1}m_{bm1}a_{1y} - p_{11}m_{11}a_{11y} - rF_{13y})c\theta_1 + (I_{cm1} + I_{11})\alpha_1 \end{aligned} \tag{3.32}$$

For Link 2 in Equation 3.33:

$$\begin{aligned} F_{02x} &= F_{B4x} + m_{bm2}a_{2x} + m_{21}a_{21x} \\ F_{02y} &= F_{2By} + m_{bm2}a_{2y} + m_{21}a_{21y} \\ T_2 &= (p_{bm2}m_{bm2}a_{2x} - p_{21}m_{21}a_{21x} - rF_{B4x})s\theta_2 \\ &\quad - (p_{bm2}m_{bm2}a_{2y} - p_{21}m_{21}a_{21y} - rF_{2By})c\theta_2 + (I_{bm2} + I_{21})\alpha_2 \end{aligned} \tag{3.33}$$

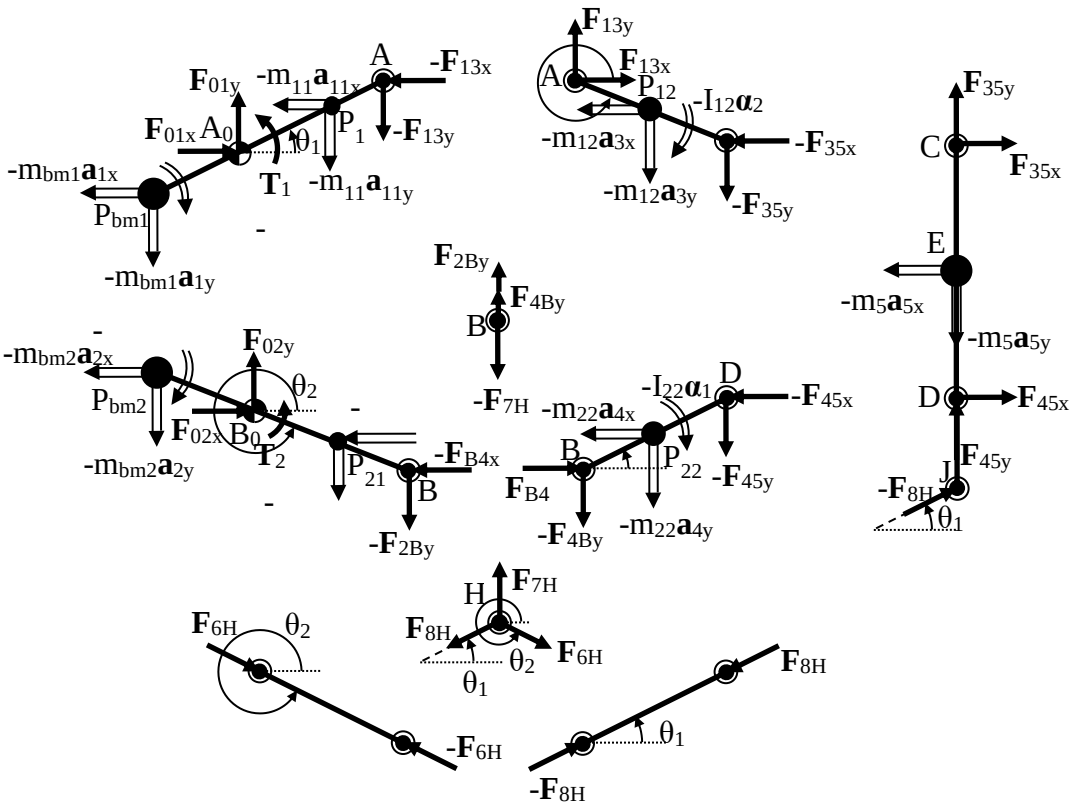

Figure 3.9. Free body diagrams of the mechanism links.

For Link 3 in Equation 3.34:

$$
\begin{aligned}
&F_{13x} = F_{35x} + m_{12}a_{3x} \\
&F_{13y} = F_{35y} + m_{12}a_{3y} \\
&-I_{12}\alpha_2 - r(\tfrac{1}{2}m_{12}a_{3y} + F_{35y})c\theta_2 + r(\tfrac{1}{2}m_{12}a_{3x} + F_{35x})s\theta_2 = 0
\end{aligned}
\tag{3.34}
$$

For Link 4 in Equation 3.35:

$$
\begin{aligned}
&F_{B4x} = F_{45x} + m_{22}a_{4x} \\
&F_{4By} = -F_{45y} - m_{22}a_{4y} \\
&-I_{22}\alpha_1 - r(\tfrac{1}{2}m_{22}a_{4y} + F_{45y})c\theta_1 + r(\tfrac{1}{2}m_{22}a_{4x} + F_{45x})s\theta_1 = 0
\end{aligned}
\tag{3.35}
$$

For Link 5 in Equation 3.36:

$$
\begin{aligned}
&F_{35x} + F_{45x} + F_{8H}c\theta_1 = m_5a_{5x} \\
&F_{35y} + F_{45y} + F_{8H}s\theta_1 = m_5a_{5y} \\
&-aF_{35x} + \tfrac{1}{2}am_5a_{5x} + bF_{8H}\cos\theta_1 = 0
\end{aligned}
\tag{3.36}
$$

For Joints H and B in Equation 3.37:

$$\begin{aligned} F_{6H}c\theta_2 &= F_{8H}c\theta_1 \\ F_{6H}s\theta_2 - F_{8H}s\theta_1 + F_{7H} &= 0 \\ F_{2By} + F_{4By} &= F_{7H} \end{aligned} \tag{3.37}$$

A matrix is created using the force/moment equations of link 5 and the moment equations of links 3 and 4. The inverse of this matrix gives F_{35x}, F_{35y}, F_{45x}, F_{45y} and F_{8H}.

$$\begin{bmatrix} rs\theta_2 & -rc\theta_2 & 0 & 0 & 0 \\ 1 & 0 & 1 & 0 & c\theta_1 \\ 0 & 1 & 0 & 1 & s\theta_1 \\ a & 0 & 0 & 0 & -bc\theta_1 \\ 0 & 0 & rs\theta_1 & -rc\theta_1 & 0 \end{bmatrix} \begin{bmatrix} F_{35x} \\ F_{35y} \\ F_{45x} \\ F_{45y} \\ F_{8H} \end{bmatrix} = \begin{bmatrix} I_{12}\alpha_2 - \tfrac{1}{2}rm_{12}\left(a_{3x}s\theta_2 - a_{3y}c\theta_2\right) \\ m_5a_{5x} \\ m_5a_{5y} \\ \tfrac{1}{2}am_5a_{5x} \\ I_{22}\alpha_1 - \tfrac{1}{2}rm_{22}\left(a_{4x}s\theta_1 - a_{4y}c\theta_1\right) \end{bmatrix}$$

After that, F13x, F_{13y}, F_{B4x} and F_{B4y} are found from the force equations of links 3 and 4. F_{6H}, F_{7H} and F_{2By} are found from the equations of joints B and H. The equilibrium equations of link 1 give F_{01x}, F_{01y} and T_1; the equilibrium equations of link 2 give F_{02x}, F_{02y}, T_2.

3.4.2. Analytical Dynamics

In this section, the equation of motion is derived using Lagrange method. The model in Figure 3.7 is also used for the Lagrange method.

The total kinetic energy of the system ($m_{11} = m_{21} = m_1$; $m_{12} = m_{22} = m_2$; $I_{11} = I_{21} = I_1$; $I_{12} = I_{22} = I_2$):

$$KE = \frac{1}{2}\begin{bmatrix} m_5v_5^{\,2} + m_1\left(v_{P_{11}}^{\,2} + v_{P_{21}}^{\,2}\right) + m_2\left(v_{P_{12}}^{\,2} + v_{P_{22}}^{\,2}\right) \\ + m_{bm}\left(v_{P_{bm1}}^{\,2} + v_{P_{bm2}}^{\,2}\right) + \left(I_{bm} + I_1 + I_2\right)\left(\omega_1^{\,2} + \omega_2^{\,2}\right) \end{bmatrix} \tag{3.38}$$

The velocity expressions ($|A_0P_{bm1}| = |B_0P_{bm2}| = p_0$, $|A_0P_{11}| = |B_0P_{21}| = p_1$, $|AP_{12}| = |BP_{22}| = p_2$):

$$V_{P_{bm1}} = p_0\omega_1,\ V_{P_{bm2}} = p_0\omega_2,\ V_{P_{11}} = p_1\omega_1,\ V_{P_{21}} = p_1\omega_2 \tag{3.39}$$

$$\vec{r_5} = re^{i\theta_1} + re^{i\theta_2} \Rightarrow V_5 = \left|ir(e^{i\theta_1}\omega_1 + e^{i\theta_2}\omega_2)\right| = r\sqrt{\omega_1^{\,2} + \omega_2^{\,2} + 2c(\theta_1 - \theta_2)\omega_1\omega_2} \tag{3.40}$$

$$\overrightarrow{r_{P_{12}}} = re^{i\theta_1} + p_2 e^{i\theta_2} \Rightarrow V_{P_{12}} = \left|ire^{i\theta_1}\omega_1 + ip_2 e^{i\theta_2}\omega_2\right| = \sqrt{r^2\omega_1^{\,2} + p_2^{\,2}\omega_2^{\,2} + 2rp\omega_1\omega_2\, c(\theta_1 - \theta_2)} \tag{3.41}$$

$$\overrightarrow{r_{P_{22}}} = re^{i\theta_2} + p_2 e^{i\theta_1} \Rightarrow V_{P_{22}} = \left|ire^{i\theta_2}\omega_2 + ip_2 e^{i\theta_1}\omega_1\right| = \sqrt{r^2\omega_2^{\,2} + p_2^{\,2}\omega_1^{\,2} + 2rp\omega_1\omega_2\, c(\theta_1 - \theta_2)} \tag{3.42}$$

The total kinetic energy of the system with open state of velocity equations:

$$KE = \frac{1}{2}\left[\begin{array}{l}\left(m_5r^2 + m_1p_1^{\,2} + m_{bm}p_{bm}^{\,2} + m_2(r^2 + p_2^{\,2})\right)\left(\omega_1^{\,2} + \omega_2^{\,2}\right) + \\ (m_5r^2 + 2m_2rp_2)(2c(\theta_1 - \theta_2)\omega_1\omega_2 + \left(I_{bm} + I_1 + I_2\right)\left(\omega_1^{\,2} + \omega_2^{\,2}\right)\end{array}\right] \tag{3.43}$$

Partial derivatives are taken with respect to position angle in Equation 3.44;

$$\begin{aligned}\frac{\partial KE}{\partial\theta_1} &= -(m_5r^2 + 2m_2rp_2)\,s(\theta_1 - \theta_2)\omega_1\omega_2 \\ \frac{\partial KE}{\partial\theta_2} &= (m_5r^2 + 2m_2rp_2)\,s(\theta_1 - \theta_2)\omega_1\omega_2\end{aligned} \tag{3.44}$$

with respect to angular velocity in Equation 3.45;

$$\begin{aligned}\frac{\partial KE}{\partial\omega_1} &= \left[m_5r^2 + m_1p_1^{\,2} + m_{bm}p_{bm}^{\,2} + m_2(r^2 + p_2^{\,2}) + I_{bm} + I_1 + I_2\right]\omega_1 \\ &\quad + (m_5r^2 + 2m_2rp_2)\,c(\theta_1 - \theta_2)\omega_2 \\ \frac{\partial KE}{\partial\omega_2} &= \left[m_5r^2 + m_1p_1^{\,2} + m_{bm}p_{bm}^{\,2} + m_2(r^2 + p_2^{\,2}) + I_{bm} + I_1 + I_2\right]\omega_2 \\ &\quad + (m_5r^2 + 2m_2rp_2)\,c(\theta_1 - \theta_2)\omega_1\end{aligned} \tag{3.45}$$

with respect to time in Equation 3.46 and 3.47:

$$\begin{aligned}\frac{d}{dt}\frac{\partial KE}{\partial\omega_1} &= \left[m_5r^2 + m_1p_1^{\,2} + m_{bm}p_{bm}^{\,2} + m_2(r^2 + p_2^{\,2}) + I_{bm} + I_1 + I_2\right]\alpha_1 \\ &\quad + (m_5r^2 + 2m_2rp_2)\,c(\theta_1 - \theta_2)\alpha_2 \\ &\quad - (m_5r^2 + 2m_2rp_2)\,s(\theta_1 - \theta_2)(\omega_1 - \omega_2)\omega_2\end{aligned} \tag{3.46}$$

$$\frac{d}{dt}\frac{\partial KE}{\partial \omega_2} = \left[m_5 r^2 + m_1 p_1^{\,2} + m_{bm} p_{bm}^{\,2} + m_2 (r^2 + p_2^{\,2}) + I_{bm} + I_1 + I_2 \right] \alpha_2$$
$$+ (m_5 r^2 + 2 m_2 r p_2)\, c(\theta_1 - \theta_2)\alpha_1 \qquad (3.47)$$
$$- (m_5 r^2 + 2 m_2 r p_2)\, s(\theta_1 - \theta_2)(\omega_1 - \omega_2)\omega_1$$

Lagrange Equations for the torques of actuators:

$$\frac{d}{dt}\frac{\partial KE}{\partial \omega_1} - \frac{\partial KE}{\partial \theta_1} = T_1$$
$$\frac{d}{dt}\frac{\partial KE}{\partial \omega_2} - \frac{\partial KE}{\partial \theta_2} = T_2 \qquad (3.48)$$

Actuations torques are solved from Lagrange equations:

$$T_1 = \left[m_5 r^2 + m_1 p_1^{\,2} + m_{bm} p_{bm}^{\,2} + m_2 (r^2 + p_2^{\,2}) + I_{bm} + I_1 + I_2 \right] \alpha_1$$
$$+ (m_5 r^2 + 2 m_2 r p_2) \left[c(\theta_1 - \theta_2)\alpha_2 + s(\theta_1 - \theta_2)\omega_2^{\,2} \right] \qquad (3.49)$$

$$T_2 = \left[m_5 r^2 + m_1 p_1^{\,2} + m_{bm} p_{bm}^{\,2} + m_2 (r^2 + p_2^{\,2}) + I_{bm} + I_1 + I_2 \right] \alpha_2$$
$$+ (m_5 r^2 + 2 m_2 r p_2) \left[c(\theta_1 - \theta_2)\alpha_1 - s(\theta_1 - \theta_2)\omega_1^{\,2} \right] \qquad (3.50)$$

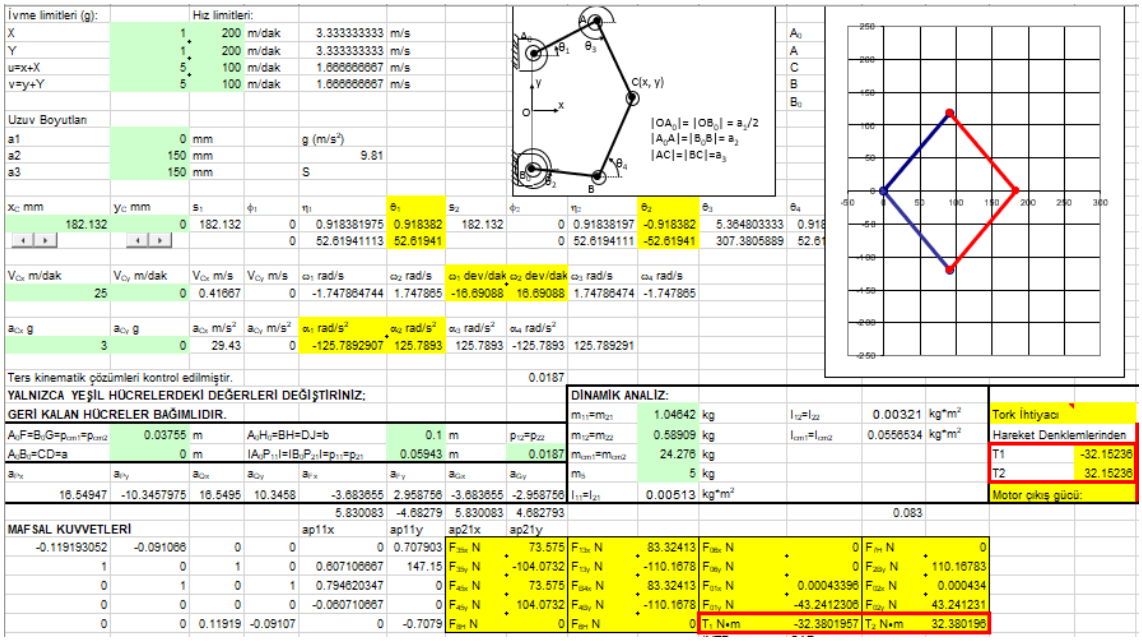

Figure 3.10. The Excel file for dynamic analysis.

The torque values obtained by the Lagrange method and the torque values from the equilibrium equations were compared to verify mathematical models of the system. An Excel file (Figure 3.10) was created for calculations. In accordance with the mass and moment of inertia created by 5 kg platform and the structural design, and with full shaking force balancing, the maximum torque requirement under high acceleration conditions are re-calculated after the constructional design study of the mechanism. A Matlab Simulink model and an MSC ADAMS model is also constructed for the mechanism. It is seen that the simulation results are in accordance with each other.

CHAPTER 4

CAD MODEL OF THE MECHANISMS

Examples of the prototype of 2-dof 5R mechanism are examined to design of the mechanism for this study. These examples are Mitsubishi RP series (Figielski et al., 2007), DexTAR (Compas et al., 2010), PARVUS (Burisch et al., 2007), Par2 (Pierrot et al., 2011), the PALAPLACER (Helm et al., 2006) mentioned in the literature survey and SFB 562 (Schütz et al., 2010) and the protype study of delta robot in (Dinçer, 2017). When RP-AH1 of Mitsubishi RP series is similar about link dimension, RP-AH5 is similar about carrying capacity to the designed mechanism. Prototypes of mechanisms in (Schütz et al., 2010) and (Dinçer, 2017) show that composite tubes can be used for the links (Figure 4.1). The use of composite tube is also considered for this study to decrease mass with high strength material.

(a) (b)

Figure 4.1. Prototype of (a) SFB 562 mechanism (Source: Schütz et al., 2010), (b) the delta mechanism (Source: Dinçer, 2017).

The CAD model of over-constrained mechanism (Figure 4.2) and simply constrained mechanism are constructed in SolidWorks environment. In this section, CAD model, material and connection elements of all mechanism parts are explained in detail. In general, motors are placed on the base so that they do not carry load. The support group and base, the arms, the platform and its parts, the balancing masses are explained for over- and simply constrained mechanisms as the following subsections. A link of one of the parallelogram loops is removed from the over-constrained mechanism to obtain simply

constrained one as mentioned in Section 3.1. Therefore, the simply constrained mechanism is also presented in Section 4.4.

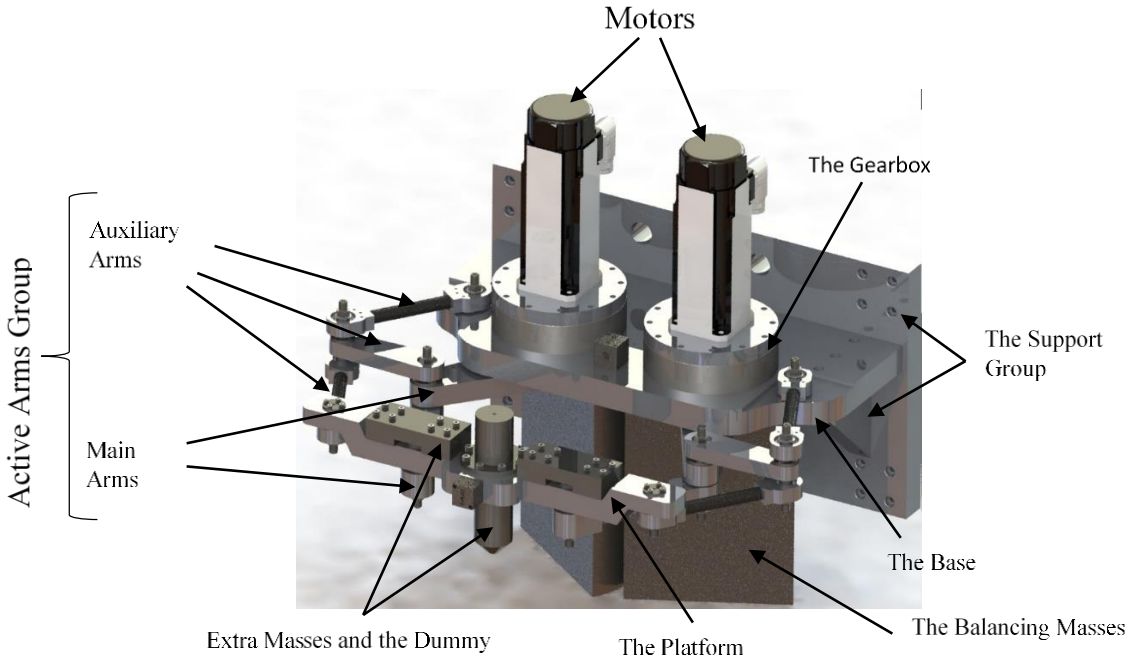

Figure 4.2. The over-constrained 6R mechanism design.

4.1. The Support Group and the Base

The support group consists of four parts which are made from Al 5000 series. 285x493x30 mm^3 plate (support-1 in Figure 4.3) is designed to fix the mechanism to the table (which weighs 500 kg) with four holes on all corners (showed with "1"). The base is also assembled to the plate with six holes (showed with "2") located in the middle. Two holes (numbered with "3") are opened for cables of motors. Twelve holes (located under the connection of the base) are used to connect to three support parts which are used to bear bending moments.

Two support-2 parts (Figure 4.4 (a)) are used. They are connected to support-1 with their faces (numbered with "2"). Support-3 (Figure 4.4 (b)) is assembled to support-1 with its face (numbered with "2"). Other faces (numbered with "1") are used to connect to the base. These support parts help to the base when carrying the motors. There are only dimensional differences between support-2 and support-3.

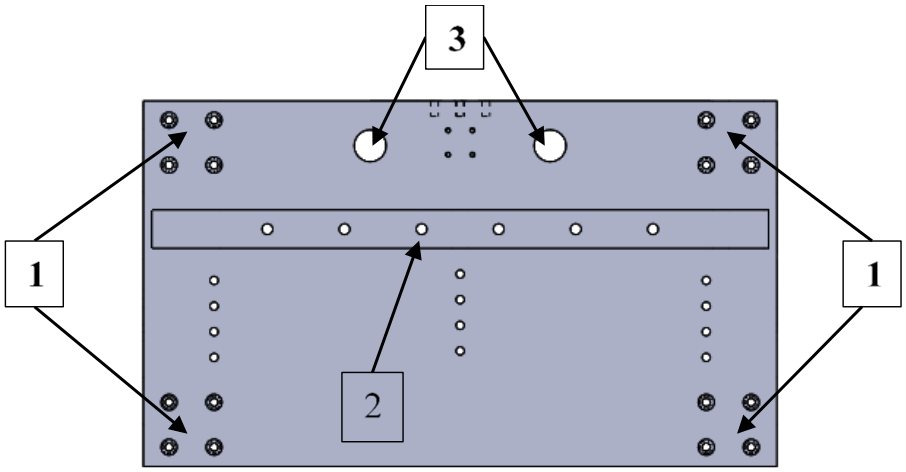

Figure 4.3. Support-1: The plate is to provide the connection of the base and the table.

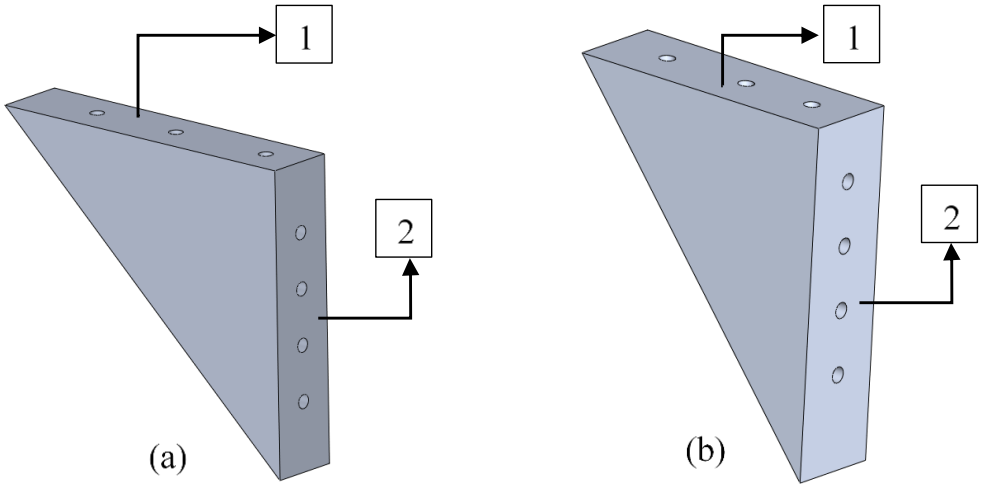

Figure 4.4. (a) Support-2, (b) support-3.

The base (Figure 4.5 (a)) is connected to support parts to holes showed with "1". Two holes (with numbered "2") are shaft holes which are used for shaft-1 (Figure 4.5 (b)). The material is removed from the faces in which the shaft holes located to prevent interference between the base and link type 1.

Motors are placed in the big two holes (designated with "3"). Motor flanges are connected to the base with twelve holes on the circular path. One of the important points for the design of the base is that there should be 180 mm between the fixed revolute joints. There must be 180 mm between the center of two motor shafts to provide this. Moreover, there must be 100 mm between shaft-1 and the motor shaft. These dimensions are

determined with consideration of the workspace of mechanism (which is 150 x 100 mm) and the interference between motors and link type 2.

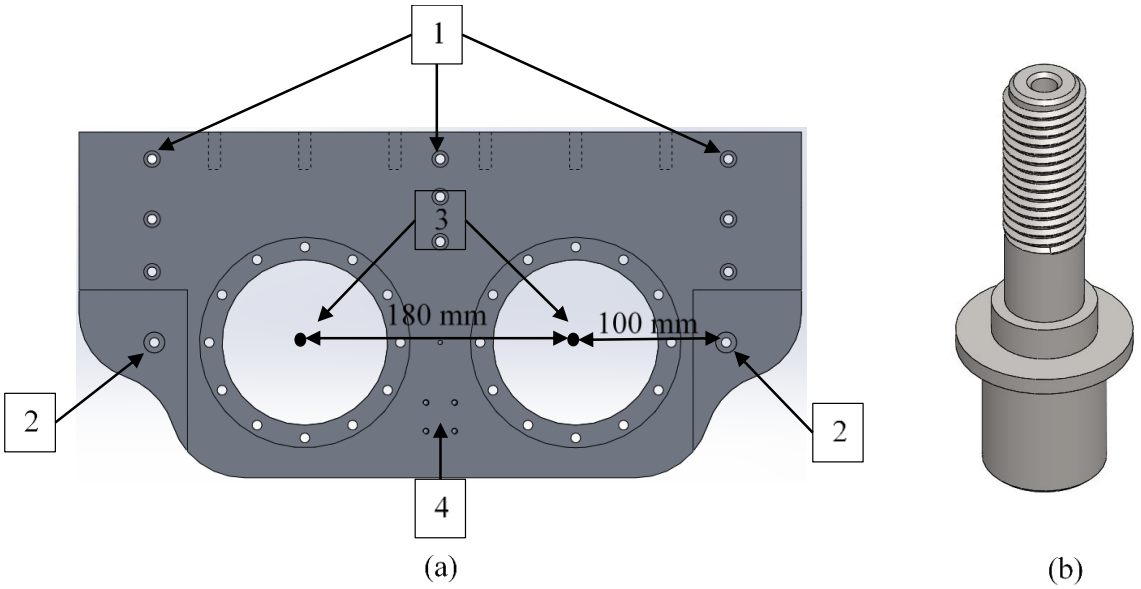

Figure 4.5. (a) The base, (b) shaft-1.

The relationships between the above described parts can be understood from the exploded assembly view of support group and the base (Figure 4.6).

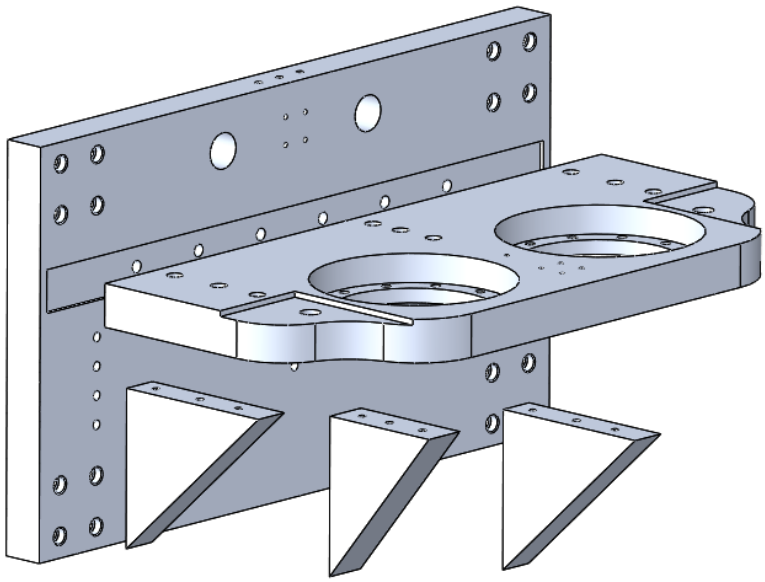

Figure 4.6. The exploded assembly view of support group and the base.

4.2. The Arms

The arms can be divided into main arms and auxiliary arms. The main arms form the main structure of the mechanism, whereas the auxiliary arms are used to create parallelograms. Two different types of main arm and auxiliary arm design are available. One of main arms is connected to motor flange and the other is assembled to platform (Figure 4.7). There are three auxiliary arms. One of them is called as intermediate arm which provides connection between the main arms and other two auxiliary arms which have same constructional details. One of them is between the base and the intermediate arm. Other is between the intermediate arm and the platform.

Al 7000 series was used for all metal parts of active arms. Carbon-fiber composite material was preferred for the tubes. The links remain under the influence of axial and radial forces because of the movement of the mechanism. Therefore, carbon-fiber tube which is made from 0^0-90^0 fabric woven was selected. All shafts are designed with 1040 steel material.

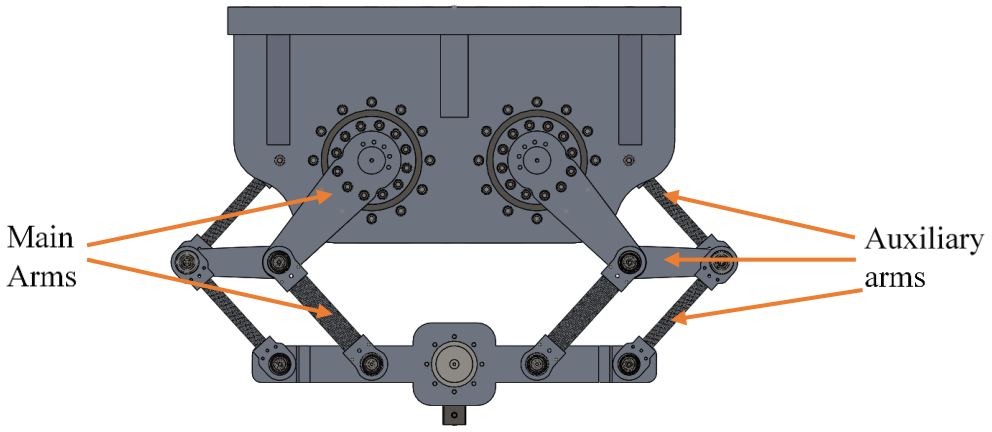

Figure 4.7. Bottom view of the mechanism.

4.2.1. Auxiliary Arms

A type of the auxiliary arms is link type 1 (Figure 4.8) and the four arms of the mechanisms are of this type. It is composed of two metal joints and a composite tube. The composite tube has 10 mm inner diameter and 14 mm outer diameter. There are two types

of bearings embedded in metal joints. One of them is a deep grove ball bearing and the other is a spherical roller bearing. Spherical roller bearings are used in order to release some of the stress during the motion of the mechanism. M24 segments are used to prevent the bearings from slipping. One of the important design details is to glue composite tube with two metal joints for link type 1 and also for link type 3 to be explained later on. The composite tube is inserted into the two metal parts up to 15 mm. Split pin holes of 3 mm diameter are drilled in order to get more robust connection when the composite tube is glued from these surfaces.

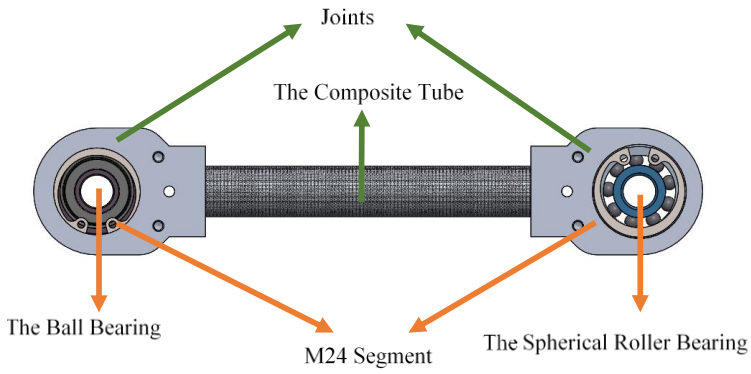

Figure 4.8. Link type 1.

One of joint connections of intermediate link (Figure 4.9) has a ball bearing. The other connection is provided by press-fitting of the shaft. The distance between the two revolute joints of the intermediate arm must be the same as the distance between link type 1 and the motor shafts to provide a parallelogram.

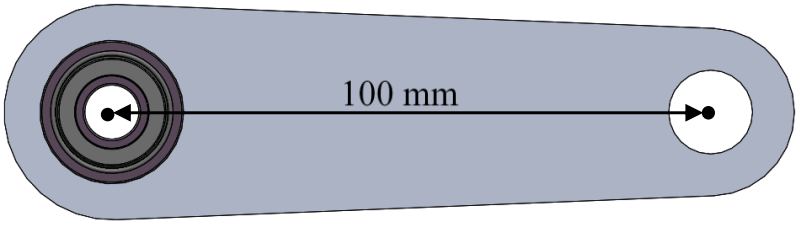

Figure 4.9. The intermediate link.

Two shafts which are connected to the intermediate arm can be seen in Figure 4.10. Shaft-2 (Figure 4.10 (a)) is connected to the intermediate link inside the bearing. This shaft is fixed to link type 2 (Figure 4.11). Shaft-3 (Figure 4.10 (b)) is designed to be fixed to the intermediate link.

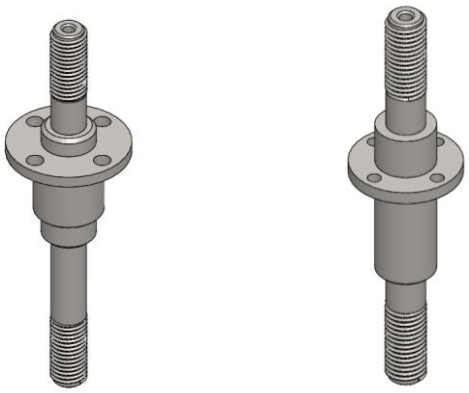

Figure 4.10. (a) Shaft-2, (b) shaft-3.

4.2.2. Main Arms

Link type 2 (Figure 4.11) is the arm connected to the motor. The holes (numbered "1") allow the connection of the gearbox flange with M6 bolts. In fact, the detail corresponding to the gearbox flange could be designed separately from this link. However, it is thought that the monolithic design will require less fasteners and mounting accuracy. The detail (showed with "2") is combined with the moving surface of the gearbox to transfer the movement from the motor to link type 2. Five holes (numbered with "3") are opened in order to connect the balancing masses with M5 bolts. Shaft-2 is designed to be fixed to link type 2 at the point indicated by "4" and M4 bolts are used.

Link type 3 (Figure 4.12) has similar properties of link type 1 in terms of the design details. There are dimensional differences between the two links. One of them is to use a composite tube with higher thickness (3 mm). Because this link is the main link which carries higher load compared to auxiliary arms. In addition, deep grove ball bearing is used for both joints of the link.

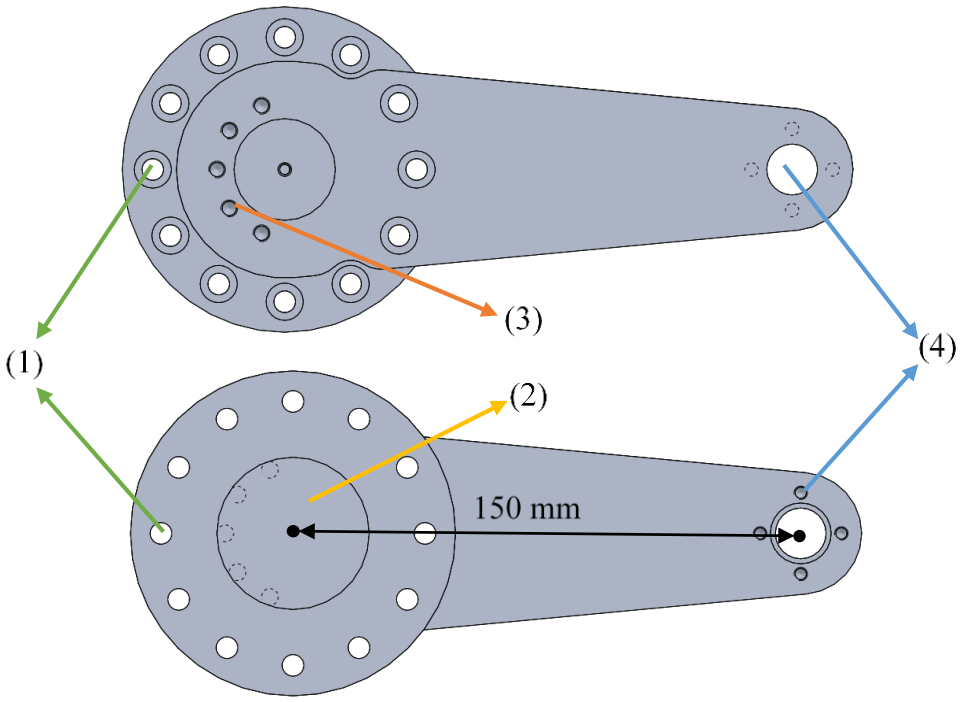

Figure 4.11. Link type 2: is connected to the motor.

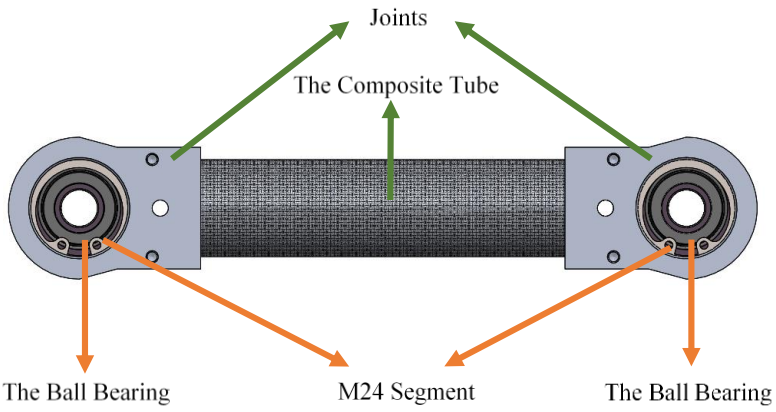

Figure 4.12. Link type 3.

4.3. Platform Group

The main part of this group is platform which is made from Al 7000 series (Figure 4.13 (a)). The type 1 links connected to the platform are connected at holes numbered with “1” on the platform. Type 3 links are connected to the platform at holes numbered with “2”. The end-effector is assembled to the hole numbered with “3”.

There are eight holes numbered with “5” on both sides of hole “2”. These are used to connect extra masses (Figure 4.13 (b)). The purpose of connecting extra masses is to obtain 5 kg of total platform masses. Because one of the thesis criteria is to have 5 kg payload.

The other extra masses are designed as a dummy of end-effector (Figure 4.13 (c)). The important thing is to not disrupt the mass distribution of the mechanism at this point. The dummy will be used before the studies to be carried out with the laser head (end-effector). The dummy and extra masses are made from 1040 steel.

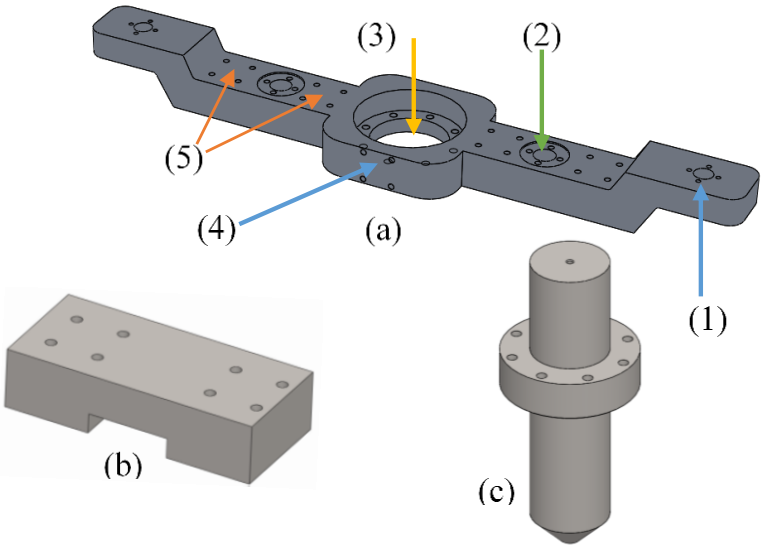

Figure 4.13. Platform Group: (a) Platform, (b) Extra mass, (c) The dummy of end-effector.

Shaft-4 (Figure 4.14 (a)) and shaft-5 (Figure 4.14 (b)) are fixed to the platform by press-fitting and also with M3 bolts.

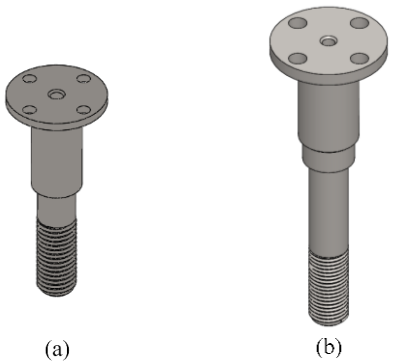

Figure 4.14. (a) Shaft-4, (b) Shaft-5.

4.4. The Simply Constrained Mechanism

When a link of a parallelogram loop is removed from the over-constrained mechanism, it becomes a simply constrained mechanism. Therefore, one of the auxiliary distal links is removed. After that, additional masses are needed to achieve symmetrical mass distribution of the mechanism. Thus, there will be no changing in the calculations for the balancing masses.

Two parts were designed as additional masses which are connected to shafts instead of joints of the removed link as can be seen as circled in Figure 4.15. The inner and outer diameter were determined as 9 mm and 30 mm. The height of the parts will be determined after the manufacturing of link type 3. The material of the parts is 1040 steel.

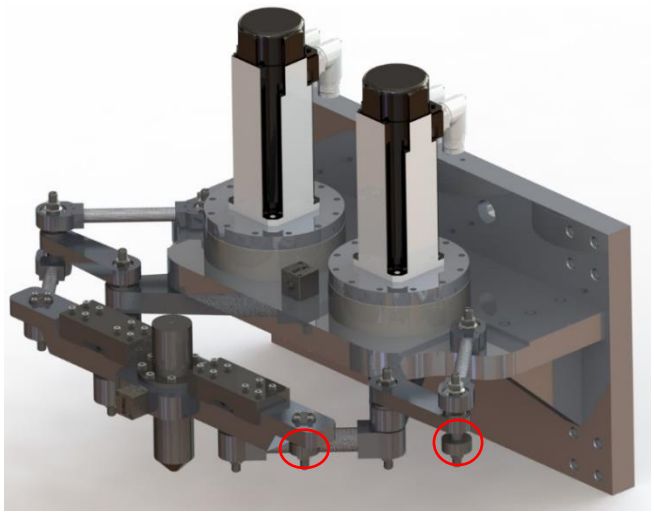

Figure 4.15. The simply constrained 6R mechanism.

4.5. The Balancing Masses

The balancing masses are designed in four parts to see the vibration which affects the base against the different values of balancing masses, when the balancing test are performed. It was observed that the mechanism will be tested under at least 3 different conditions when deciding on the masses of four parts. These conditions are: 1) when the end-effector of the mechanism is not assembled, 2) when the end-effector is assembled, 3) when the platform group total mass is 5 kg. On the other hand, since the balancing

masses can be connected to each other in different configurations, it is planned to make different experiments in terms of partial balancing.

Firstly, the distance (180 mm in Figure 4.16) between the centers of the two link type 2 was examined to design the largest diameter of balancing masses. The distance between the masses was determined to be 8 mm in order to prevent interference of the balancing masses with each other. Thus, the diameter of the balancing masses is 172 mm.

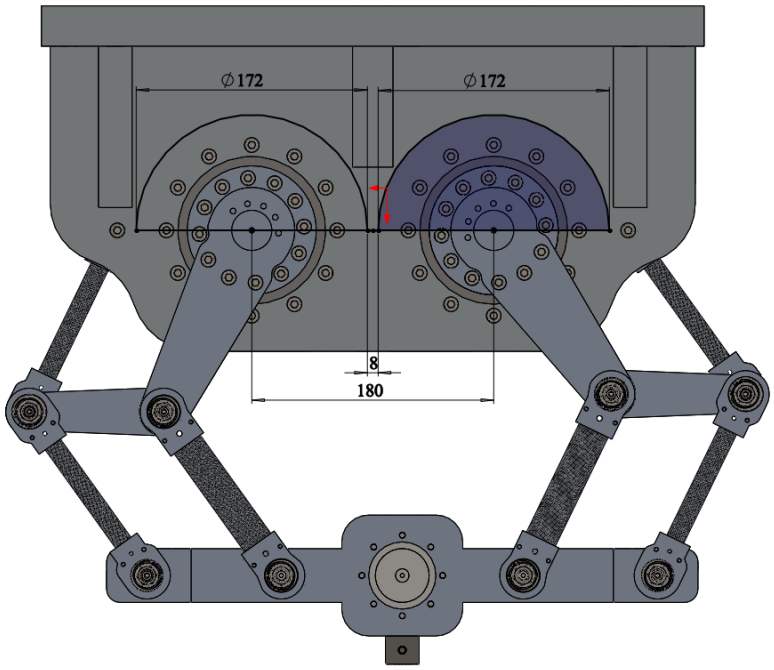

Figure 4.16. The design detail of balancing masses.

After that, mass values are taken from SolidWorks CAD model for the test situations to determine balancing masses values. According to this, the total height of balancing masses was found about 27 cm. It was decided to design the balancing masses in 4 parts (Figure 4.17). However, it was decided to revise the heights of the balancing masses after the parts of the mechanism were produced, since there would be differences between the mass values taken from SolidWorks and the mass values of the produced parts.

The balancing mass M_1 (Figure 4.17) has two different types of holes for bolts. It is connected to link type 2 with M5 bolts. M8 stud holes are drilled so that all masses can be connected to each other as desired.

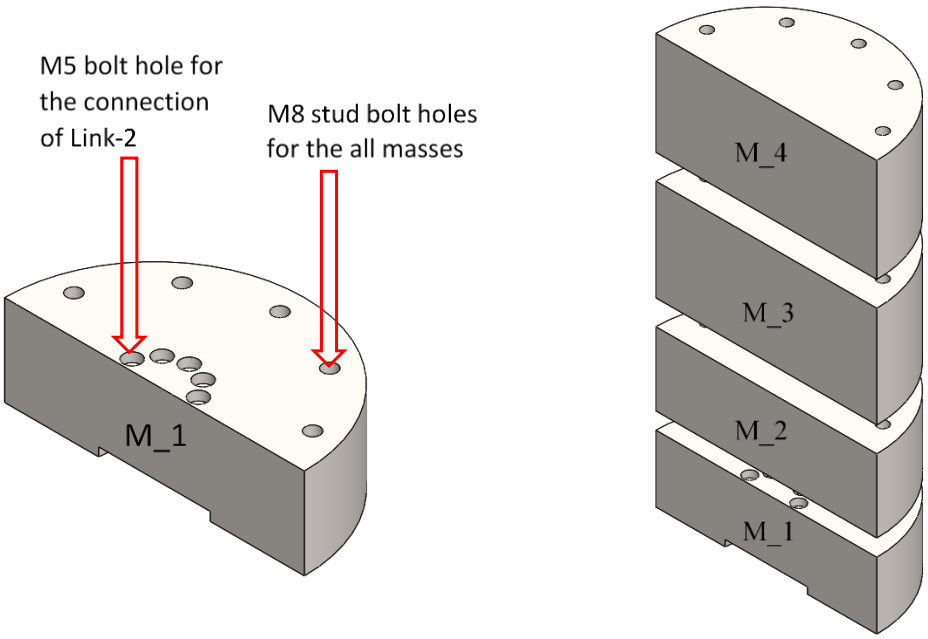

Figure 4.17. The balancing masses and connection details.

.

CHAPTER 5

PROTOTYPE OF THE MECHANISMS

In this Chapter, prototypes of over- and simply constrained mechanism are presented in detail. Components of the prototype are explained in two subsections. The purchased components which are actuators, gearboxes, laser cutting head are presented in Section 5.1. The manufactured parts are described in Section 5.2.

5.1. Purchased Components

The main purchased components are the laser cutting head, the motors and the cycloidal gear drives. Firstly, the motor and reducer selection are explained in the following subsection. Then the used laser cutting head and its properties are given.

5.1.1. Motor and Reducer Selection

According to CAD model of the mechanism, the parametric values are updated in order to obtain the torque values in the dynamic model (which is derived in Section 3.4). The dynamic model is run with a trajectory which gives the maximum torque values. The end-effector position (-50 mm, 272 mm) where the expected maximum torque value is obtained is shown in Figure 5.1. When the end effector is initiated from this point with maximum acceleration along a diagonal path, the maximum torque value is found as 138.33 N·m in the dynamic model. Other criteria expected from the motor are as follows:

- the need of motor torque should be low while working at high speeds
- the reducer should have no or minimal backlash in order to work under high dynamic conditions
- the motor and the reducer should have as low inertia as possible

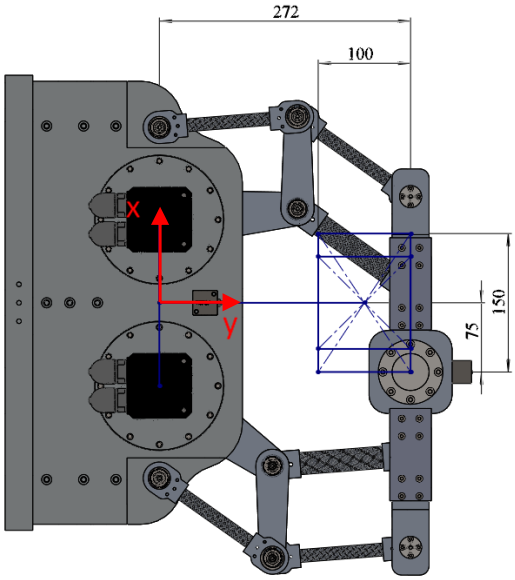

Figure 5.1. The point of workspace where the mechanism needs maximum actuator torque.

When all criteria are considered, Sumitomo Fine Cyclo F1C-A15 gearbox (Figure 5.2 (a)-(b)) and Kollmorgen AKM33E series motor (Figure 5.2 (c)) are selected and their properties are given in Table 5.1. The gearbox was selected as a cycloid type gearbox which has high efficiency and low backlash (< 1arcmin) compared to other types (planetary gearboxes and harmonic gearboxes) (The study of motor and reducer selections were realized within the scope of the TÜBİTAK project no:116M272).

Table 5.1. The selected motor and gearbox properties.

Motor	Gearbox	Output Torque (N·m)	Maximum Torque (N·m)	Average Speed (rpm)	Maximum Speed (rpm)	Rated Power (Watt)
AKM33E	F1C-A15 (1:59)	111	164	70	93	1100

5.1.2. The Laser Cutting End-Effector

The balancing masses are designed to reduce vibrations that affect the base. The positioning accuracy is expected to improve with reduced amount of vibrations. In order to measure positioning accuracy, it is sufficient to observe the difference between the given trajectory and the followed trajectory of the end-effector. The laser cutting head

was suitable for this process as the end-effector. The purchased laser cutting head and its components are shown in Figure 5.3 (a)-(c).

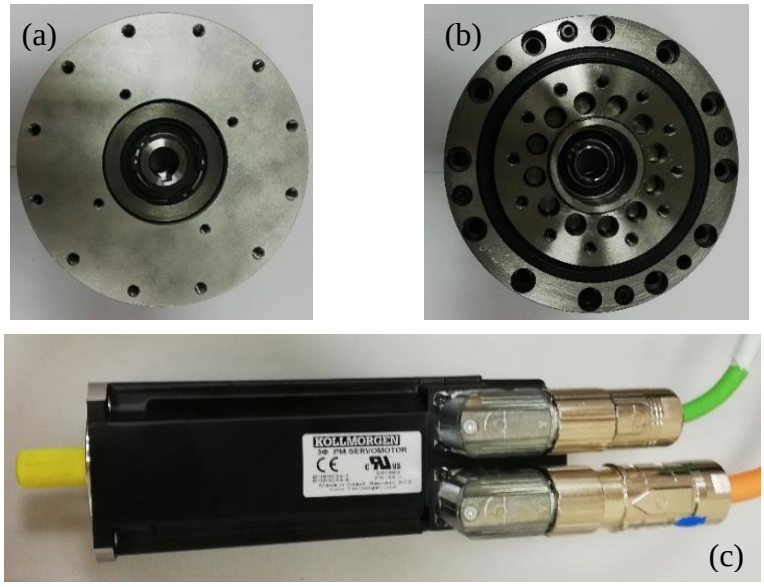

Figure 5.2. (a) The gearbox bottom view, (b) the gearbox top view, (c) AKM33E motor.

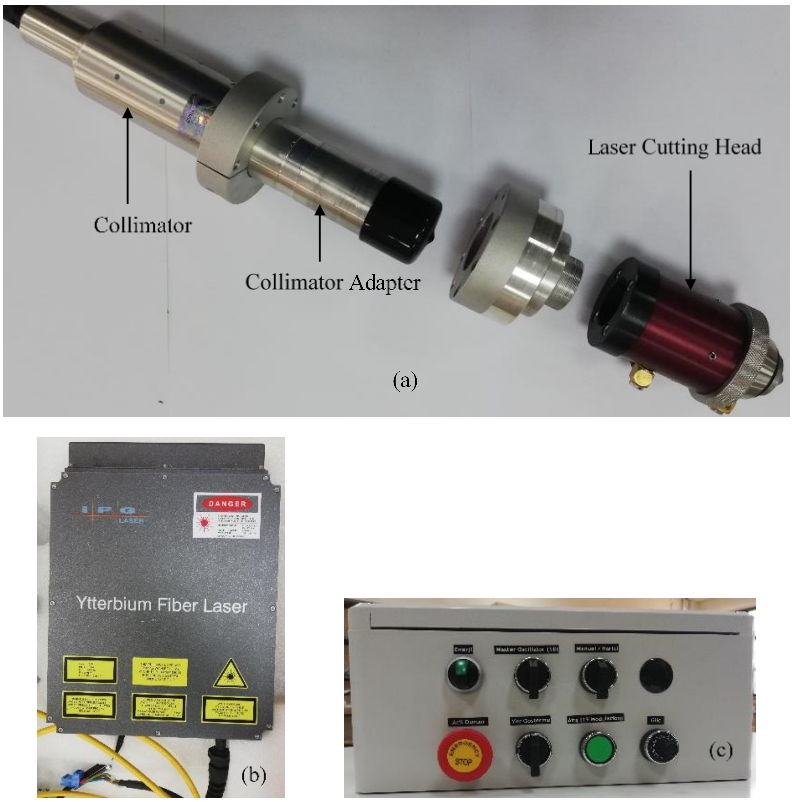

Figure 5.3. (a) PHF25 lacer cutting head (HAAS Technologies Inc.), (b) YLP-1-120-50-50 HC resonator (IPG Laser Inc.), (c) electrical panel.

5.2. Manufacturing of Components

It is aimed to come up with a simple design of the parts of the mechanism. All metal link parts are produced with a CNC milling machine and the shafts are produced with a lathe. One of the considered factors when producing parts is the parallelism and the desired distances between the joint axes of the links. Other factors are shaft and the hole tolerances of bearings and shafts. Link types 1 and 3 are explained in Appendix A with the study of preliminary prototype. The balancing masses are also presented in detail in the following subsection with updates according to the manufactured mechanism parts.

Firstly, the manufactured parts of support group are demonstrated. The steel table (Figure 5.4) which is available from a previous project weighs nearly 500 kg to prevent undesired motion of the mechanism. Therefore, support-1 was designed to match with the connection holes available on the table. The assembly of support parts is shown in Figure 5.4. There are two critical points for the base. One of them is to connect the shaft-1 to the base by press-fitting. Therefore, when for the machined holes for shaft-1, the tolerance value is given as +0.02 mm. The other critical point is the precision milling of the surface on which the gearbox is to be located. The mass of the support group is approximately 18 kg.

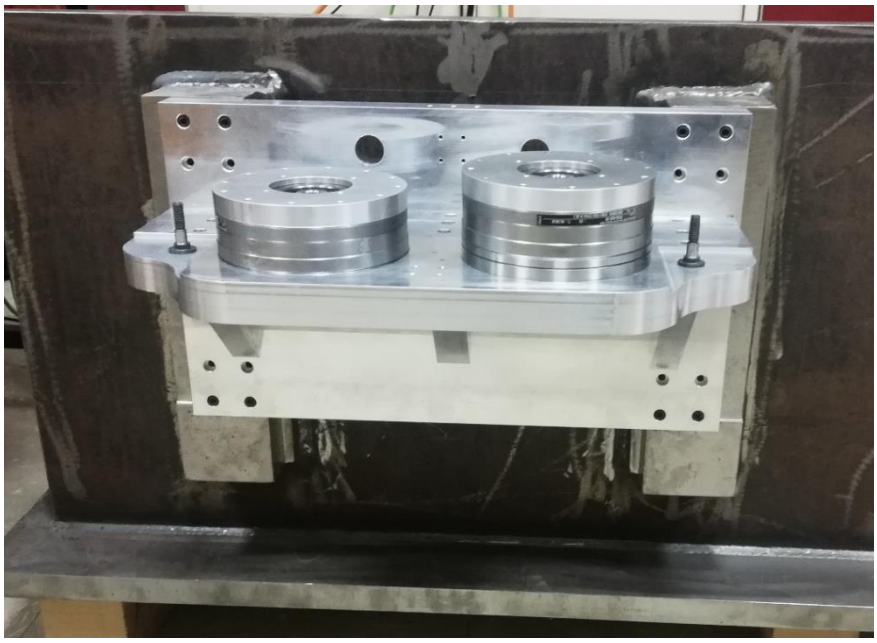

Figure 5.4. The support group, the reducers and the table.

Type 2 links are assembled to the gearbox (Figure 5.2 (b)). For this reason, as seen in Figure 5.5, the flange surface to be jointed with the gearbox is machined more precisely like the base. Heat treatment and grinding were applied to each of shafts in order to increase surface precision and strengthen the material structure. The shaft-2 (Figure 5.5) was seated by applying press-fitting pressure to the hole. The mass of link type 2 with shaft-2 is 928.6 g. Shaft-3 and the ball bearing are mounted in the holes of intermediate link (Figure 5.6). The mass of the intermediate link with shaft-3 and the ball bearing is 155.2 g.

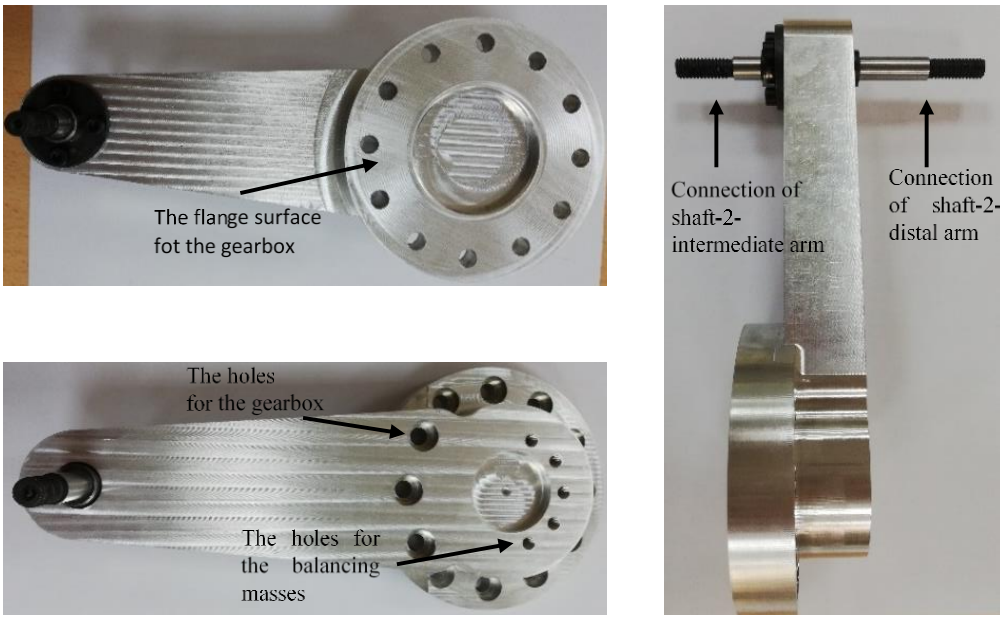

Figure 5.5. Three view of link type 2 and shaft-2.

Figure 5.6. The intermediate link and shaft-3.

The platform is shown with shaft-4 and shaft-5 in Figure 5.7 (a). The dummy end effector is shown in Figure 5.7 (b). The mass of the platform and the dummy end-effector are 1452.8 g and 1870 g, respectively. The important point is to make the mass of the

platform group 5 kg. For this reason, an additional mass of 1670 g is needed. As mentioned in Chapter 4, the extra masses designed after the production of the platform are produced according to the specified mass (Figure 5.7 (c)). The mass of the bolts and nuts to be used when determining the value of extra mass is taken into account and the extra masses are produced as 750 g each.

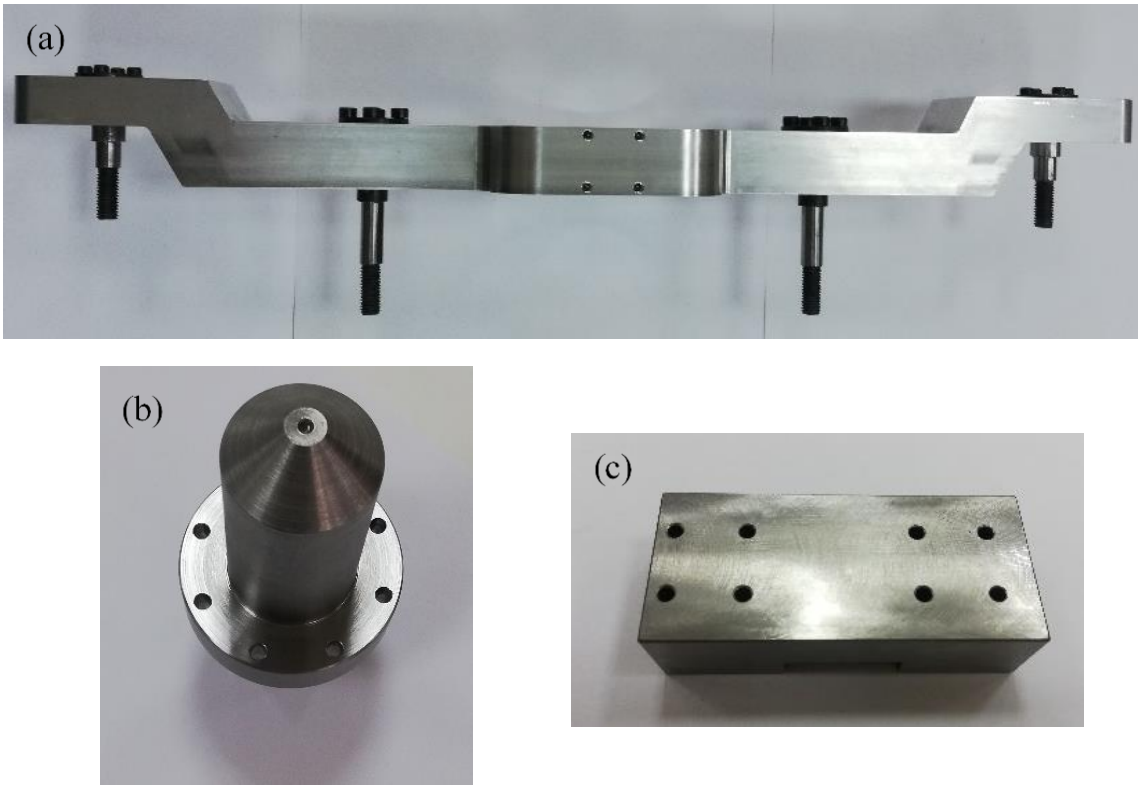

Figure 5.7. (a) The platform, (b) the dummy end-effector, (c) an extra mass.

As mentioned in Chapter 4, composite tubes were selected for all auxiliary arms and distal main arms to reduce the inertia of the mechanism. However, the use of composite tubes for mechanisms is not widespread. A preliminary prototype was made to obtain information about the use of composite tubes. In this way, bonding of metal parts with composite tubes has been tried. Moreover, a tensile test was conducted to see how the composite tube-metal combination reacted to higher tensile forces. These details are presented in Appendix A to explain why and how composite tubes are selected for the mechanism. As a result, the composite links of over- and simply constrained mechanisms are similarly produced and assembled with the mentioned method. Link types 1 and 3 are

shown in Figure 5.8 (a)-(b). The masses of link types 1 and 3 are measured as 123.6 g and 219.4 g, respectively.

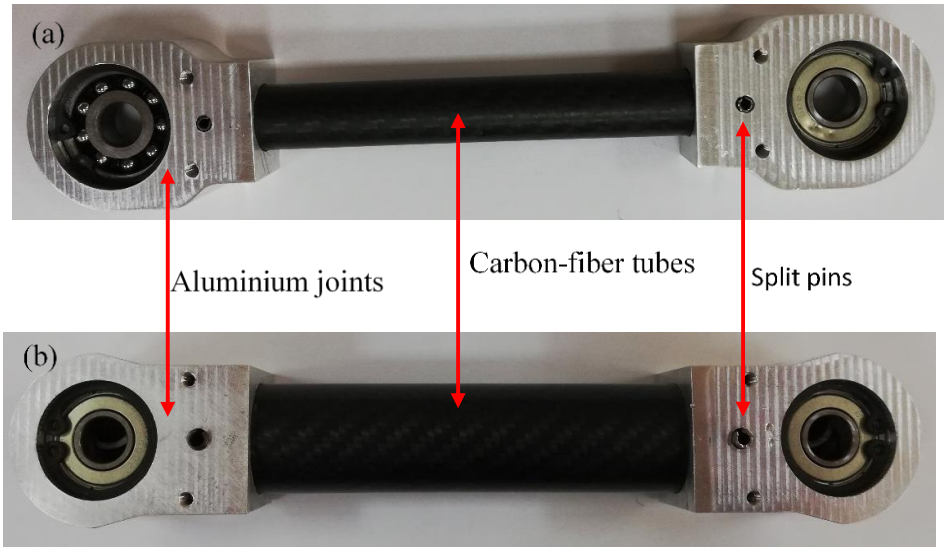

Figure 5.8. (a) The manufactured link type 1, (b) the manufactured link type 3.

As mentioned in Section 4.4, additional masses were designed for the simply constrained mechanisms to prevent the symmetric mass distribution. Before the manufacturing of additional masses, the mass of link type 3 were measured as 123.6 g. Thus, the height of additional masses was determined as 12.2 mm to obtain 61.8 g. The additional masses are shown with their mass values in the Figure 5.9.

Figure 5.9. The additional masses for the simply constrained mechanism.

5.2.1. Manufacturing of Balancing Masses

As mentioned in Section 4.4, the mass of the balancing masses is determined in order to obtain exact mass values of the mechanism after the production of all parts. The diameter of balancing masses and the connection holes are the same as in the CAD model. The force balancing equations in Section 3.3 are used to calculate the mass balancing values. The lumped masses and their location are shown in Figure 3.6 and given in Table 5.2. The total value of the balancing mass is found as 24.276 kg according to the distance of its center of mass.

Table 5.2. Mass and distance values of the masses.

Mass values (in kg)			Mass location (in mm)		
$m_1 = 1.05$	$m_2 = 0.59$	$m_{bm} = 24.28$	$p_1 = 59.43$	$p_2 = 18.7$	$p_{bm} = 37.6$

The balancing mass values determined for three different conditions (as mentioned in Section 4.4 are given in the Table 5.3. These conditions are: 1) when the end-effector of the mechanism is not assembled, 2) when the end-effector is assembled, 3) when the platform group total mass is 5kg.

Table 5.3. The balancing mass values for the conditions.

	Payload	Balancing mass values
Condition-1	1.45 kg	$M_1 + M_2 = 10.1$ kg
Condition-2	3.41 kg	$M_1 + M_2 + M_3 = 17.1$ kg
Condition-3	5 kg	$M_1 + M_2 + M_3 + M_4 = 24.28$ kg

The heights of the balancing masses were determined by taking into account the masses of bolts and nuts according to Table 5.3. The heights of M_1, M_2, M_3 and M_4 are found as 52 mm, 57 mm, 79 mm, 80.5 mm. The manufactured balancing masses are shown in Figure 5.10.

(a) (b)

Figure 5.10. The manufactured balancing masses: (a) M_1, (b) M_2.

The balancing masses (M_1, M_2, M_3, M_4) are produced two for each. The mass values of balancing masses after manufacturing are presented in Table 5.4. The mass values are shown with symbol "M_{ji}" for j=1, 2, 3, 4 and i=1, 2. These masses are collected in two groups which can be seen from the table. The total mass of each group is almost close to each other. However, the calculated mass is 24.28 kg as mentioned before. The difference between the calculated mass and the manufactured mass is completed with additional nuts and connection components (stud bolts).

Table 5.4. The mass values of balancing masses after the manufacturing process.

M_{11}	4.533 kg	M_{12}	4.531 kg
M_{21}	4.999 kg	M_{22}	4.978 kg
M_{31}	6.947 kg	M_{32}	6.947 kg
M_{41}	7.071 kg	M_{42}	7.073 kg
Total	23.52 kg	Total	23.53 kg

The assembled prototype of the over-constrained mechanism and the simply constrained mechanism are shown in Figure 5.11 and Figure 5.12, respectively. The over-constrained mechanism was made ready for testing and all systems were commissioned as the actuators, the drivers, the electrical panel.

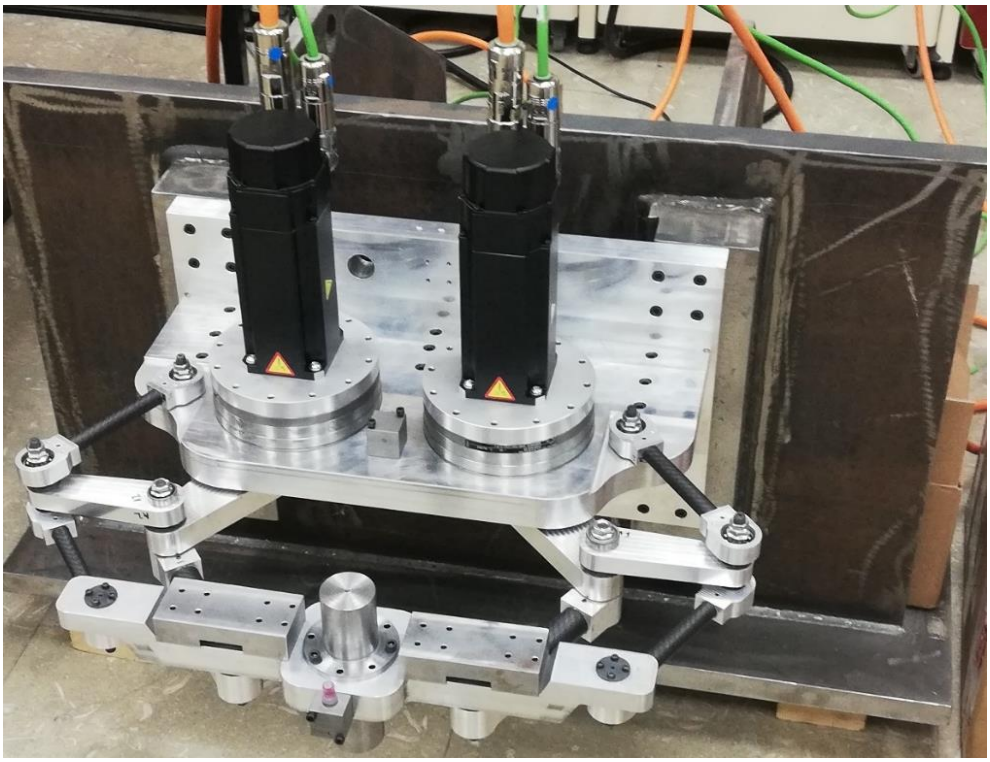

Figure 5.11. The prototype of over-constrained mechanism.

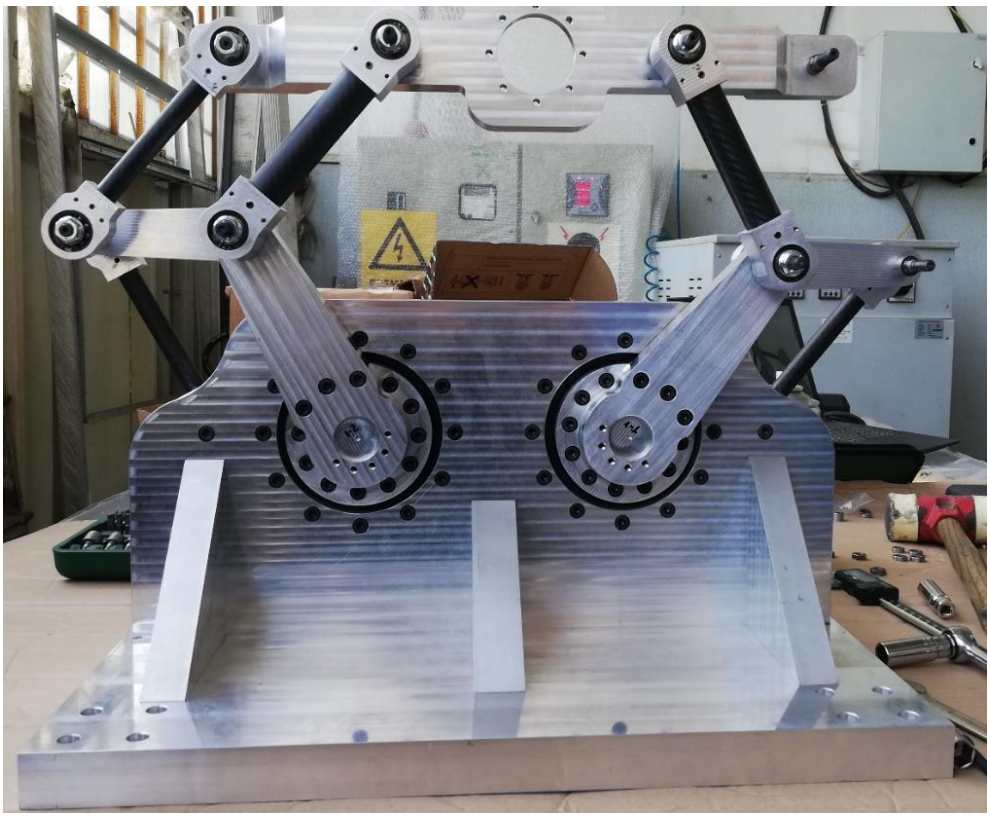

Figure 5.12. The prototype of simply constrained mechanism.

5.2.2. Dimensional Measurements of the Manufactured Parts

In this subsection, the dimensional measurements of manufactured parts are given to update kinematic parameters of the mechanism in the computer models. The kinematic dimensions of the mechanism are measured using Faro PrimeARM (1.2 m measurement arm) and Faro CAM2 Measurement 10.6 software program. Faro PrimeArm has 0.016 mm point repeatability and 0.023 mm volumetric accuracy (FaroARM, n.d.). The links for measurements were named as shown in Figure 5.13, where the first number were used for the same type of links. During the measurements, 3 mm probe was used with Faro PrimeArm (1.2 m). Before the measurements, the probe was calibrated and the error of probe was found as 0.0075 mm.

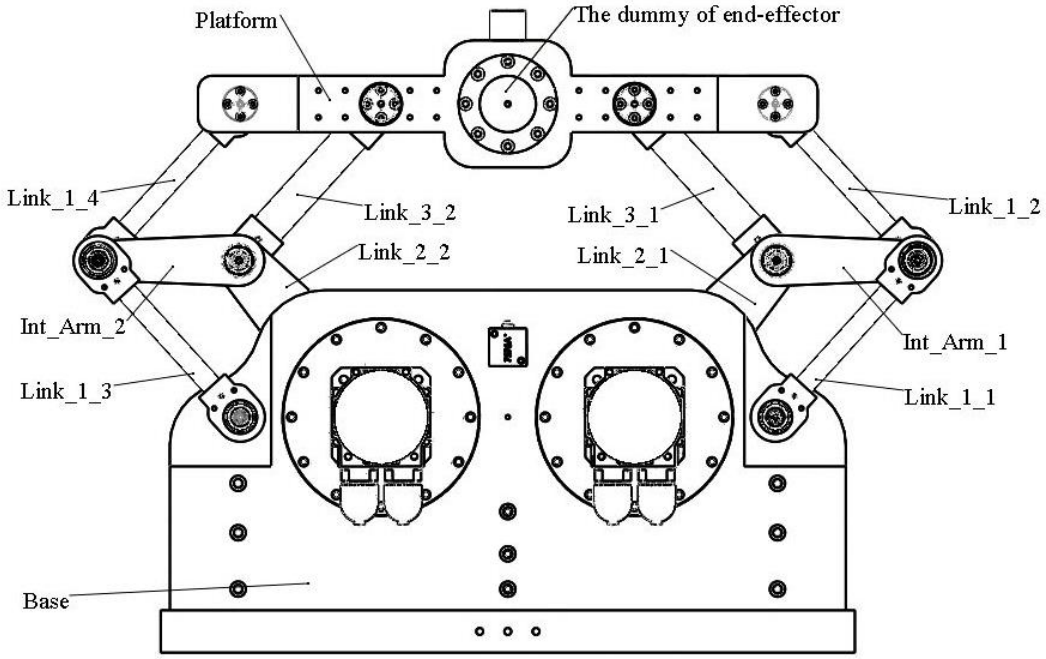

Figure 5.13. The name of links for dimensional measurements.

In order to measure the dimensions of the links, for details that would be expected to be precisely machined, surfaces on the links are selected in the Faro CAM2 environment as shown in Figure 5.14-17 for the base, the platform, link type 2 and intermediate arms respectively. Then, measurements are made on the manufactured links by using the probe. Thus, the CAD model uploaded into the Faro CAM2 and the actual model are compared with each other. The measurements between the surfaces are given

in Table 5.5-8 for the base, the platform, link type 2, intermediate arms, link type 1 and link type 3, respectively.

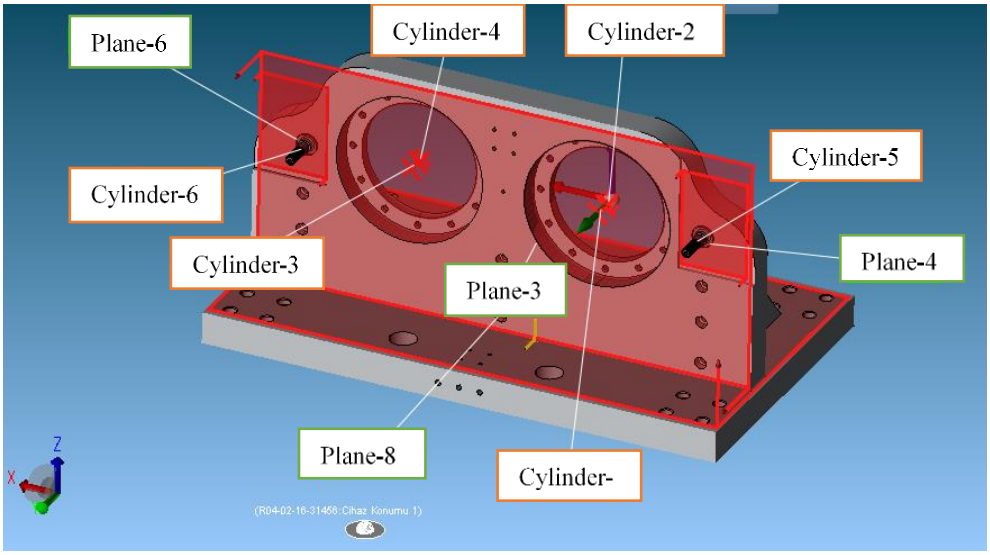

Figure 5.14. The surfaces on the base.

Table 5.5. The measurement results for the base.

Part Name	Surface-1	Surface-2	The measured distance value	The designed distance value
The base	Cylinder-4	Cylinder-6	100.064 mm	100 mm
The base	Cylinder-2	Cylinder-4	179.949 mm	180 mm
The base	Cylinder-5	Cylinder-2	99.939 mm	100 mm
The base	Cylinder-3	Cylinder-1	179.987 mm	180 mm

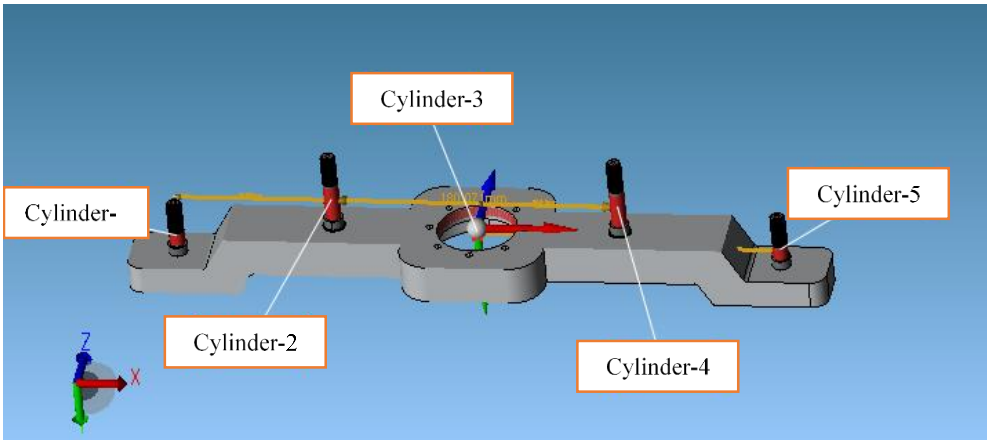

Figure 5.15. The surfaces on the platform.

Table 5.6. The measurement results for the platform.

Part Name	Surface-1	Surface-2	The measured distance value	The designed distance value
The platform	Cylinder-5	Cylinder-4	99.963 mm	100 mm
The platform	Cylinder-2	Cylinder-4	180.071 mm	180 mm
The platform	Cylinder-3	Cylinder-4	90.024 mm	90 mm
The platform	Cylinder-1	Cylinder-2	99.992 mm	100 mm

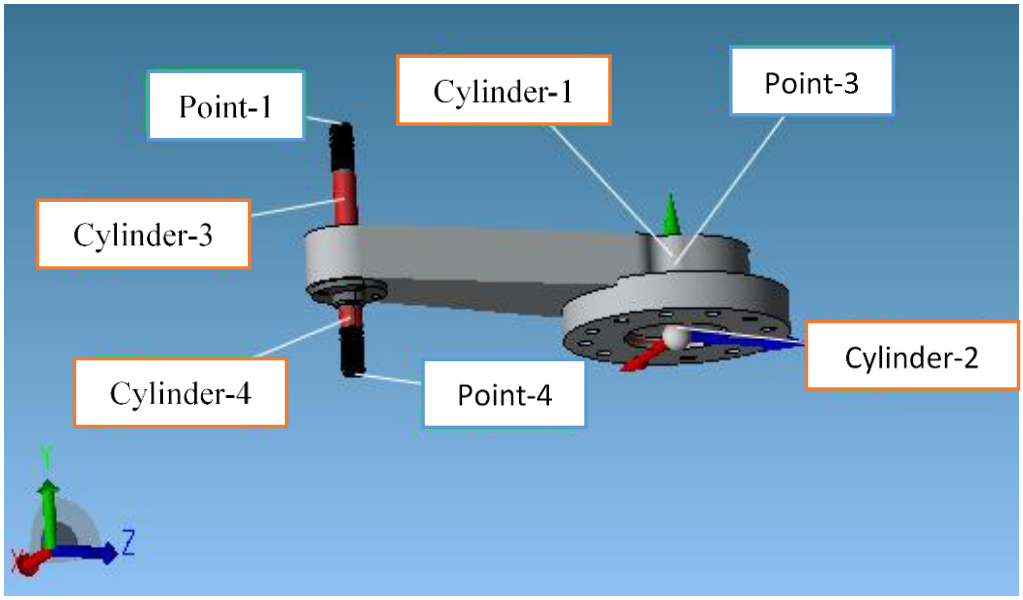

Figure 5.16. The surfaces on link type 2.

Table 5.7. The measurement results for link type 2.

Part Name	Surface-1	Surface-2	The measured distance value	The designed distance value
Link_2_1	Cylinder-1	Cylinder-3	150.032 mm	150 mm
Link_2_1	Cylinder-2	Cylinder-4	150.044 mm	150 mm
Link_2_2	Cylinder-1	Cylinder-3	150.006 mm	150 mm
Link_2_2	Cylinder-2	Cylinder-4	150.009 mm	150 mm

The kinematic dimensions of the mechanism were found to be close to the designed values as can be seen in Table 5.9. It can be stated that the dimension of manufactured parts is acceptable from the measurements in terms of values of production tolerances.

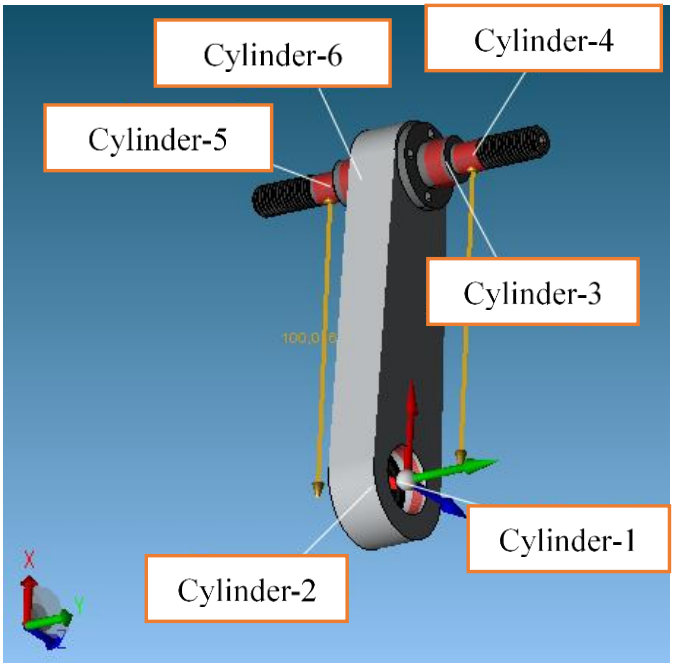

Figure 5.17. The surfaces on the intermediate arm.

Table 5.8. The measurement results for intermediate arm.

Part Name	Surface-1	Surface-2	The measured distance value	The designed distance value
Int_Arm_1	Cylinder-2	Cylinder-4	99.973 mm	100 mm
Int_Arm_1	Cylinder-2	Cylinder-6	100.016 mm	100 mm
Int_Arm_2	Cylinder-1	Cylinder-3	99.992 mm	100 mm
Int_Arm_2	Cylinder-1	Cylinder-4	99.965 mm	100 mm

Table 5.9. The measurement results for links type 1 and 3.

Part Name	The measured value (mm)	The designed value (mm)	Part Name	The measured value (mm)	The designed value (mm)
Link_1_1	150.045	150	Link_1_4	150.066	150
Link_1_1	150.014	150	Link_1_4	149.998	150
Link_1_2	150.063	150	Link_3_1	150.012	150
Link_1_2	150.018	150	Link_3_1	149.954	150
Link_1_3	150.059	150	Link_3_2	150.037	150
Link_1_3	150.055	150	Link_3_2	149.825	150

CHAPTER 6

TESTS

All the tests are performed for the over-constrained mechanism. Firstly, calibration procedure is clarified for the over-constrained mechanism. The measurements taken for calibration is evaluated according to VDI 3441 /DGQ Guideline (Statistical Testing of the Operational and Positional Accuracy of Machine Tools). The results of calibration are presented in Section 6.1. Balancing test procedure is explained in Section 6.2. Firstly, the unbalanced over-constrained mechanism is operated for a specific trajectory to measure the effect of vibrations on the base. Then, the balanced mechanism was operated for the same purpose. The acceleration measurements are made using tri-axial accelerometers. Finally, test results are stated and discussed.

6.1. Calibration

When the link length measurements of the mechanism prototype are investigated, the actual mechanism model is different from the theoretical mechanism model due to the manufacturing errors. The use of link lengths taken from the dimensional measurements is a way to modify the model. However, this is not a viable option for an over-constrained mechanism. Therefore, Kiper et al. (2015) applied two methods for the model estimation and calibration which makes use of the hidden robot concept. Based on end-effector position measurements, the hidden robot link lengths are determined using two methods: polynomial approximation and least square approximation. In order to apply these two methods, it is necessary to measure the inputs of the mechanism and the end-effector points. Thus, the model estimation problem becomes a path generation synthesis problem. Polynomial approximation method was found to yield better results compared to least square approximation to find optimum link lengths in the study (Kiper et al., 2015). Therefore, the polynomial approximation is used in this thesis.

It can be said that calibration of the mechanism consists of two stages. First, several measurements are taken for the end-effector position via a coordinate measurement machine are recorded and the input angle computed from inverse kinematics are computed. In this particular case, measurements are taken at 9 points: the corners, the midpoints of the sides and the geometric center of the rectangular workspace of the mechanism. Only two of these measurements can be used for polynomial approximation to determine the link lengths of the two dyads connecting the base and the end-effector point in the 5R hidden robot. So, all possible pairs of points out of 9 are tested for synthesis. For each pair of points synthesis is performed and the root-mean-square (RMS) error for the 9 points are computed based on the measured data. Finally, the pair of points which yield least amount of error are selected for determination of the link lengths.

Next, many measurements are taken within the workspace (in 5 mm increments in x- and y-directions within the 100 mm x 150 mm workspace) and based on the end-effector position measurements, the error between the desired input angles and the computed angles according to the inverse kinematics of the hidden robot model are computed. The hence-obtained error matrix is used along with bi-linear interpolation is used for the calibrated mechanism. The maximum errors are recorded and it is checked whether the error is within the accuracy aim which is set as 200 μm. Also the repeatability value for 100 μm is checked via repeated measurements according to the associated VDI standard. In this thesis, these stages are applied for the prototype of the over-constrained 6R mechanism (Figure 5.11). The applied two stages and their results are explained in detail in the following sections.

The calibration studies are applied to the condition where the mechanism works with the end-effector (the dummy of the laser cutting head). Ideally, the calibration studies should be repeated for the conditions under which the mechanism works (for specific payload and balancing mass values).

6.1.1. The First Stage: Model Estimation

In the first stage, end-effector locations $E(x_i, y_i)$ are measured at nine points which are four corners, four midpoints of the sides and the center of the mechanism's rectangular

workspace (100 mm x 150 mm) by using FARO PrimeArm. In addition, motor inputs (θ_{1i}, θ_{2i}) are calculated based on the E(x_i, y_i) measurements. Thus, the link lengths a_1, a_2, a_3, a_4 for hidden model (Figure 6.1) are calculated with given a set of inputs (θ_{1i}, θ_{2i}) and the end-effector locations E(x_i, y_i) for nine points. The polynomial approximation equations are explained for OAE dyad. θ_{2i} is used instead of θ_{1i} for OBE dyad and the rest of calculations is the same. The polynomial form is given in Equation 6.1 where X_i represents pair of precision point parameters (θ_{1i}, x_i, y_i) (i = 1,2) for OAE dyad, and (θ_{2i}, x_i, y_i) for OBE dyad.

$$\sum_{j=1}^{2} P_j f_j(X_i) = F(X_i) \tag{6.1}$$

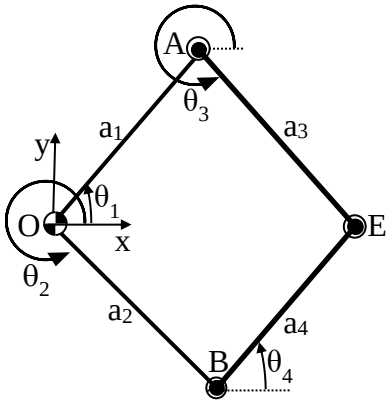

Figure 6.1. The hidden model of the over-constrained 6R mechanism.

Then I/O equation is expressed as follows:

$$\begin{aligned} &|OE|^2 = (x_i - a_2\cos\theta_{1i})^2 + (y_i - a_2\sin\theta_{1i})^2 = {a_3}^2 \\ &\Rightarrow ({a_3}^2 - {a_2}^2) + a_2 2(x_i\cos\theta_{1i} + y\sin\theta_{1i}) = ({x_i}^2 + {y_i}^2) \end{aligned} \tag{6.2}$$

When the polynomial form and I/O equation are matched, the terms are found as $P_1 = {a_3}^2 - {a_2}^2$, $P_2 = a_2$, $f_1(X_i) = 1$, $f_2(X_i) = 2(x_i\cos\theta_{1i} + y_i\sin\theta_{1i})$, $F(X_i) = {x_i}^2 + {y_i}^2$.

Thus, P_1 and P_2 are linearly solved for given two sets of (θ_{1i}, x_i, y_i) as given in Equation 6.3:

$$\begin{bmatrix} 1 & 2(x_1\cos\theta_{11} + y_1\sin\theta_{11}) \\ 1 & 2(x_2\cos\theta_{12} + y_2\sin\theta_{12}) \end{bmatrix} \begin{bmatrix} P_1 \\ P_2 \end{bmatrix} = \begin{bmatrix} {x_1}^2 + {y_1}^2 \\ {x_2}^2 + {y_2}^2 \end{bmatrix} \tag{6.3}$$

In order to decide the optimum link lengths, two of the 9 data (36 possibilities) are selected which will give the least RMS error values. The measured data are given in Table 6.1. The design points 1 and 3 give the minimum RMS error. The kinematic parameters are found as a_1 = 149.969 mm, a_2=149.751 mm, a_3 = 150.007 mm and a_4 = 150.094 mm. With these link lengths, the RMS error for the 9 points is computed as 145 μm.

Table 6.1. Measured data for polynomial approximation.

j	Desired		Measured		θ_1 (°)	θ_2 (°)
	x_j	y_j	x_j	y_j		
1	222.132	0	222.182	0.049	42.231	-42.231
2	272.132	75	272.098	74.774	35.201	-4.384
3	272.132	0	272.088	-0.064	24.891	-24.891
4	272.132	-75	272.092	-74.762	364.384	324.799
5	222.132	-75	222.208	-74.878	379.945	302.742
6	172.132	-75	172.398	-74.928	387.710	285.203
7	172.132	0	172.271	0.094	54.986	-54.986
8	172.132	75	172.298	74.986	74.797	-27.710
9	222.132	75	222.204	74.974	57.258	-19.945

The maximum error is measured for point 7, for which the error for x-direction is 171 μm, for y-direction is 99 μm and the absolute error is 198 μm, which is slightly lower than the target value of 200 μm. This error value is further decreased via the calibration studies explained in the next section. The maximum errors for the uncalibrated version were recorded at point 6, where the error for x-direction is 94 μm, for y-direction is 266 μm and the absolute error is 282 μm.

6.1.2. The Second Stage: Workspace Calibration

The procedure for obtaining the error matrices and integrating into the control system is described below:

1) The 100 mm x 150 mm workspace of the mechanism is divided at equal intervals of 5 mm x 5 mm (Figure 6.2). Thus, 651 points are specified to measure. Faro PrimeArm is used to take measurements at the end-effector points.

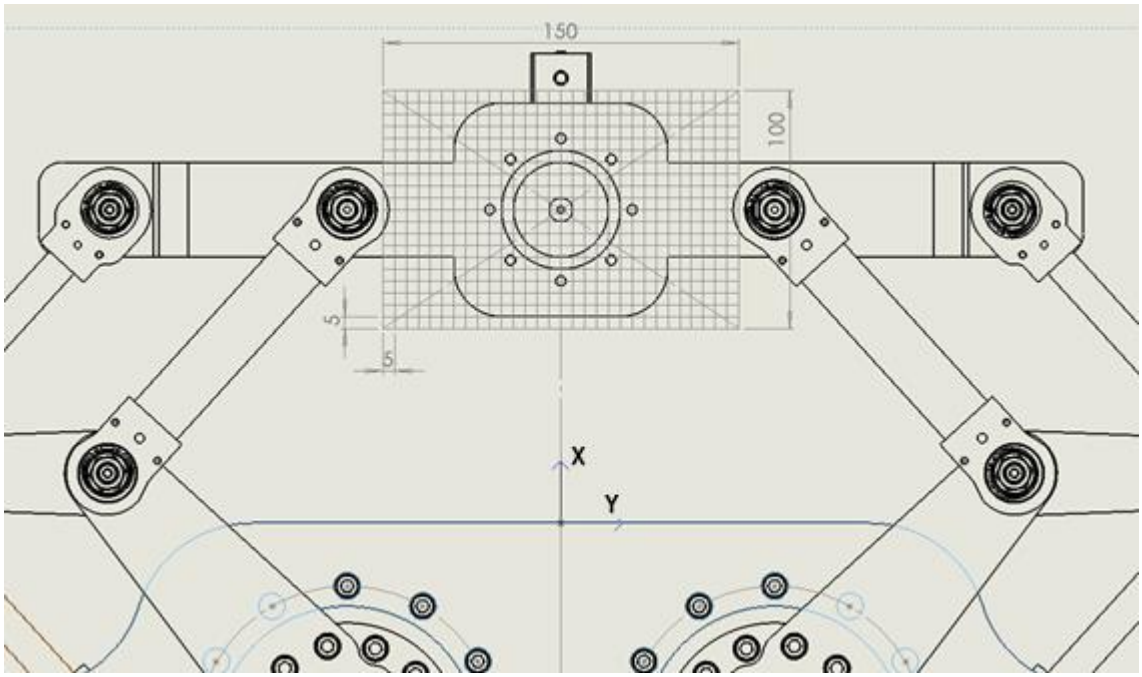

Figure 6.2. The workspace of the mechanism with 5 mm x 5 mm grids for calibration studies.

2) The difference between desired value and measured value of points is calculated to create error matrices $[\delta_{xi}]_{21x31}$ and $[\delta_{yi}]_{21x31}$ for x- and y-axes of the mechanism.
3) Using bilinear interpolation the error value for any point on the workspace of the mechanism except these 651 points are found. All grids have four corner points which are shown in Figure 6.3 as $Q_{11}(x_1, y_1)$, $Q_{12}(x_1, y_2)$, $Q_{21}(x_2, y_1)$, $Q_{22}(x_2, y_2)$ and the errors are $\delta_{11}(x_1, y_1)$, $\delta_{12}(x_1, y_2)$, $\delta_{21}(x_2, y_1)$, $\delta_{22}(x_2, y_2)$ at these points. The position error $\delta(x, y)$ at a point $P(x, y)$ is calculated with four

corner points by using bilinear interpolation as shown in Equation 6.4. The position error is calculated by using linear interpolation where x is equal to x_1 or y is equal to y_1 as shown in Equation 6.5. These calculations are carried out separately for x- and y-axes.

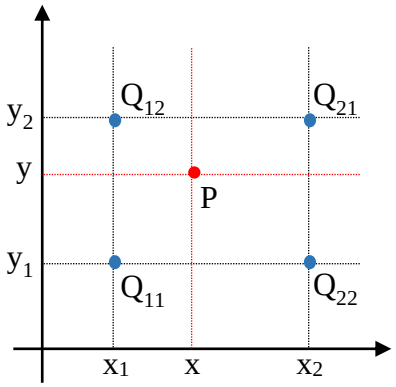

Figure 6.3. The four corner points of grid for bilinear interpolation.

$$\delta(x,y)=\frac{\left\{\begin{array}{l}(x_2-x)(y_2-y)\delta_{11}+(x_2-x)(y-y_1)\delta_{12}\\+(x-x_1)(y_2-y)\delta_{21}+(x-x_1)(y-y_1)\delta_{22}\end{array}\right\}}{(x_2-x_1)(y_2-y_1)} \tag{6.4}$$

$$\begin{aligned} x=x_1 \Rightarrow \delta(x,y)&=\frac{(y_2-y)\delta_{11}+(y-y_1)\delta_{12}}{y_2-y_1}\\ y=y_1 \Rightarrow \delta(x,y)&=\frac{(x_2-x)\delta_{11}+(x-x_1)\delta_{21}}{x_2-x_1}\end{aligned} \tag{6.5}$$

4) When the position error (δx, δy) is known, the errors of input value ($\delta\theta_1$, $\delta\theta_2$) are found by using the inverse kinematics Jacobian matrix as shown in Equation 6.6.

$$\delta_{\theta 1}=-\frac{c\theta_3\delta_x+s\theta_3\delta_y}{a_1 s(\theta_1-\theta_3)}\ ,\ \delta_{\theta 2}=-\frac{c\theta_4\delta_x+s\theta_4\delta_y}{a_2 s(\theta_2-\theta_4)} \tag{6.6}$$

5) The motor inputs (θ_1, θ_2) are modified as θ_{1_new}, θ_{2_new}. When the mechanism is moved, the control system is fed with these new motor inputs.

$$\theta_{1\_new}=\theta_1-\delta\theta_1,\ \theta_{2\_new}=\theta_2-\delta\theta_2 \tag{6.7}$$

After five steps, the results of calibration studies are evaluated in terms of positional deviation, standard deviation, repeatability according to VDI 3441 /DGQ (Statistical Testing of the Operational and Positional Accuracy of Machine Tools) guideline. In this guideline, all calculations are separately performed for each axis of the mechanism workspace. In the guideline, 10 random points are recommended for 1 m line of an axis, but since the workspace of the manipulator is small, 10 random points are selected for 100 mm x-axis of the mechanism and 15 random points are selected for 150 mm y-axis of the mechanism.

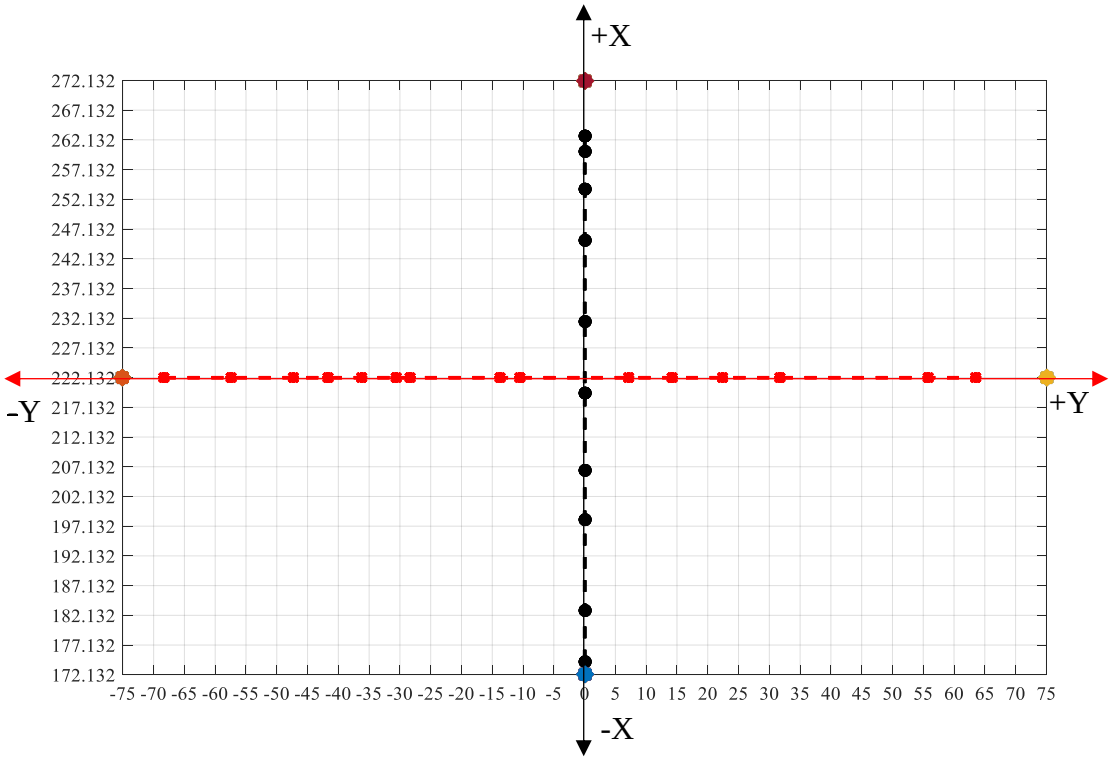

Figure 6.4. Random points on the workspace of the mechanism.

10 random points on the x-axis with black points and 15 random points on the y-axis with red points are demonstrated in Figure 6.4. These random points are measured in positive and negative directions and the measurement are repeated five times. The mean values for the repeated measurements are given in the following tables and figures in this section. The midpoints of the rectangular workspace are also showed in Figure 6.4. They are used as reference points to measure same points two times (positive and negative direction). The measurement steps are applied to the mechanism firstly without the modified kinematic parameters and before calibration steps, secondly with the modified

kinematic parameters and after calibration steps. Thus, the mechanism can be compared as calibrated and non-calibrated.

The "+X" representation means that the end-effector location is measured in a positive direction along the x-axis, while the "-X" representation indicates the negative direction. The same representations are also used for the y-axis. As seen in Tables 6.2-3 and Figure 6.5, the errors have drastically reduced for the calibrated mechanism for x-axis. The deviation from desired point coordinate is the difference between the desired point coordinate and the mean of five measurements taken at this point. The results for non-calibrated and calibrated mechanism are compared according to the calculated maximum deviation to indicate the improvement of positioning accuracy. The maximum deviation from desired point coordinate is calculated as 180 μm at point-1 in the positive direction for the non-calibrated mechanism, whereas it is calculated as 75.8 μm at point-8 in the negative direction for the calibrated mechanism.

Table 6.2. The results of x-axis for the non-calibrated mechanism.

	Desired Point (mm)	Deviation from desired point (μm)		Standard deviation (μm)		Repeatability (μm)	
		+X	-X	+X	-X	+X	-X
1	174.382	180.00	179.60	2.92	3.58	8.75	10.73
2	182.912	115.60	169.20	2.70	3.11	8.11	9.34
3	198.202	81.80	137.40	2.77	3.05	8.32	9.15
4	206.522	79.40	132.40	2.88	3.51	8.64	10.52
5	219.542	59.20	108.60	1.10	3.21	3.29	9.63
6	231.572	42.60	86.00	2.70	3.54	8.11	10.61
7	245.152	19.00	53.60	3.39	3.21	10.17	9.63
8	253.912	10.00	48.80	2.12	3.63	6.36	10.90
9	260.102	17.40	17.00	2.88	4.58	8.64	13.75
10	262.762	19.00	15.20	2.35	4.09	7.04	12.26

In the positive direction of the travel, the deviation calculated for the calibrated mechanism is greater than the one for the non-calibrated mechanism at points-7 and -8 as can be seen in Figure 6.5. In the negative direction of the travel, the deviation calculated for the calibrated mechanism is greater than the one for the non-calibrated mechanism at

points -7, -8, -9 and -10. Nevertheless, the calibrated mechanism performs better in overall.

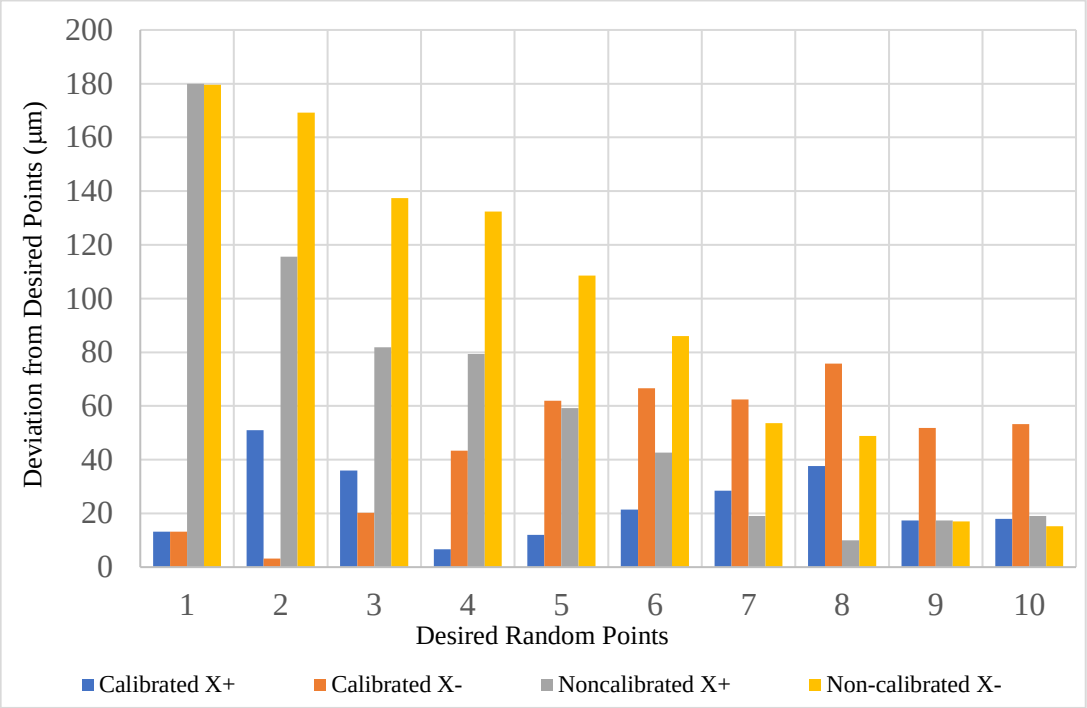

Figure 6.5. The deviation between the measured and desired points for x-axis.

Table 6.3. The results of x-axis for the calibrated mechanism.

	Desired Point (mm)	Deviation from desired point (µm)		Standard deviation (µm)		Repeatability (µm)	
		+X	-X	+X	-X	+X	-X
1	174.382	13.20	13.20	2.77	4.09	8.32	12.26
2	182.912	51.00	3.20	2.55	4.76	7.65	14.29
3	198.202	36.00	20.20	3.39	4.32	10.17	12.97
4	206.522	6.60	43.40	3.65	3.65	10.94	10.94
5	219.542	12.00	62.00	4.69	3.39	14.07	10.17
6	231.572	21.40	66.60	5.41	3.78	16.24	11.34
7	245.152	28.40	62.40	4.04	4.51	12.11	13.52
8	253.912	37.60	75.80	3.91	4.66	11.73	13.97
9	260.102	17.40	51.80	3.91	4.44	11.73	13.32
10	262.762	18.00	53.20	4.18	4.44	12.55	13.32

The results for the y-axis are presented in Tables 6.4-5 and Figure 6.6 for the calibrated and non-calibrated mechanism. The deviation from desired point is calculated as 116.8 μm at point-1 in the positive direction for the non-calibrated mechanism, whereas it is calculated as 72 μm at point-12 in the negative direction for the calibrated mechanism.

Table 6.4. The results of y-axis for the non-calibrated mechanism.

	Desired Point (mm)	Deviation from desired point (μm)		Standard deviation (μm)		Repeatability (μm)	
		+Y	-Y	+Y	-Y	+Y	-Y
1	-68.33	116.80	115.40	3.56	2.07	10.69	6.22
2	-57.39	51.80	112.20	2.49	2.17	7.47	6.50
3	-47.28	45.00	109.60	2.55	1.82	7.65	5.45
4	-41.74	36.60	103.60	2.70	3.21	8.11	9.63
5	-36.29	34.60	93.40	2.61	3.51	7.82	10.52
6	-30.67	44.80	102.40	1.64	3.44	4.93	10.31
7	-28.33	41.00	101.00	1.41	1.22	4.24	3.67
8	-13.69	22.80	76.60	2.68	3.21	8.05	9.63
9	-10.47	25.20	76.60	1.64	3.36	4.93	10.08
10	7.17	17.80	74.40	2.95	4.16	8.85	12.48
11	14.23	21.40	76.80	3.13	3.49	9.39	10.48
12	22.43	19.60	76.80	2.30	3.27	6.91	9.81
13	31.68	9.80	63.20	3.42	2.95	10.26	8.85
14	55.73	20.20	35.60	3.56	3.85	10.69	11.54
15	63.51	27.00	24.40	3.00	4.39	9.00	13.18

In the positive direction of the travel, the deviation is calculated for the calibrated mechanism more than the non-calibrated mechanism at point-10, -11 and -13 as can be seen in Figure 6.6. In the negative direction of the travel, the deviation is calculated for the calibrated mechanism more than the non-calibrated mechanism at point-14 and -15. In general, the calibration process improves the positioning accuracy for the y-axis of the mechanism except the mentioned points.

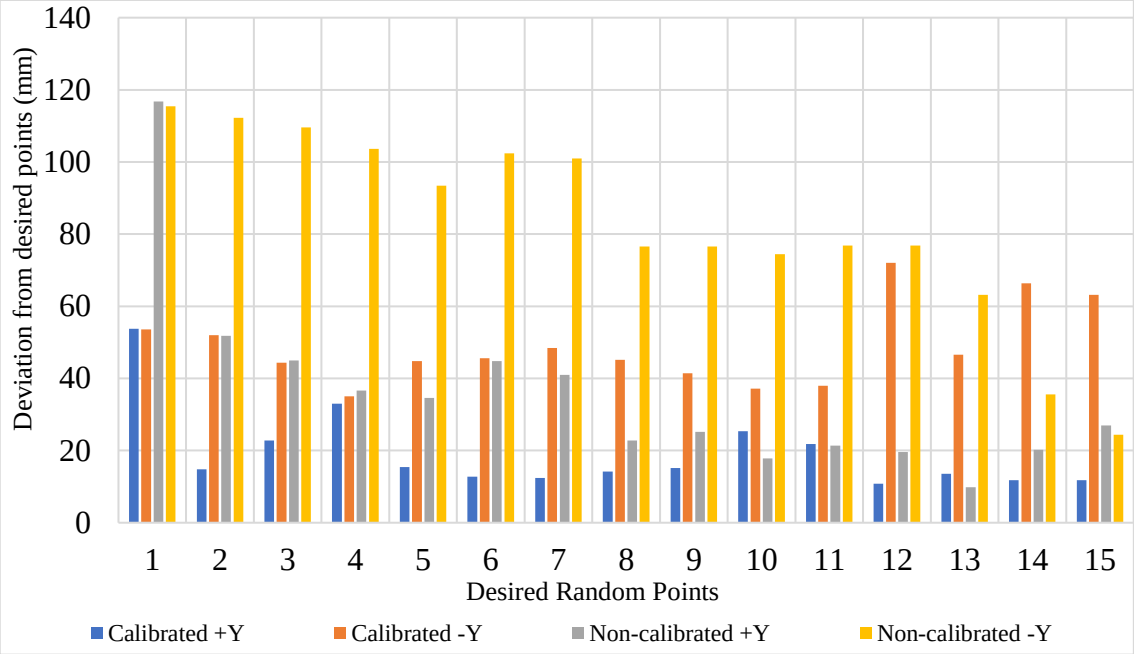

Figure 6.6. The deviation between the measured and desired points for y-axis.

Table 6.5. The results of y-axis for the calibrated mechanism.

	Desired Point (mm)	Deviation from desired point (µm)		Standard deviation (µm)		Repeatability (µm)	
		+Y	-Y	+Y	-Y	+Y	-Y
1	-68.33	53.80	53.60	2.17	2.41	6.50	7.22
2	-57.39	14.80	52.00	2.39	10.02	7.16	30.07
3	-47.28	22.80	44.40	2.59	4.51	7.77	13.52
4	-41.74	33.00	35.00	2.92	5.43	8.75	16.29
5	-36.29	15.40	44.80	4.77	5.45	14.32	16.35
6	-30.67	12.80	45.60	5.81	4.04	17.42	12.11
7	-28.33	12.40	48.40	7.16	3.65	21.49	10.94
8	-13.69	14.20	45.20	7.98	4.49	23.94	13.48
9	-10.47	15.20	41.40	8.32	2.30	24.96	6.91
10	7.17	25.40	37.20	8.65	3.27	25.95	9.81
11	14.23	21.80	38.00	6.42	3.00	19.26	9.00
12	22.43	10.80	72.00	4.71	1.73	14.14	5.20
13	31.68	13.60	46.60	7.20	1.52	21.59	4.55
14	55.73	11.80	66.40	3.83	2.70	11.50	8.11
15	63.51	11.80	63.20	4.82	4.09	14.45	12.26

When the measurements are evaluated, the calculated maximum precision is 9 μm for the non-calibrated mechanism and 11 μm for the calibrated mechanism on the x-axis. The calculated maximum precision is 20 μm for the non-calibrated mechanism, 15 μm for the calibrated mechanism on the y-axis. Although maximum standard deviation and maximum repeatability calculated based on the precision values increase for the calibrated mechanism as can be seen from the Tables 6.2-6.5, all taken measurements are evaluated according to VDI guideline for all points where positional uncertainty is enhanced as explained below.

Positional uncertainty (P) is the total deviation on the selected test axis taking into account the characteristic values determined in the individual positions: positional deviation (P_a), positional scatter (P_{sj}), reversal error (U). Therefore, it is necessary to describe these terms and to give explanation about their calculations.

P_a: the maximum difference of the mean values of all measuring positions on a selected test axis.

$$\bar{\bar{x}}_j = \frac{\bar{x}_j \uparrow + \bar{x}_j \downarrow}{2}, P_a = \left| \bar{\bar{x}}_{j\,max} - \bar{\bar{x}}_{j\,min} \right| \tag{6.8}$$

P_{sj}: it represents the effect of random deviations in each position on the chosen axis.

$$s_j \uparrow = \sqrt{\frac{\sum_{i=1}^{n} \left(x_{ij} \uparrow - \bar{x}_{ij} \uparrow \right)^2}{n-1}}, s_j \downarrow = \sqrt{\frac{\sum_{i=1}^{n} \left(x_{ij} \downarrow - \bar{x}_{ij} \downarrow \right)^2}{n-1}} \tag{6.9}$$

$$\bar{s}_j = \frac{\bar{s}_j \uparrow + \bar{s}_j \downarrow}{2}, P_{sj} = 6\bar{s}_j \tag{6.10}$$

U_j: the difference obtained from the mean values in both directions of travel for each position on the chosen test axis.

$$U_j = \left| \bar{x}_j \uparrow - \bar{x}_j \downarrow \right| \tag{6.11}$$

Thus, positional uncertainty can be calculated as follows:

$$P = \left[\bar{\bar{x}}_j + \frac{1}{2}\left(U_j + P_{sj} \right) \right]_{max} - \left[\bar{\bar{x}}_j - \frac{1}{2}\left(U_j + P_{sj} \right) \right]_{min} \tag{6.12}$$

where n is the number of measurements, $\overline{x_j}\uparrow$ and $\overline{x_j}\downarrow$ are the mean of the individual measured values at position x_j in the positive and negative direction, respectively. The computed results are summarized in Table 6.6. As seen in the table, the positional deviation (P_a) values have decreased from 181 μm to 81 μm in x-direction and from 117 mm to 53 mm in y-direction. Positional uncertainty formulation comprises of the mean of five measurements for each point and both directions, reversal error and positional scatter. Therefore, positional uncertainty shows the relation between all taken measurements. The positional uncertainty is decreased from 218 μm to 151 μm for x-axis, from 163 μm to 127 μm. Although the maximum repeatability values are higher for the calibrated mechanism, the repeatability values for each point and both axis were already calculated below the target value. In addition, it can be said that the repeatability of the mechanism is enhanced by looking at the decrease in the positional uncertainty.

Table 6.6. The results according to VDI guideline.

	Non-calibrated x-axis	Calibrated x-axis	Non-calibrated y-axis	Calibrated y-axis
P_a (μm)	181	81	117	53
$\overline{P_S}$ (μm)	18	24	19	28
$(P_s)_{max}$ (μm)	22	28	48	37
P (μm)	218	151	163	127

The calibration process was also implemented for the balanced over-constrained mechanism with the same modified kinematic parameters and error matrices. However, the obtained results show that the calibration process should be repeated for the balanced over-constrained mechanism. After that, it is necessary to compare the calibrated balanced mechanism with the non-calibrated balanced mechanism.

6.2. Balancing Tests

After the calibration study, the balancing tests are performed to observe vibrations on the base and the platform with accelerometers. Two types of accelerometers are used to measure acceleration values on the base and the platform. One of accelerometers is

DYTRAN 7556A2 which is attached on the platform via two screws. The other one is DYRTAN 7576A1 which is attached on the base via two screws. The attachment locations are depicted in Figure 4.5 (a) designated with “4” for the base and Figure 4.13 (a) designated with “4” for the platform. The properties of accelerometers are presented in Table 6.7. Thus, while acceleration data is received on x-, y- and z- axis for the base, the acceleration values that the end-effector should reach can be controlled from the accelerometer on the platform.

Table 6.7. Properties of accelerometers.

	DYTRAN 7556A2	**DYTRAN 7576A1**
Range of acceleration	±6 g triaxial	±5 g triaxial
Sensitivity of acceleration	200 (±10%) mV/g	500 mV/g
Range of angular velocity	±1000 °/sec	50 °/sec
Sensitivity of angular velocity	1.0 (±10%) mV/°/sec	25
Acceleration input frequency range	0-800 Hz	0-1150 Hz
Gyro input frequency range	0-150 Hz	0-1000 Hz

Test setup of the mechanism is shown in Figure 6.7. The motors are actuated with AKD Kollmorgen servo drives. Low-level control is performed with Cascade PID type controller which are embedded in the drivers. High-level control is realized by a computer based controller (NI PXI Chassis Modules). Accelerometers are directly connected to the computer based controller.

The requirement of motor power increases when the balancing masses are added. Therefore, the balancing masses are designed gradually as mentioned in Section 4.5. This makes it possible to conduct several combinations of balancing tests with different balancing mass values except for the conditions mentioned in Table 5.3. The mechanism is run with different acceleration values for three conditions. A trajectory is specified and it is used for all balancing test to compare each other. The test steps are explained for all conditions as follows:

1) A trajectory is specified.

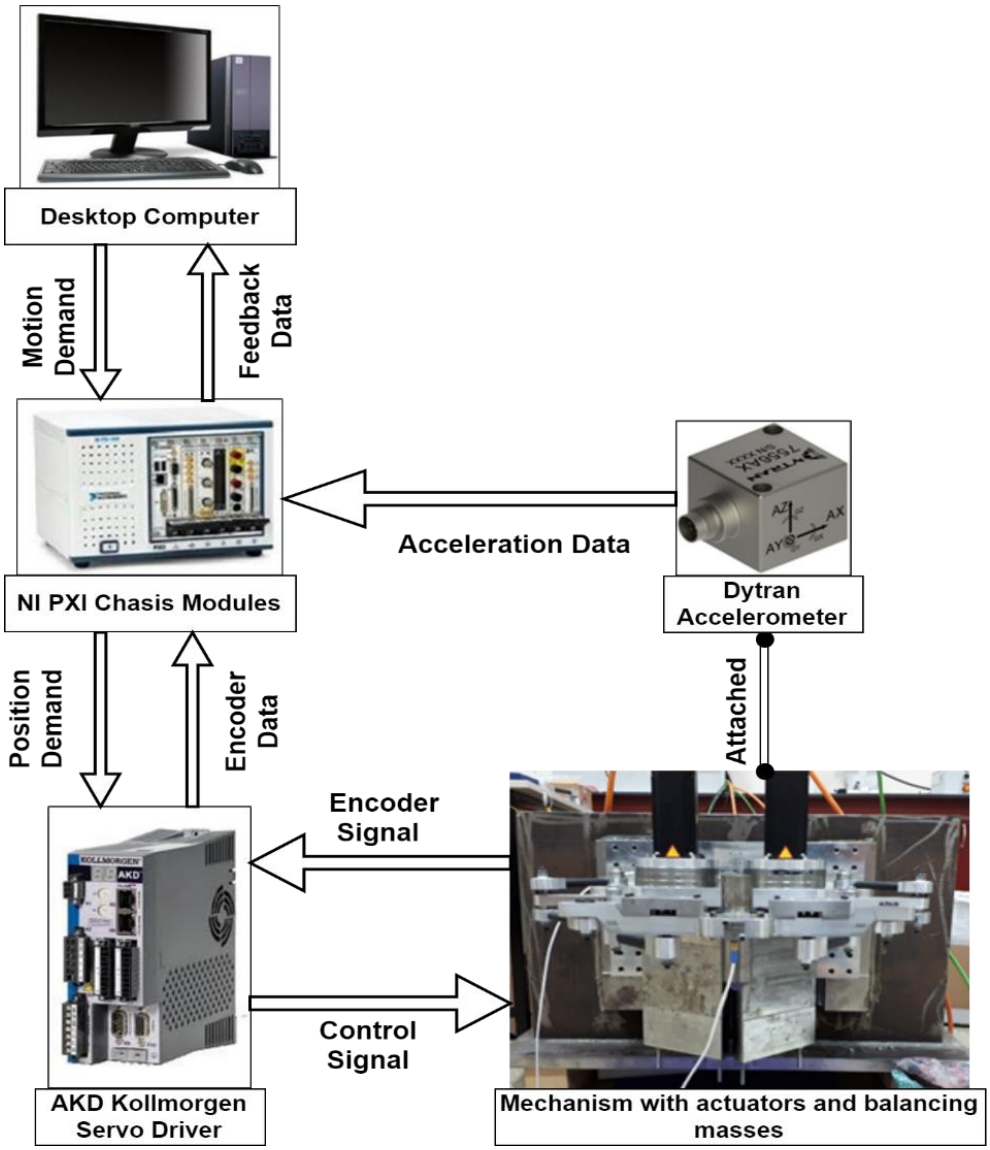

Figure 6.7. Test setup of the mechanism for balancing tests.

2) The motion and the acceleration that the mechanism should reach are checked on the control system.

3) The motion information is given to the actual system as position inputs of motors.

4) The data is recorded from the accelerometers, motor encoders and drivers (for measuring current values).

These steps are repeated for the unbalanced mechanism and the balanced mechanism at different target acceleration values. The maximum acceleration value is limited by the torque limit value of actuators for each condition. The trajectory consists

of longitudinal motions (on the x-axis of the mechanism) and lateral motions (on the y-axis of the mechanism) to observe the vibrations on each axis. The longitudinal motion is shown in Figure 6.8 and the lateral motion is shown in Figure 6.9. Of course, for different acceleration values these trajectories vary slightly in shape and considerably in time (the more the acceleration, the shorter the time). This type of trajectories is used for all balancing tests. The applied conditions and the acceleration values at which these conditions are tested are presented in Table 6.8.

Table 6.8. The conditions for the balancing tests.

Condition	Payload	Balancing Mass	Acceleration (g: 9.81 m/s^2)
1	just the platform (1.45 kg)	10.1 kg	1 g, 2g, 3 g, 4 g
2	platform + end-effector (3.41 kg)	17.1 kg	0.5 g, 1 g, 2 g, 3 g, 3.5 g
3	platform + end-effector + extra masses (5 kg)	24.28 kg	0.5g, 1g, 2g, 3g

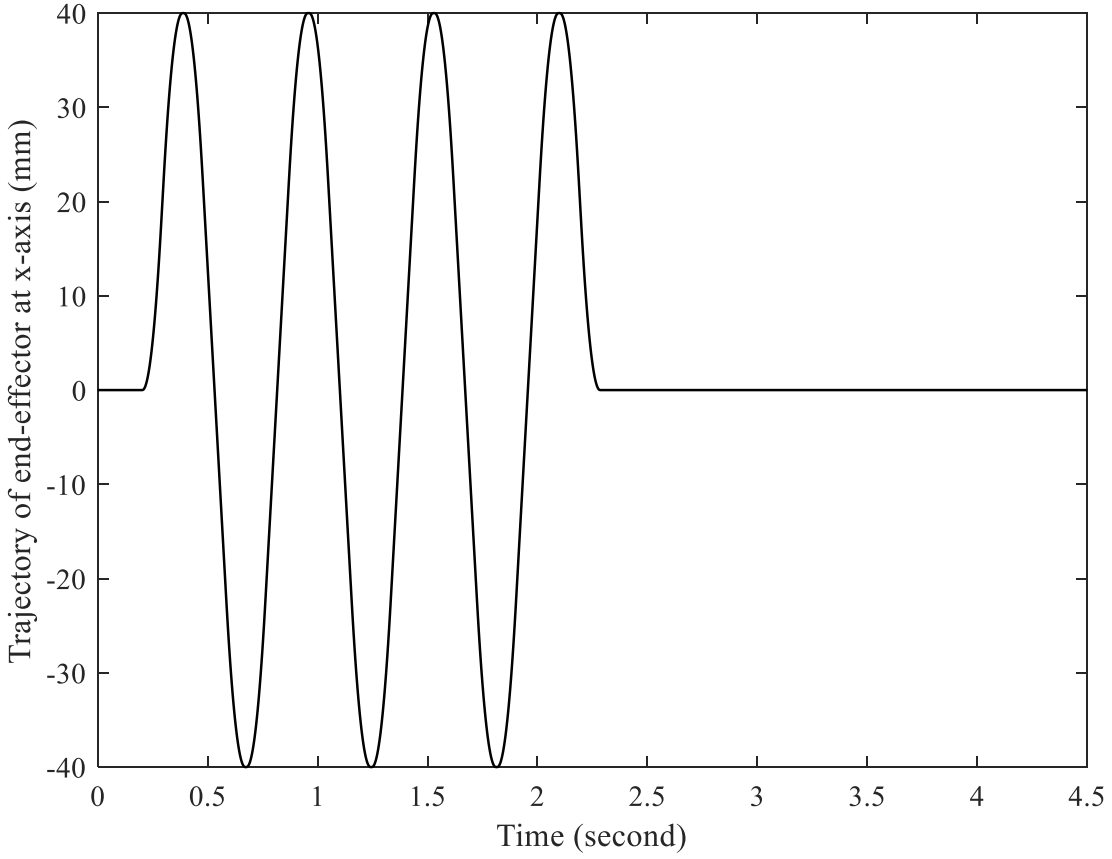

Figure 6.8. The given trajectory for the balancing tests at x-axis.

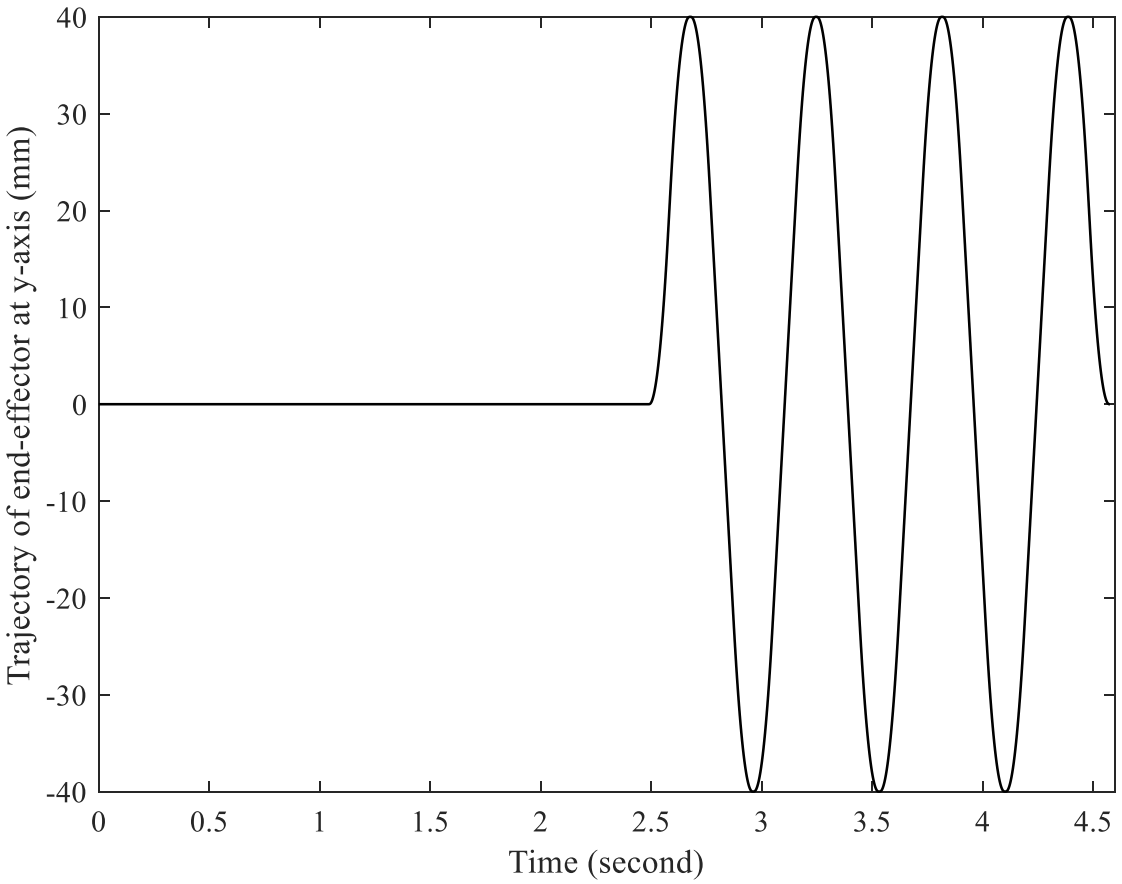

Figure 6.9. The given trajectory for the balancing tests at y-axis.

The test results are evaluated in terms of acceleration information for each axis. They are shown in Figures 6.10-13 for Condition-1, in Figures 6.14-18 for Condition-2, in Figures 6.19-22 for Condition-3 where red colour represents for the balanced mechanism and black colour represents for the unbalanced mechanism. Each figure has three graphs for x-motion and three graphs for y-motion. In addition, RMS values of acceleration information are separately calculated for x- motion and y-motion for each balancing test of the unbalanced and balanced mechanism. Thus, the percentage of acceleration reduction is observed and presented in following tables for each condition.

The percentage of acceleration reduction is shown in Table 6.9 for each axis and both motions for the tests for Condition-1. The maximum amount of reduction in acceleration is calculated for 1 g. For the motion along x-axis, the calculated reduction values for the x-axis are more than the values for the y-axis. For the motion along y-axis, the calculated reduction values for y-axis are more than the values for x-axis.

Table 6.9. The RMS acceleration values for Condition-1.

	Acceleration	x-axis	y-axis	z-axis
x-motion	1 g	52.31 %	43.77 %	35.57 %
	2 g	44.45 %	39 %	33.61 %
	3 g	40.77 %	34.37 %	37.57 %
	4 g	50.94 %	34.66 %	29.40 %
y-motion	1 g	49.85 %	54.58 %	46.1 %
	2 g	44.32 %	54.41 %	42.52 %
	3 g	43.07 %	52.45 %	41.15 %
	4 g	41.59 %	29.02 %	34.99 %

For Condition-2, each reduction value in the x-axis is more than other axes for both motions in contrast to Condition-1. The difference between Condition-1 and Condition-2 is payload at the end-effector. It can be said that the reduction values in x-axis for both motions are close to each other.

Table 6.10. The reduction of vibration for Condition-2.

	Acceleration	x-axis	y-axis	z-axis
x-motion	0.5 g	73.06 %	58.54 %	37.42 %
	1 g	70.93 %	51.83 %	43.2 %
	2 g	70.48 %	53.29 %	41.29 %
	3 g	72.37 %	49.14 %	45.06 %
	3.5 g	68.72 %	40.22 %	28.61 %
y-motion	0.5 g	62.70 %	50.73 %	47.72 %
	1 g	71.4 %	54.71 %	51.87 %
	2 g	70.65 %	57.95 %	52.22 %
	3 g	66.56 %	50.97 %	44.92 %
	3.5 g	55.04 %	35.16 %	33.29 %

The effect of payload is also observed for Condition-3. The shaking moments on the y-axis increase for larger end-effector payload. Therefore, the amount of reduction in the x-axis is greater than the y-axis. In order to realize the effects of shaking moments and shaking forces on the base, force sensors can be used instead of the accelerometers.

For all conditions, the minimum reduction value is obtained at the maximum motion acceleration for the y-axis.

Table 6.11. The reduction of vibration for Condition-3.

	Acceleration	x-axis	y-axis	z-axis
x-motion	0.5 g	66.38 %	59.2 %	40.24 %
	1 g	64.73 %	56.33 %	28.01 %
	2 g	53.11 %	54.95 %	30.19 %
	3 g	62.76 %	51.42 %	35.24 %
y-motion	0.5 g	60.84 %	51.64 %	37.16 %
	1 g	69.35 %	56.39 %	36.27 %
	2 g	68.31 %	65.90 %	42.78 %
	3 g	53.19 %	35.72 %	34.04 %

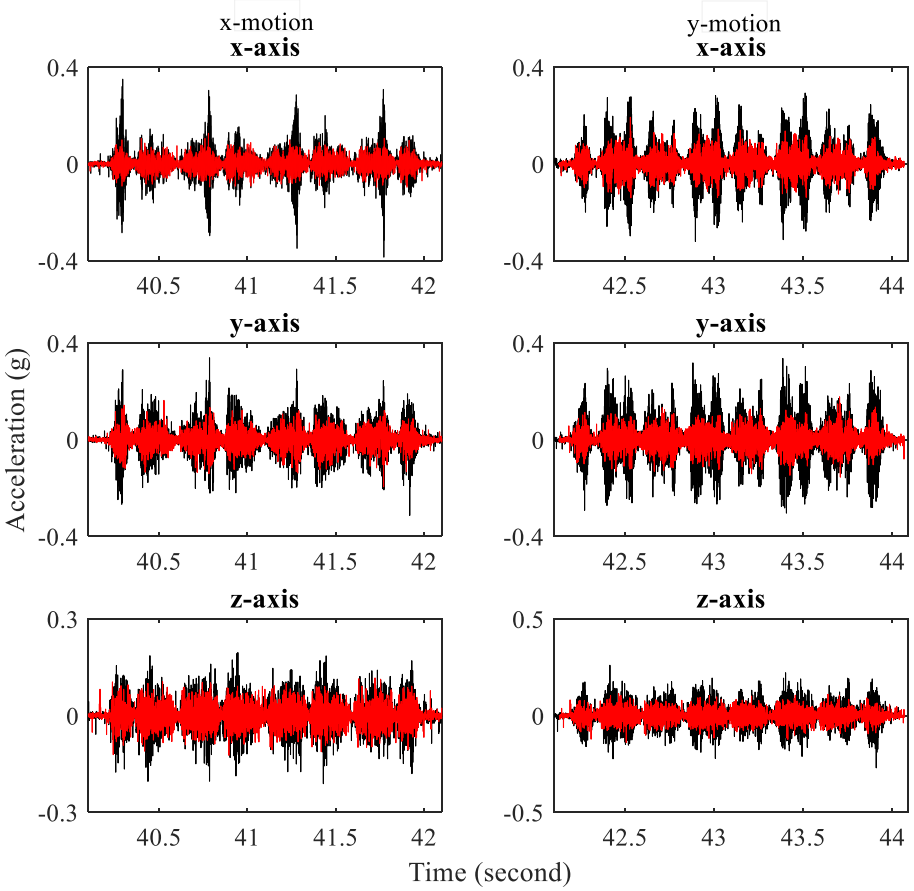

Figure 6.10. The effect of vibration on the base at 1 g for Condition-1.

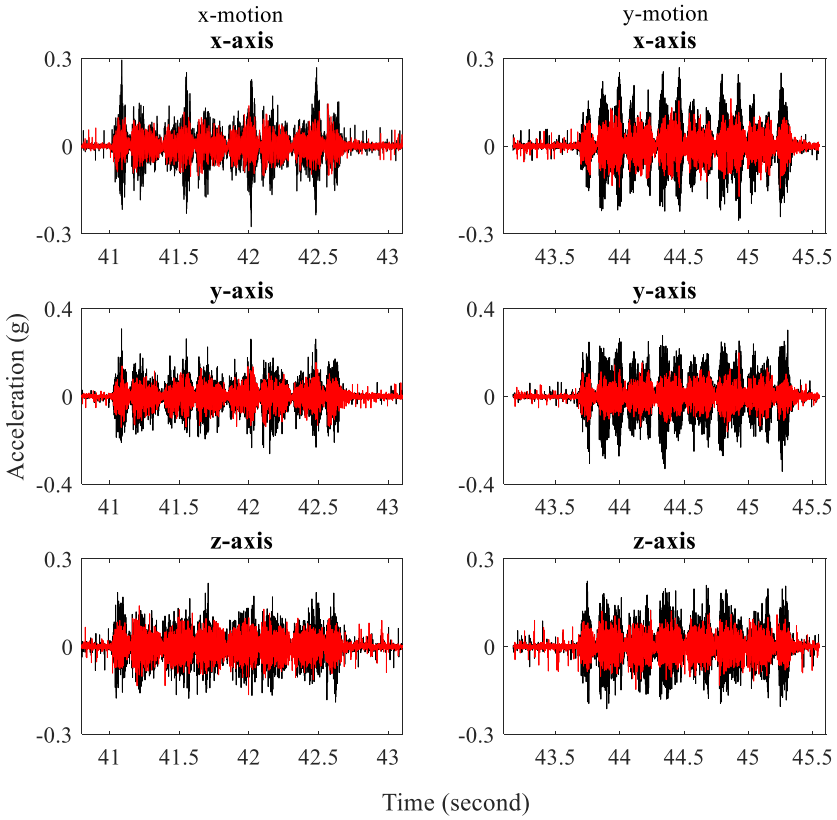

Figure 6.11. The effect of vibration on the base at 2 g for Condition-1.

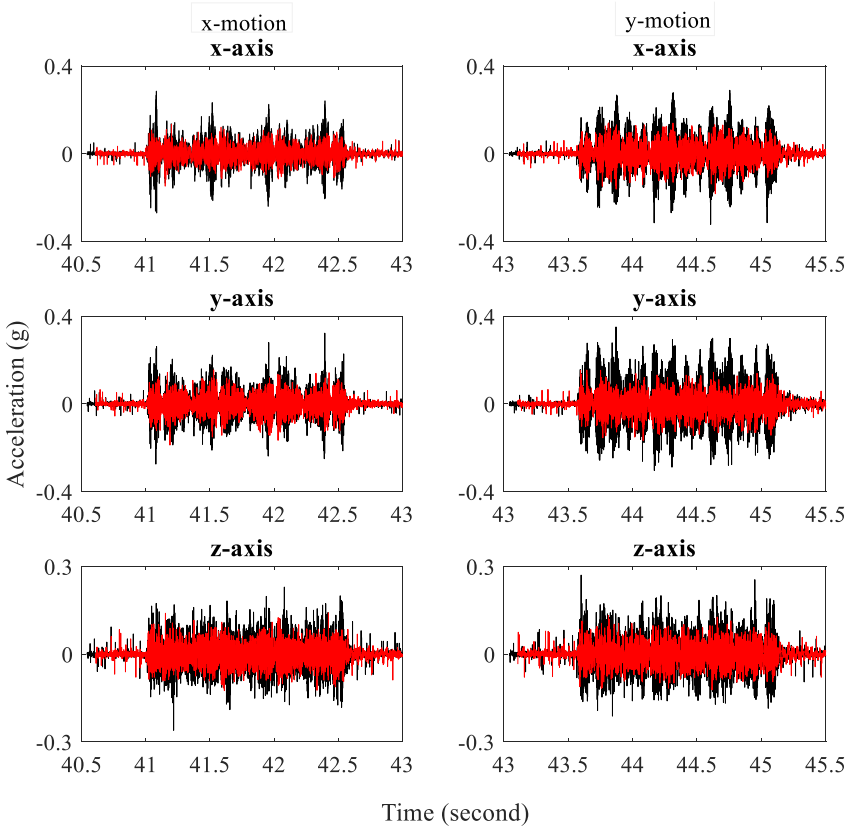

Figure 6.12. The effect of vibration on the base at 3 g for Condition-1.

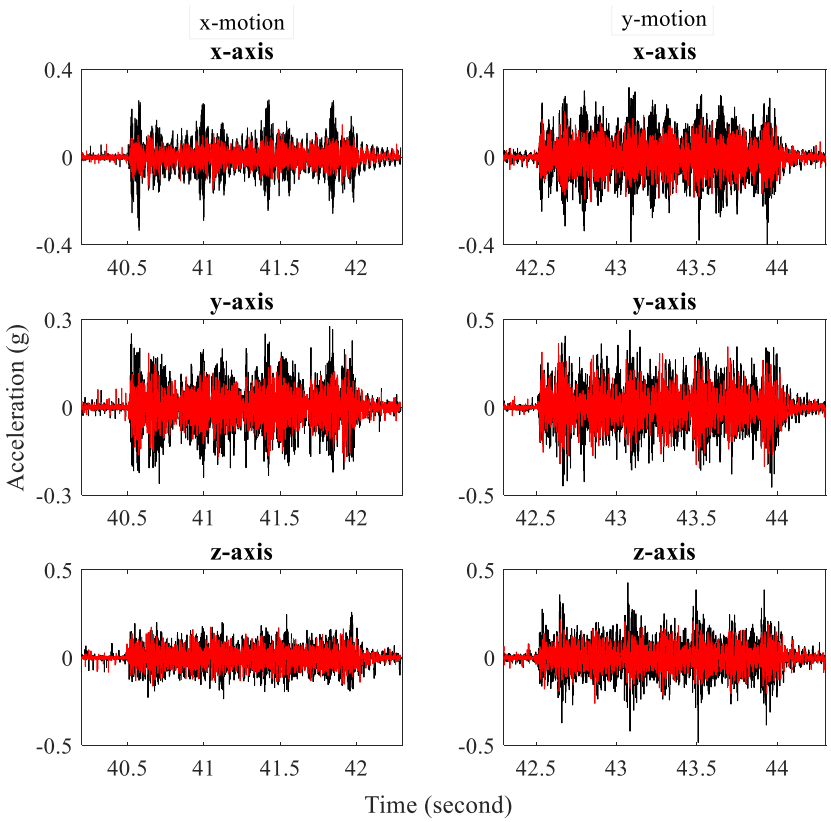

Figure 6.13. The effect of vibration on the base at 4 g for Condition-1.

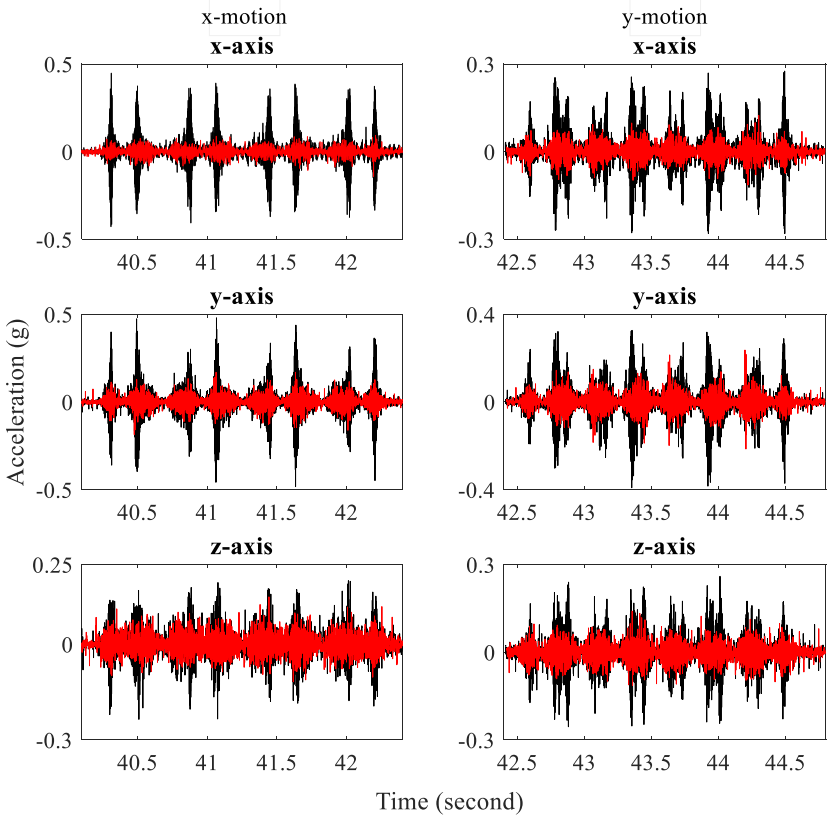

Figure 6.14. The effect of vibration on the base at 0.5 g for Condition-2.

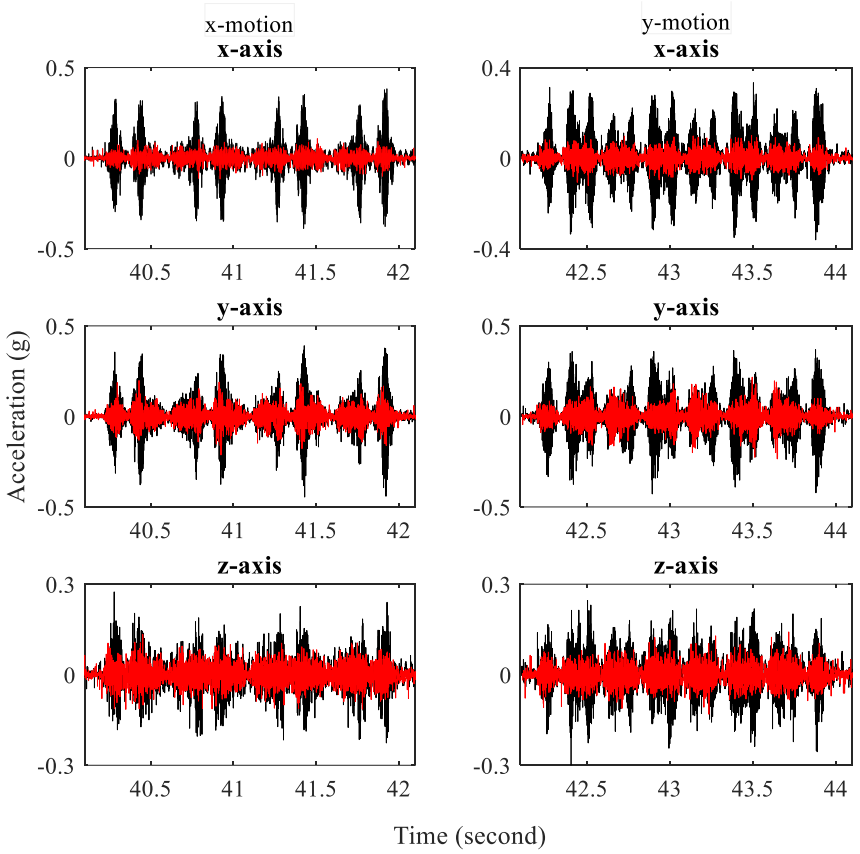

Figure 6.15. The effect of vibration on the base at 1 g for Condition-2.

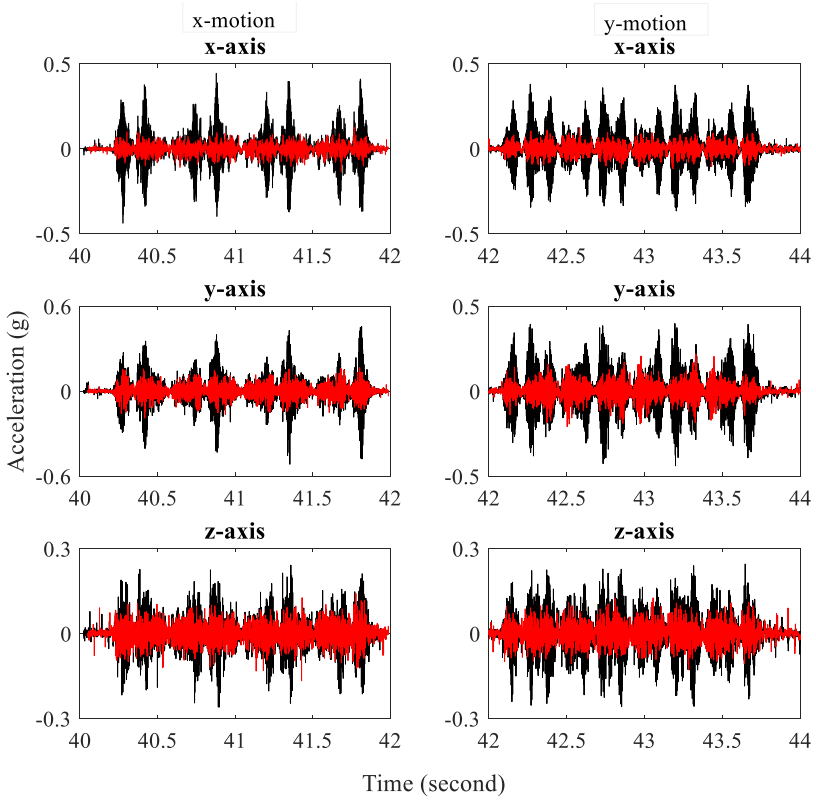

Figure 6.16. The effect of vibration on the base at 2 g for Condition-2.

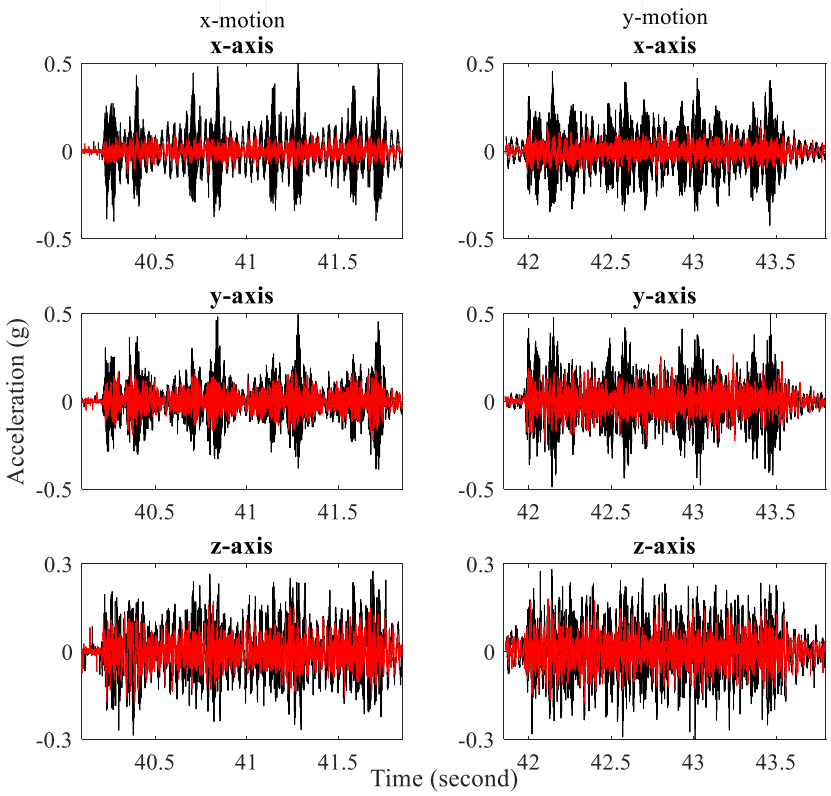

Figure 6.17. The effect of vibration on the base at 3 g for Condition-2.

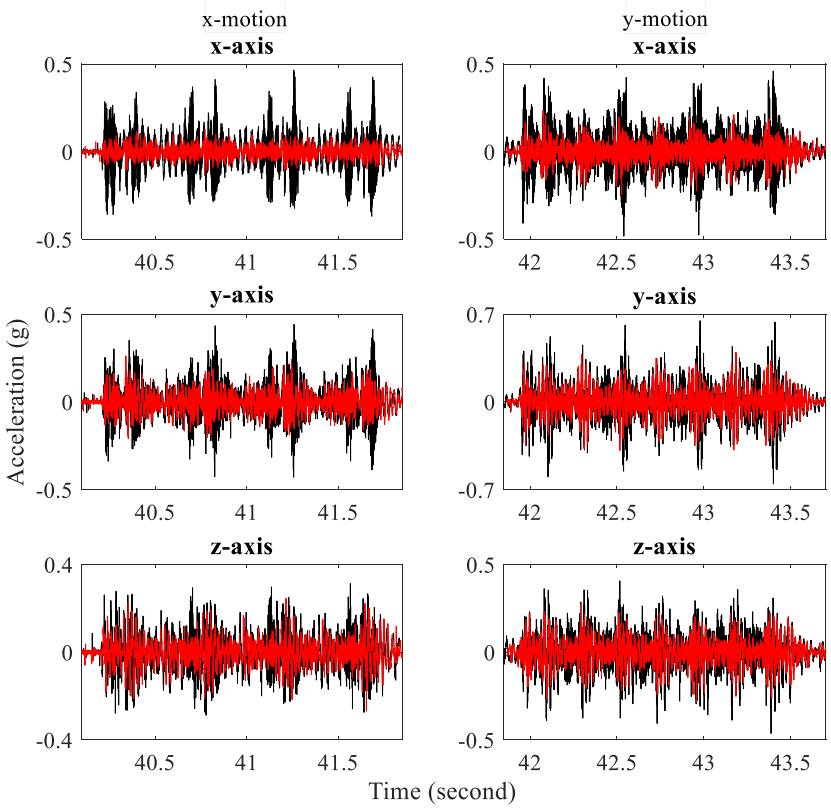

Figure 6.18. The effect of vibration on the base at 3.5 g for Condition-2.

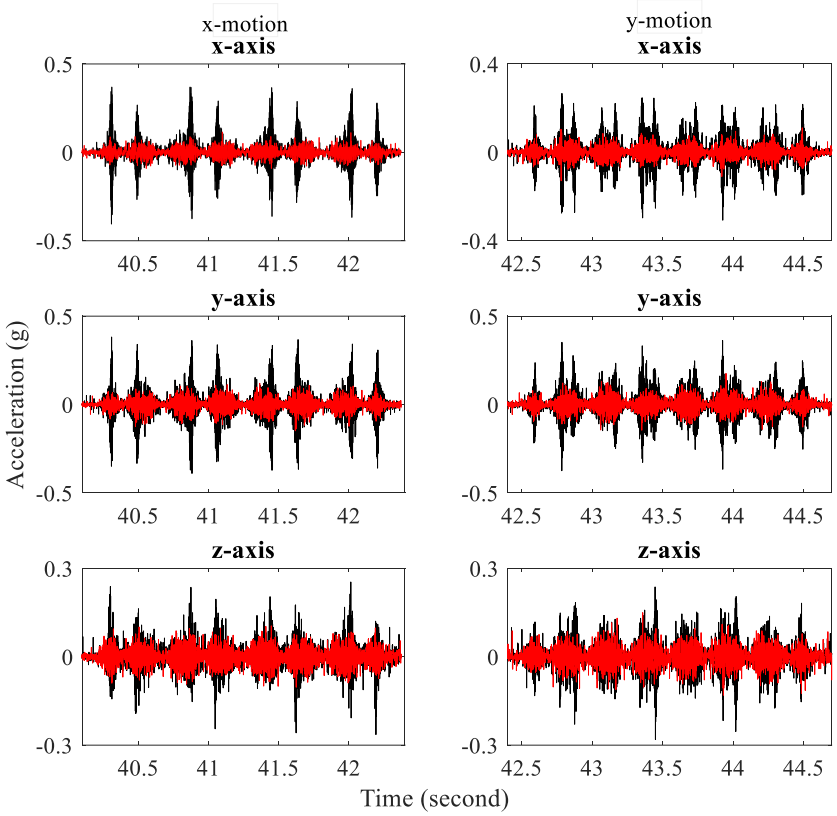

Figure 6.19. The effect of vibration on the base at 0.5 g for Condition-3.

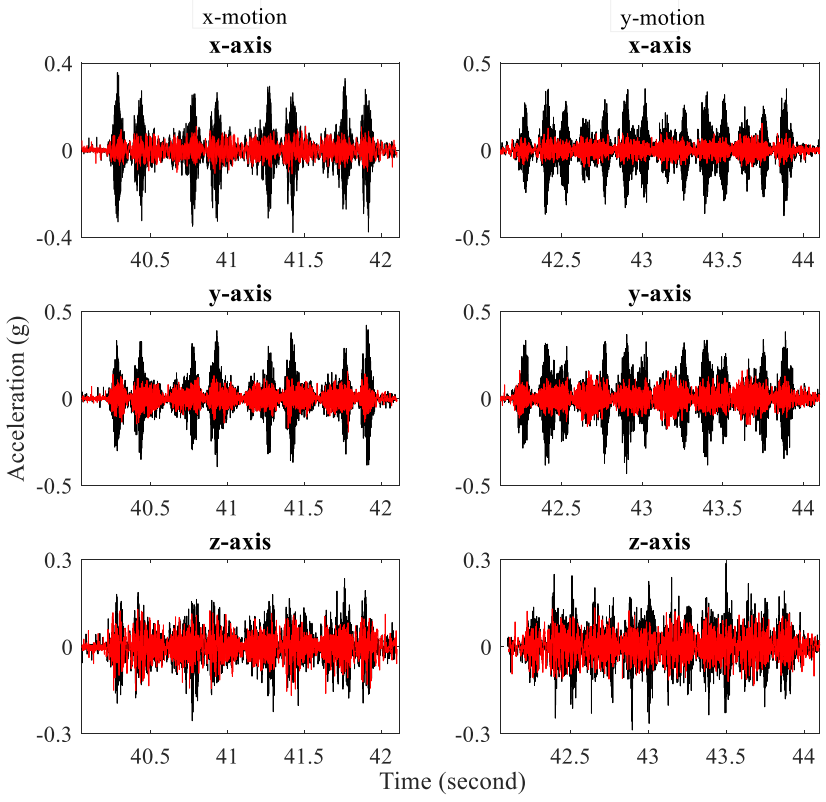

Figure 6.20. The effect of vibration on the base at 1 g for Condition-3.

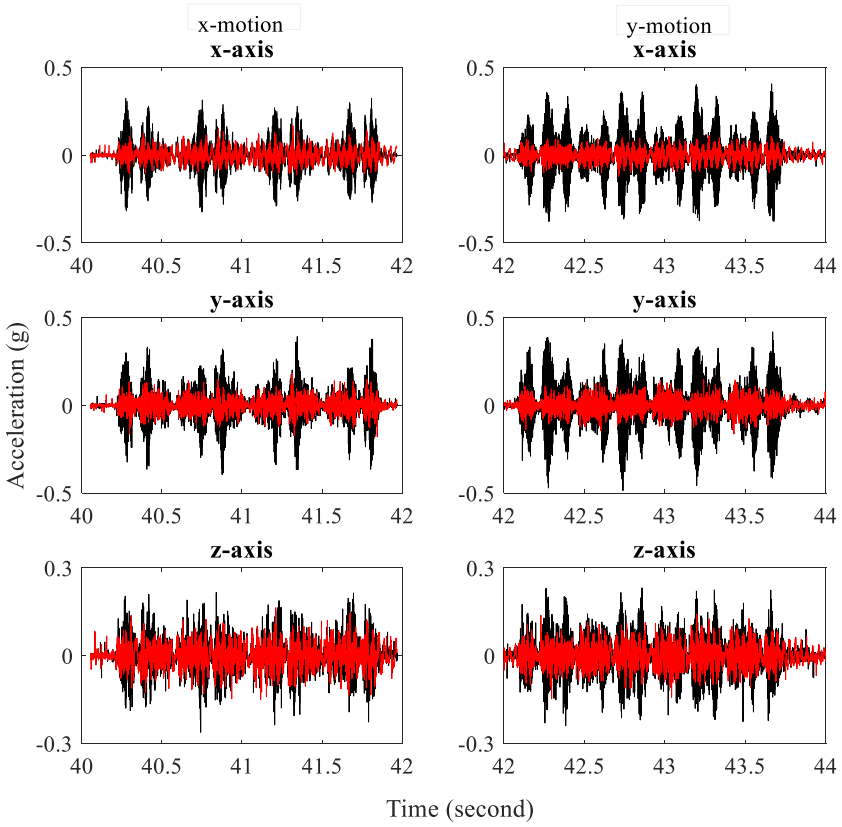

Figure 6.21. The effect of vibration on the base at 2 g for Condition-3.

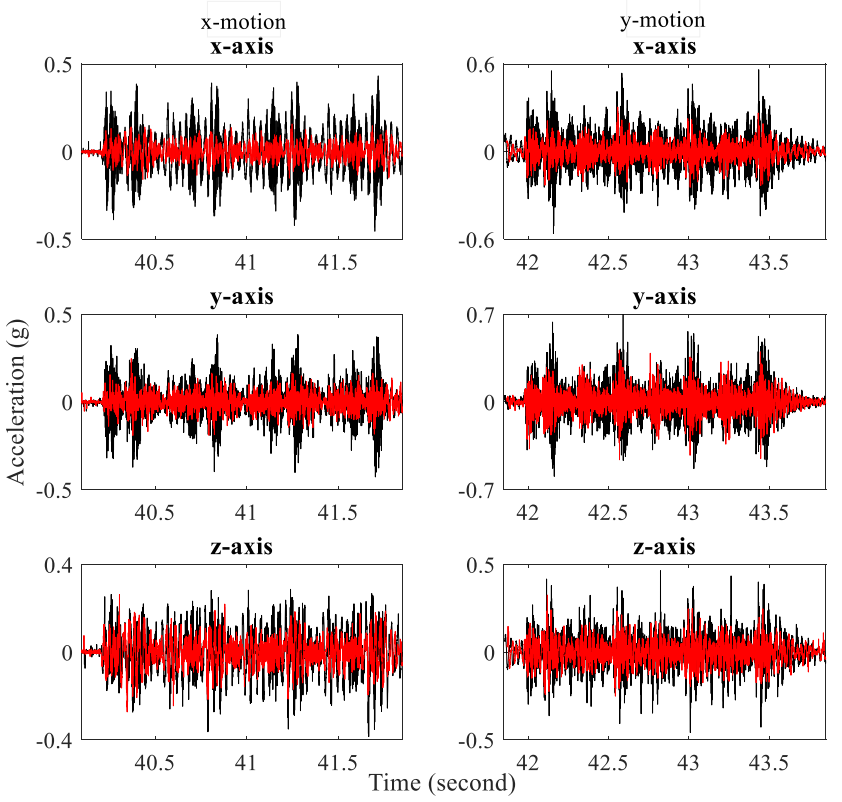

Figure 6.22. The effect of vibration on the base at 3 g for Condition-3.

The data obtained from the accelerometer (DYTRAN 7556A2) on the platform shows that the information whether the mechanism reaches the desired acceleration value. Some of the error is due to vibrations, whereas an important portion of the error is due to control input errors. Therefore, the acceleration information computed from the angular position information measured via the encoder. Firstly, the forward kinematics of the mechanism is used to find the position of the end-effector based on the encoder data. Then, the acceleration information is obtained by taking the derivative of the position information twice. However, both acceleration data have undesirable signals at different frequency values. It is necessary to eliminate the undesirable signals to compare with the desired acceleration value. Therefore, bandpass filters are used is applied to filter both acceleration data measured from the accelerometer and computed from the encoder data. Firstly, dominant frequency values are investigated from the Fast Fourier Transform (FFT) spectrum graph in order to find lower and upper frequency for each motion acceleration value. Then, the values of lower and upper frequency are tried to obtain the most convergent graph. Figures 6.23-27 indicate the desired acceleration, accelerometer data and the encoder based calculated data for given motions at 1g, 2g, 3g, 4g, 5g, respectively for the mechanism which is without the end-effector and the balancing masses.

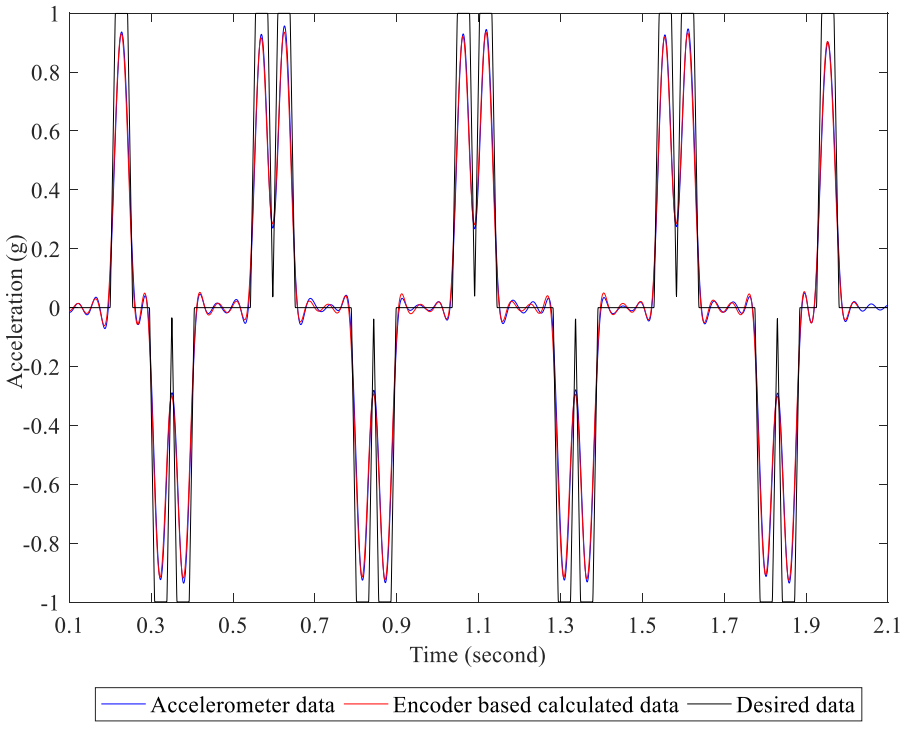

Figure 6.23. The comparison of acceleration data at 1 g.

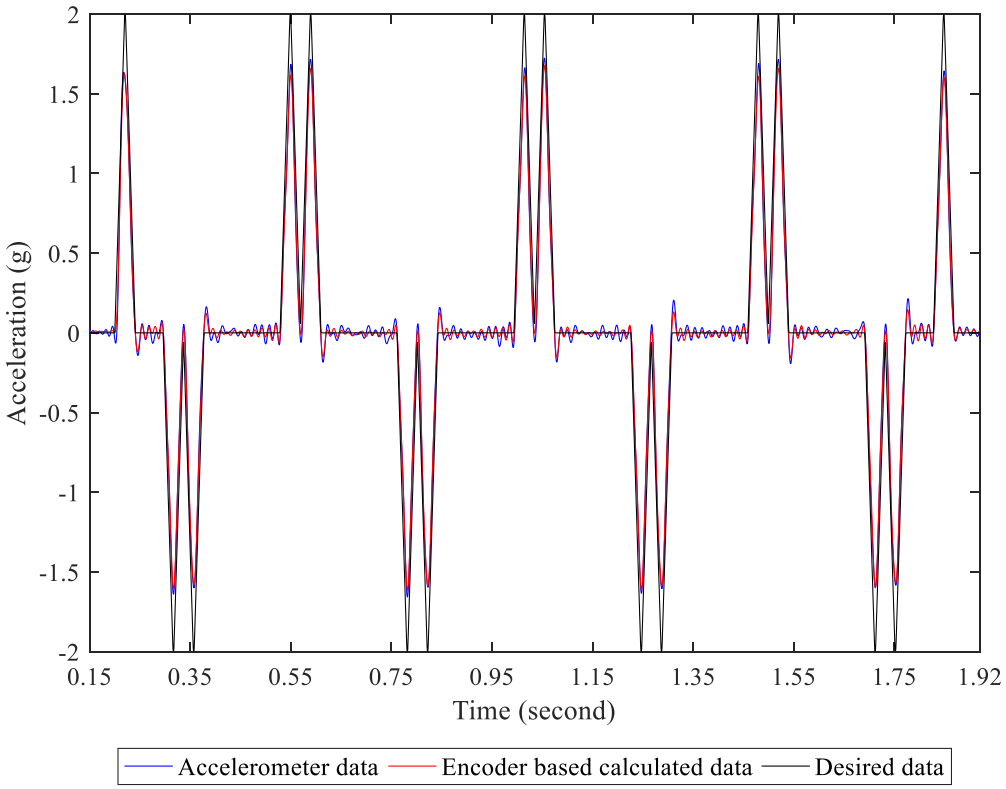

Figure 6.24. The comparison of acceleration data at 2 g.

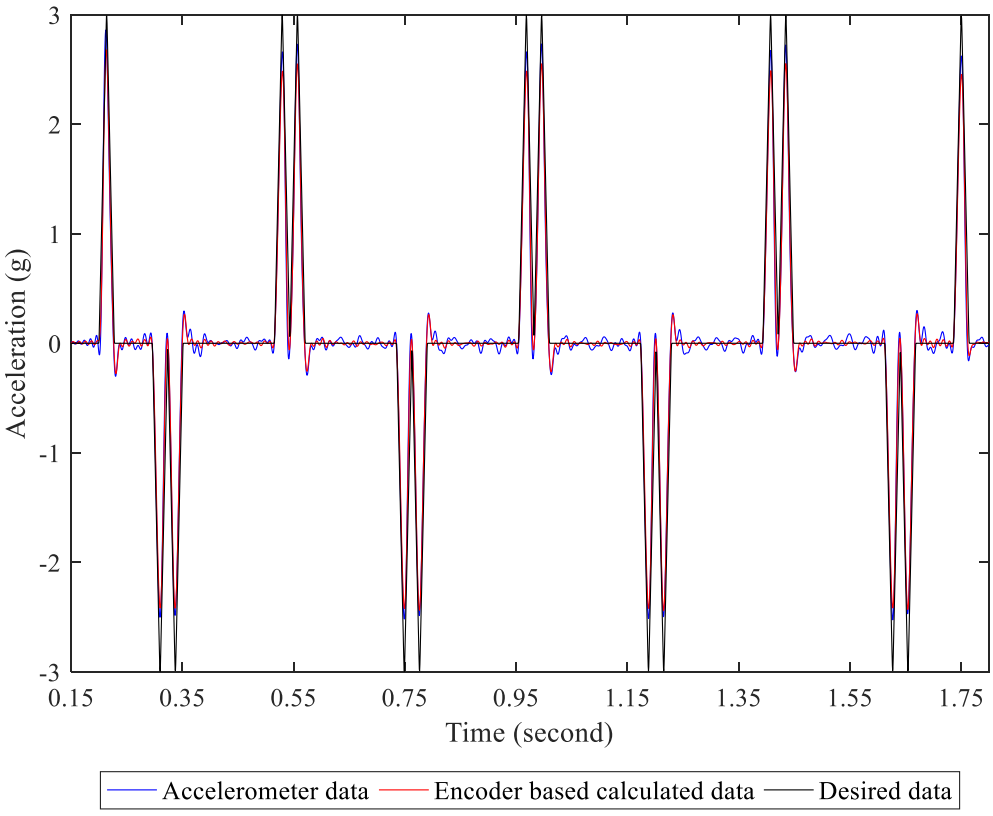

Figure 6.25. The comparison of acceleration data at 3 g.

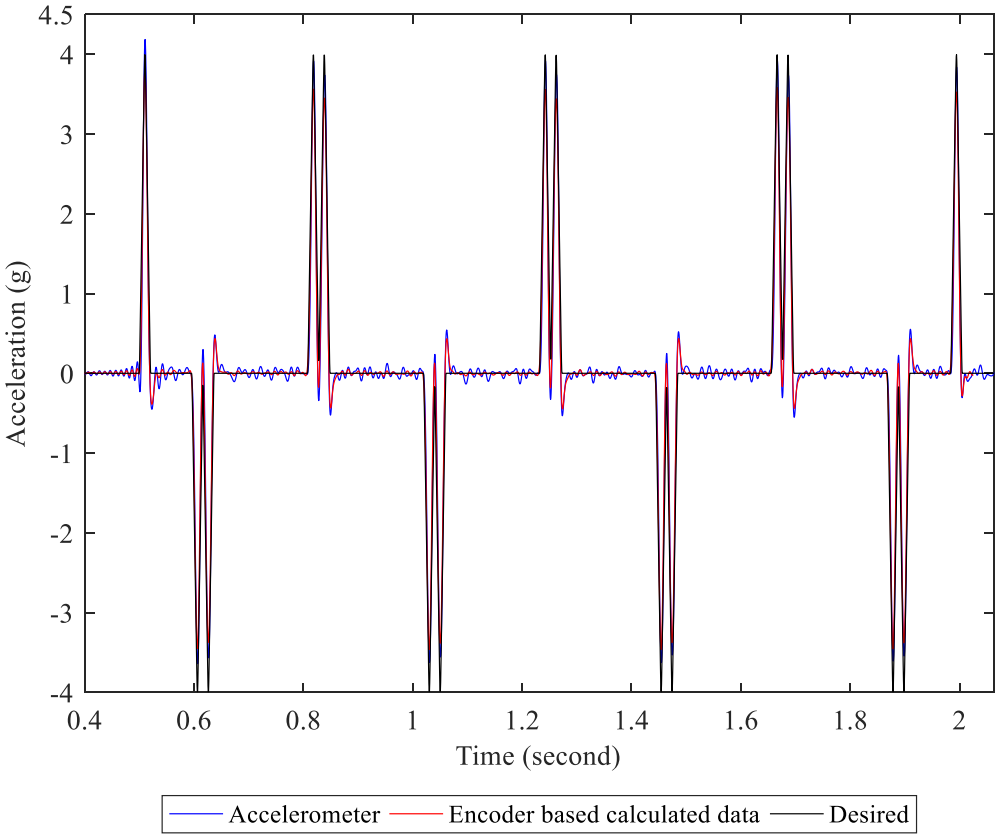

Figure 6.26. The comparison of acceleration data at 4 g.

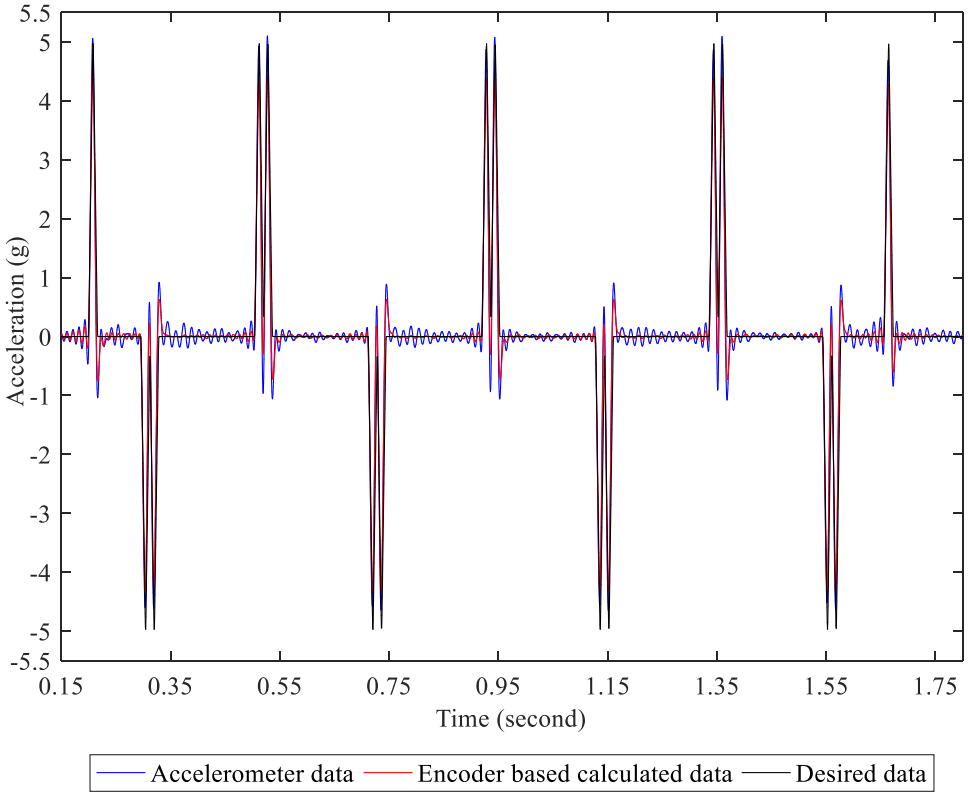

Figure 6.27. The comparison of acceleration data at 5 g.

Figures 6.28-30 present the comparison graphs for the unbalanced and balanced mechanism for the higher motion acceleration value of each condition. The end-effector acceleration is presented for Condition-1 at 4 g acceleration motion, for Condition-2 at 3.5 g acceleration motion, for Condition-3 at 3 g acceleration motion. Again, bandpass filter is applied to eliminate undesired signals. For each condition, the same lower and upper frequency values are used. The encoder based calculated data give results closer to the desired value with the selected frequency values.

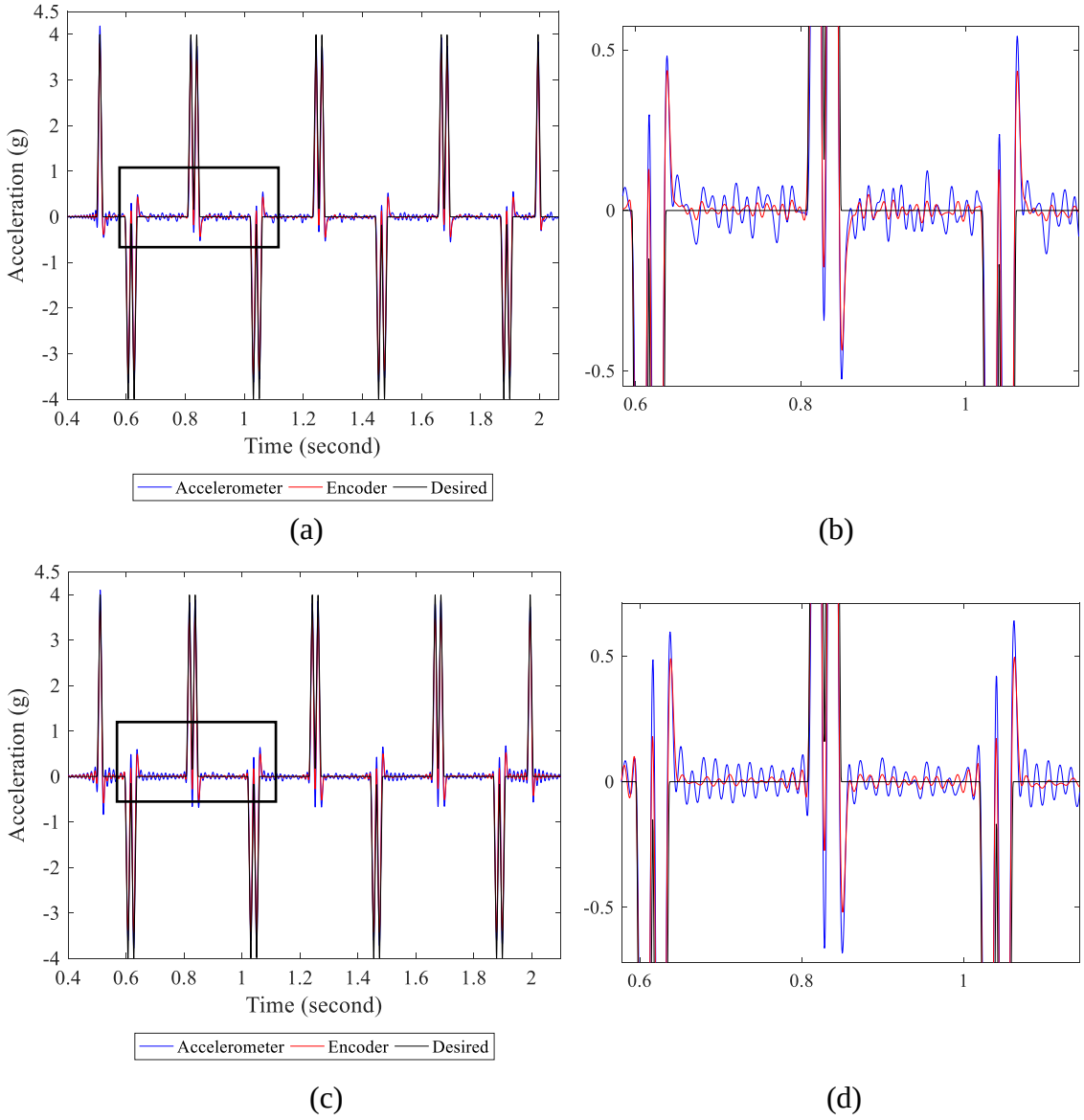

Figure 6.28. The comparison of acceleration data at 4 g motion of Condition-1 for: (a) the unbalanced mechanism, (b) zoom of (a) graph, (c) the balanced mechanism, (d) zoom of (c) graph.

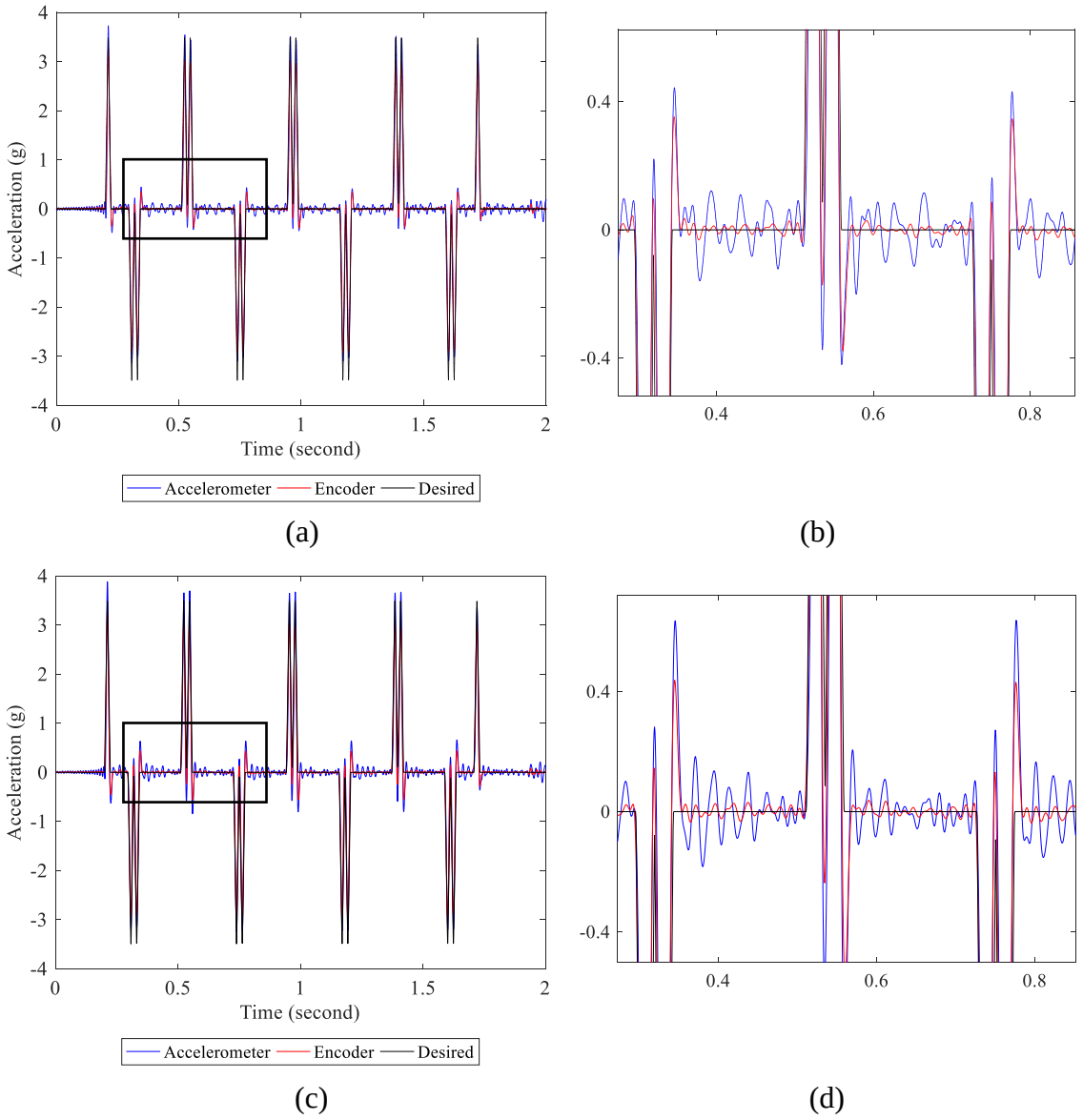

Figure 6.29. The comparison of acceleration data at 3.5 g motion of Condition-2 for: (a) the unbalanced mechanism, (b) zoom of (a) graph, (c) the balanced mechanism, (d) zoom of (c) graph.

When all zoom graphs are examined, it is seen that the balanced mechanism has more regular oscillation curves in the acceleration graphs. However, the amplitude of oscillation curves in the graphs of the balanced mechanism are greater than in the graphs of the unbalanced mechanism. As a conclusion according to these graphs, the controller parameters of actuators should be tuned separately for the unbalanced and balanced mechanism.

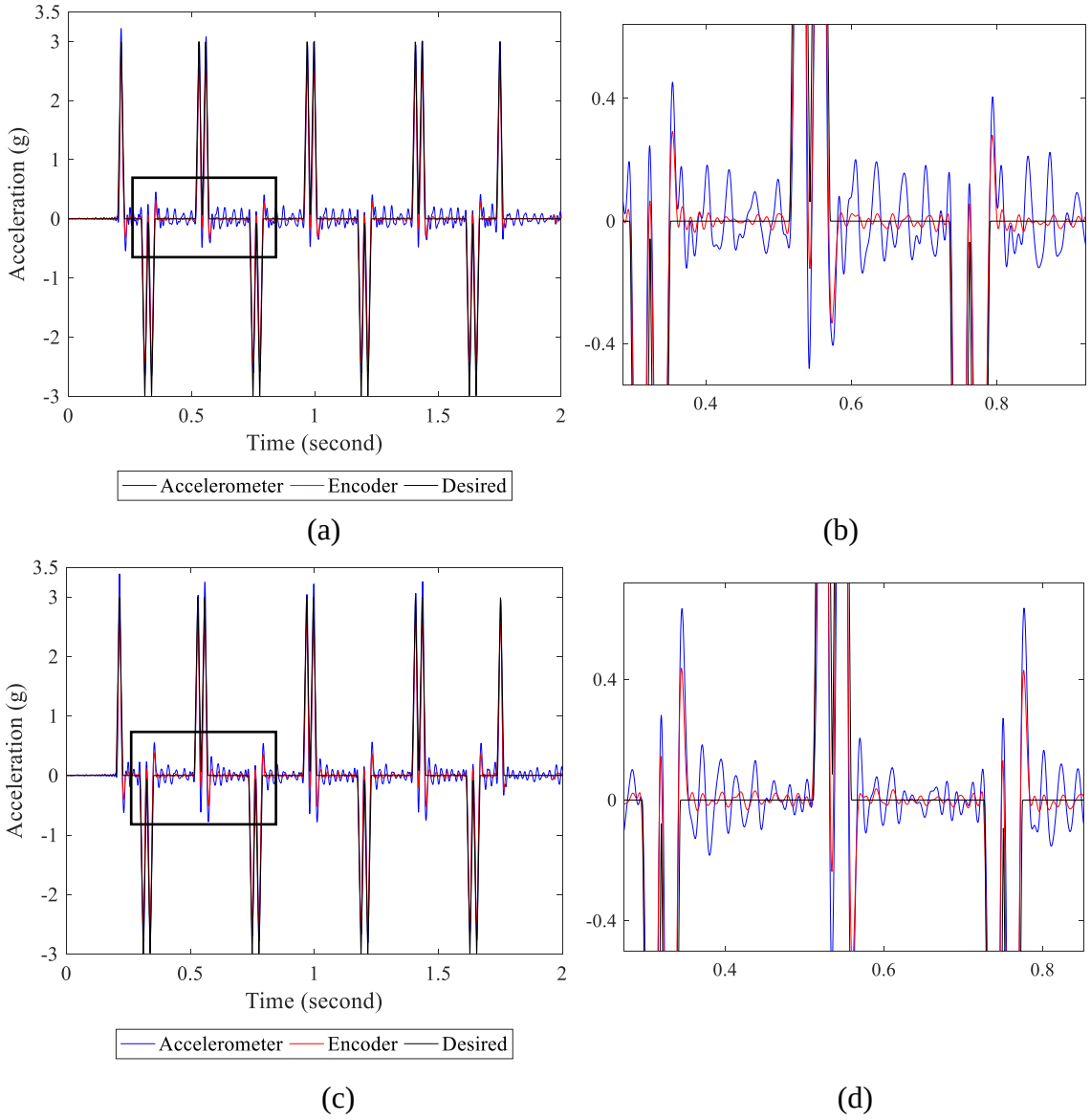

Figure 6.30. The comparison of acceleration data at 3 g motion of Condition-3 for: (a) the unbalanced mechanism, (b) zoom of (a) graph, (c) the balanced mechanism, (d) zoom of (c) graph.

The actuator torque is calculated from the Lagrange method with Equations 3.44-45 for the given motion on the x-axis and y-axis for all balancing tests. The calculated torque is shown for Condition-3 at 3 g motion acceleration in Figure 6.31 to compare the balanced mechanism with the unbalanced mechanism. The maximum requirement torque is 19.27 N.m for the unbalanced mechanism, whereas it is 31.86 N.m for the balanced mechanism. The increase in torque requirement is due to the addition of balancing masses to the system.

On the other hand, the actuator torque is obtained by multiplying the current information received from one of the actuators by actuator torque constant and reducer

constant. The graphs are presented for the unbalanced and balanced mechanism in Figure 6.32 for Condition-3 at 3 g motion acceleration. The maximum torque is 117.6 N.m for the unbalanced mechanism, whereas it is 138 N.m for the balanced mechanism.

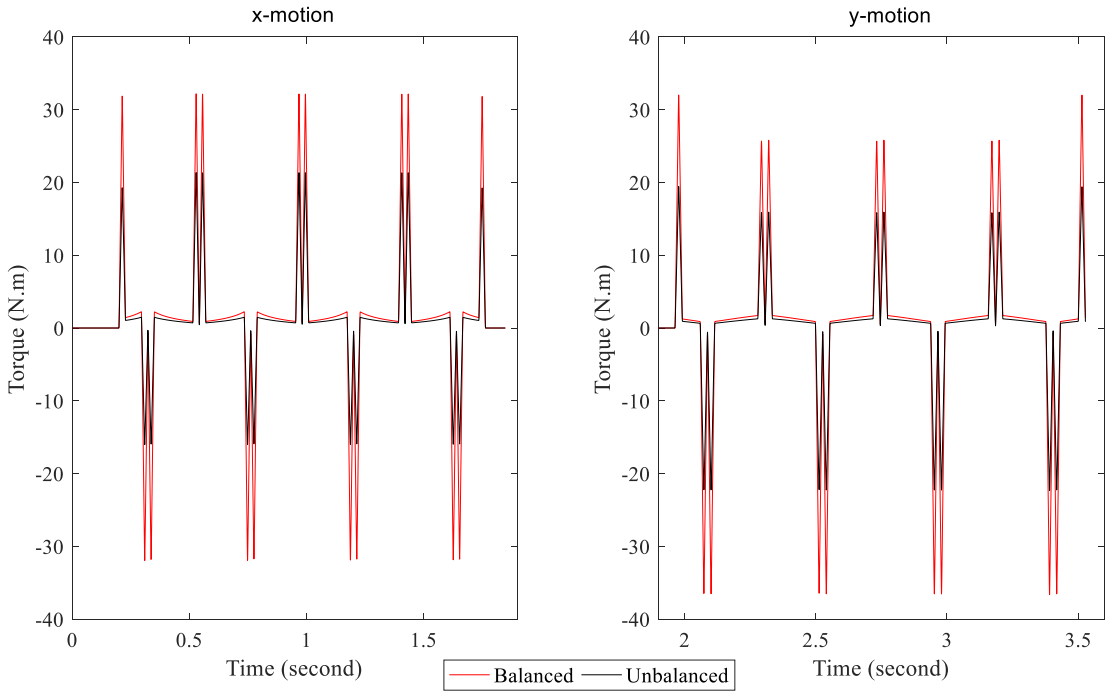

Figure 6.31. The calculated torque values from Lagrange method.

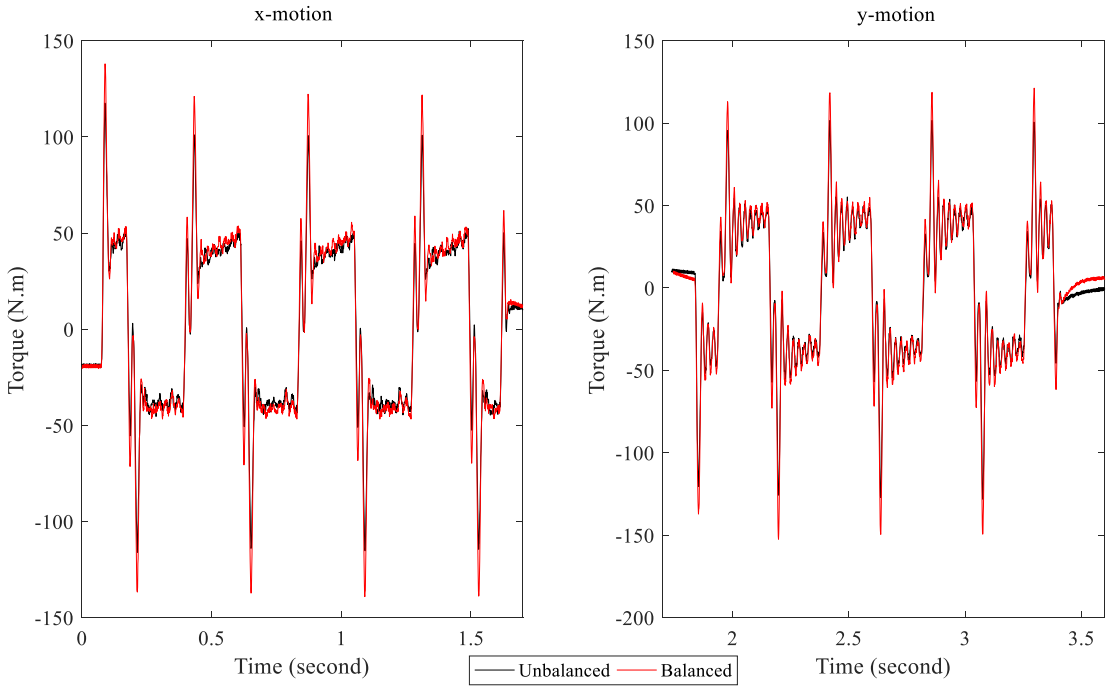

Figure 6.32. The calculated torque values from the current information of actuator.

A major difference is obtained between the torque calculated from the current information and the theoretical torque calculated from Lagrange method. The primary reason for this is that the theoretical torque is computed for the change in the kinetic energy. But there is also work done for dissipated energy and change in potential energy. The dissipative energy is due to friction in the joints and reducers of the mechanism. The potential energy is due to the strain energy of the links in the mechanism. There are peak values at the points which are acceleration/deceleration zones of the input motion. These unexpectedly high values may also occur due to the controller parameters. They should be enhanced for the balanced and unbalanced mechanism separately according to payload and balancing masses.

CHAPTER 7

CONCLUSIONS

The purpose of the thesis is to observe the effect of dynamic balancing and calibration on the positioning accuracy of parallel robots with experiments performed on an over-constrained parallel mechanism. Firstly, the alternatives of the 2-dof parallel mechanisms were evaluated and over- and simply constrained 6R mechanisms were selected.

Kinematic model, balancing calculations, dynamic models with balancing masses were derived for the selected mechanism. The constructional design studies were carried out in SolidWorks® environment based on the thesis criteria. The prototypes of the mechanisms were built for the balancing tests. The carbon-fiber composite material was used for the links. Thus, the know-how was obtained about manufacturing of links from the composite material and assembling to Aluminium parts. The calibration procedure is implemented before the balancing tests. Then, the balancing tests are performed using accelerometers according to the given test steps. Test results are presented in terms of acceleration values measured on the base and the positioning accuracy measured at the end-effector.

The calibration studies were carried out in two stages. The results of the calibration studies are expressed in terms of positional deviation and positional uncertainty according to VDI 3441/ DGQ standard. For the unbalanced mechanism with end-effector connected to the moving platform, positional deviation was decreased from 181 μm to 81 μm for the x-axis of the mechanism, from 117 μm to 53 μm for y-axis of the mechanism. Positional uncertainty was reduced from 218 μm to 151 μm for x-axis of the mechanism, from 163 μm to 127 μm for y-axis of the mechanism. The decrease in positional deviation and positional uncertainty values shows that the positioning accuracy and repeatability of the mechanism is improved. The maximum deviation from desired point is reduced from 180 μm on the x-axis of the non-calibrated mechanism to 76 μm on the x-axis of the calibrated mechanism. The maximum deviation from desired point decreased from 117 μm on the y-axis of the non-calibrated mechanism to 72 μm on the

y-axis of the calibrated mechanism. These results demonstrate that the calibration studies have enhanced the positioning accuracy and repeatability of the end-effector.

Balancing tests were carried out with the balancing masses and the accelerometer on the base. Three different conditions were specified in terms of working conditions of the mechanism. These conditions are just the platform (as 1.45 kg payload), the platform with the end-effector (as 3.41 kg payload) and the platform with the end-effector and extra masses (as 5 kg payload). The mechanism was run at different acceleration values for each condition with balancing masses which are calculated to fully balance the mechanism. Thus, the acceleration data were obtained from the accelerometer for each test. The results were presented to show the reduction of vibration effect on the base with graphs. RMS values of acceleration data were calculated for the unbalanced and balanced mechanism for each test. The graphs and tables show that the balancing masses reduce the vibrations affecting the base. As can be seen from the tables, the balancing masses have reduced the vibrations by at least 30 % for Condition-1, 35 % percent for Condition-2, 36 % for Conditon-3 in x- or y-directions.

The accelerometer on the platform was used to observe whether the mechanism reaches the desired acceleration value. On the other hand, the acceleration data were calculated from the information of measured position via encoders. Thus, the data from the accelerometer and the data from the encoders were filtered to compare with each other and also desired acceleration values (1 g, 2 g, 3 g, 4 g, 5 g). Both acceleration data follow the desired acceleration trajectory fairly well, but there are differences between the measured and the desired acceleration values dues to several reasons (Figures 6.23-27). Firstly, the acceleration data computed from the encoder data is the second derivative of the calculated end-effector position from the forward kinematics of the mechanism using motor encoders' data. Therefore, it can be assumed that there are computational errors. Also the PID controller cannot perfectly follow the desired trajectory. The acceleration data from the accelerometer have differences caused by manufacturing errors, friction in the joints, stiffness of the links. But the errors are in acceptable range. In addition, the comparison graphs of acceleration data were also carried out to see the difference between unbalanced and balanced cases for the maximum motion acceleration value of conditions which are 4 g motion for Condition-1, 3.5 g motion for Condition-2, 3 g motion for Condition-3. Looking at the graphs, although more regular oscillation curves are obtained for the balanced mechanism, the amplitude of oscillations are larger than the unbalanced

mechanism contrary to the expectations. This indicates that the PID controller parameters must also be properly set for the balanced mechanism.

Lastly, the torque requirement of actuators was theoretically calculated from the Lagrange method for the given 3.5 g motion of Condition-3 to compare with the taken data from the actuators. In addition, the difference of torque requirement was obtained between the unbalanced mechanism and the balanced mechanism. The calculated torque value and the actuator data shows that as the balancing masses are added, the torque requirement of the actuators increases. On the other hand, a major difference is observed between the calculated torque and the actuator data. The main reason of this is that the torque calculated from Lagrange method just evaluates the kinetic energy requirements. Nevertheless, the difference between the two torque values is greater than the expected values. Therefore, PID controller parameters need to be modified.

In the future works, the calibration studies can be enhanced with iterations. On the other hand, measurements can be taken from both positive and negative directions of motions. The error matrices can be reconstructed with the mean of measurements for each point in both directions. Thus, better results can be obtained with the reconstructed error matrices and iterations. Also many improvements can be performed for the balancing tests. Currently, the accelerometers show the effect of vibration caused by moments and forces acting on the base as acceleration data. Therefore, it is not possible to distinguish between moment and force information with the accelerometer data. For this reason, the balancing tests can be realized using force sensors to show the effect of balancing masses in terms of shaking force.

It should be noted that, for future studies, for a comparison between over-constrained and simply constrained mechanism the methodologies developed in this thesis are aimed to be applied to a simply constrained version of the mechanism, which is kinematically equivalent to the modified 6R mechanism. The simply constrained version of the mechanism is obtained by removing one of the links of the existing over-constrained mechanism. The prototype of the simply constrained mechanism was produced as seen in Figure 5.12. The calibration studies and the balancing tests are planned to be applied on the simply constrained mechanism as a future work. Thus, the results of the studies shall be compared between the two parallel mechanisms and compared with the unbalanced and balanced ones.

REFERENCES

Alıcı, G. Determination of Singularity Contours for Five-bar Planar Parallel Manipulators. *Robotica* 2000, 18(5), 569-575.

Alıcı, G. An Inverse Analysis of Five-bar Planar Parallel Manipulators. *Robotica* 2002, 20(2), 195-201.

Alıcı, G.; Shirinzadeh, B. Optimum Force Balancing with Mass Distribution and Single Elastic Element for a Five-bar Parallel Manipulator. *In Robotics and Automantion ICRA'03: Proceedings of International Conference on Robotics and Automation*, Taipei, Taiwan, Sept 14-19, 2003: IEEE Xplore, 2003; Vol 3, 3666-3671.

Alıcı, G; Shirinzadeh, B. Optimum Dynamic Balancing of Planar Parallel Manipulators. *In Robotics and Automation ICRA'04: Proceeding of International Conference on Robotics and Automation*, New Orleans, LA, USA, Apr 26 - May 1, 2004: IEEE Xplore: 2004; Vol 5, 4527-4532.

Alıcı, G., Shirinzadeh, B. Optimum Dynamic Balancing of Planar Parallel Manipulators Based on Sensitivity Analysis. *Mechanism and Machine Theory* 2006, 41(12), 1520-1532.

Angeles, J.; Lee, S. K. The Formulation of Dynamical Equations of Holonomic Mechanical Systems Using a Natural Orthogonal Complement. *Journal of Applied Mechanics* 1988, 55(1), 243.

Arakelian, V.; Dahan, M.; Smith, M. A Historical Review of the Evaluation of the Theory on Balancing of Mechanisms. In History of Machines and Mechanisms HMM 2000: Proceedings of International Symposium on History of Machines and Mechanisms, Cassino, Italy, May 11-13, 2000: Springer: Dordrecht, 2000, pp 291-300.

Arakelian, V. H.; Smith, M. R. Erratum: Shaking Force and Shaking Moment Balancing of Mechanisms: A Historical Review with New Examples. *Journal of Mechanical Design* 2005, 1034-1035.

Arakelian, V. H.; Smith, M. R. Shaking Force and Shaking Moment Balancing of Mechanisms: A Historical Review with New Examples. *Journal of Mechanical Design* 2005, 127(2), 334-339.

Arekelian, V. H.; Smith M. R. Design of planar 3-DOF 3-RRR reactionless parallel Manipulators. *Mechatronics* 2008, 601-606.

Asada, H.; Youcef Toumi, K. Analysis and Design of a Direct-drive Arm with a Five-bar-link Parallel Drive Mechanism. *Journal of Dynamic Systems, Measurements and Control* 1984, 106(3), 225-230.

Berkof, R. S.; Lowen, G. G. A New Methof for Completely Force Balancing Simple Linkages. *ASME Transaction on Journal of Engineering for Industry* 1969, 91(1), 21-26.

Bonev, I. Delta Parallel Robot- The Story of Success, 2001. ParalleMIC. https://www.parallemic.org/Reviews/Review002p.html (accessed Feb 6, 2019).

Bonev, I. The True Origins of Parallel Robots, 2003. ParalleMIC. https://www.parallemic.org/Reviews/Review007.html (accessed Feb 4, 2019).

Bourbonnais, F.; Bigras, P., Bonev, I. A.; Minimum-time Trajectory Planning and Control of a Pick-and-place Five-bar Parallel Robot. *IEEE/ASME Transactions on Mechatronics* 2015, 20(2), 740-749.

Briot, S.; Bonev, I. Are Parallel Robots More Accurate Than Serial Robots? *Transaction of the Canadian Society for Mechanical Engineering* 2007, 31(4), 445-455.

Briot, S.; Arakelian, V. H.; Le Baron, J. P. Shaking Force minimization of High-speed Robots via Centre of Mass Acceleration Control. *Mechanism and Machine Theory* 2012, 57, 1-12.

Buganza, A; Acevedo, M. Dynamic Balancing of a 2-DOF 2RR Planar Parallel Manipulator by Optimization. In Mechanism and Machine Science: Proceeding of the 13th World Congresss in Mechanism and Machine Science, Guanajuato, Mexico, June 19-25, 2011.

Burisch, A.; Wrege, J.; Raatz A.; Hesselbach, J.; PARVUS-Miniaturized Robot for Improved Flexibility in Micro Production. *Assembly Automation* 2007, 27(1), 65-73.

Cervantes, M. G.; Cruz- Villar, C. A.; Alvarez- Gallegos, J.; Portilla-Flores, E. A. Differential Evolution Techniques for the Structure-control Design of a Five-bar Parallel Robot. *Engineering Optimization* 2010, 42(6), 535-565.

Cervantes-Sanchez, J. J.; Rendon-Sanchez, J. G. A Simplified Approach for Obtaining the Workspace of a Class of 2-dof Planar Parallel Manipulators. *Mechanism and Machine Theory* 1999, 34, 1057-1073.

Chaudhary, H.; Saha, S. K. Balancing of Shaking Forces and Shaking Moments for Planar Mechanisms Using the Equimomental Systems. *Mechanism and Machine Theory* 2008, 43(3), 310-334.

Clavel, R. Device for The Movement and Positioning of an Element in Space. U.S. Patent 4,976,582, Dec. 11, 1990.

Compas, L.; Bourbonnais F.; Bonev I. A.; Bigras, P. Development of a Five-bar Parallel Robot with Large Workspace. *In ASME 2010 International Design Engineering Technical Conferences and Computers and Information in Engineering Conference*: 34th Annual Mechanisms and Robotics Conference, Montreal, Que, Canada, August 15-18, 2010; 917-922.

Cox, D. K.; Freeman, M. L.; Schaller J. M.; Hudgens, J. C.; Brodine, J. A. Methods and Apparatus for Extending the Reach of a Dual Scara-robot Linkage. U.S. Patent 8,016,542, Sep. 13, 2011.

Dede, M. İ. C.; Gezgin E.; Kiper, G.; Mastar E.; Sığırtmaç, T.; Uzunoğlu E. Kinematik Olarak Artıksıl Düzlemsel Lazer Kesme Makinaları Üzerine. *Proceedings of 16. Ulusal Makina Teorisi Sempozyumu*, Erzurum, Turkey 2013, Vol 1, pp 76-85.

Dede, M. İ. C.; Kiper, G.; Uzunoğlu, E. A Macro- Micro Mechanism Design for Laser-Cutting Process. *Proceedings of the 17th International Conference on Machine Design and Production*, Bursa, Turkey, July 12-15, 2016.

Deepak, S. R.; Ananthasuresh, G. K.; Static Balancing of a Four-bar Linkage and its Cognates. *Mechanism and Machine Theory* 2012, 48, 62-80.

Dinçer, Ü. İki Serbestlik Dereceli Prototip Paralel Mekanizmanın Tasarımı ve İmalatı. Master Thesis, İzmir Katip Çelebi University: Turkey, 2017.

Ebert-Uphoff, I.; Gosselin, C.; Laliberté T. Static Balancing of Spatial Parallel Platform Mechanisms-Revisited. *Journal of Mechanical Design 2000*, 122, 43-51.

Engelberger, J. Robotics in Practice, Kogan Page Ltd: London, 1980.

FaroARM, https://www.faro.com/tr-tr/urunler/3d-manufacturing/faroarm/, (accessed May 29, 2019)

Figielski, A.; Bonev, I. A.; Bigras, P. Towards Development of a 2-DOF Planar Parallel Robot with Optimal Workspace Use. *In 2007 IEEE International Conference on Systems*, Montreal, Que, Canada, Oct 7-10, 2007; pp 1562-1566. IEEE Xplore http://www.ieee.org (accessed Feb 9, 2019).

Fischer, O. Über die reduzierten Systeme und die Hauptpunkte der Glieder eines Gelenkmechanismus. *Z. Math. Phys.* 1902, 47, 429-446.

Foucault, S.; Gosselin, C. M. Synthesis, Design and Prototyping of a Planar Three-Degree-of-Freedom Reactionless Parallel Mechanism. Journal of Mechanical Design 2004, 126(6), 992-999.

Gao, F.; Liu, X.; Gruver, W. A. Performance Evaluation of Two-degree-of-freedom Planar Parallel Robots. *Mechanism and Machine Theory* 1998, 33(6), 661-668.

Gosselin, C.; Angeles, J.; A Global Performance Index for the Kinematic Optimization of Robotic Manipulators. *Journal of Mechanical Design* 1991, 113(3), 220-226.

Helm, M. B.; Hesselbach, J.; Mueller, L.; Schulz, H.; Soetebier, S.; Waeckerle, U. Device for Positioning a tool within a predetermined working area. U.S. Patent 7,100,515, Sep. 5, 2006.

Herder, J. L. *Energy-Free Systems; Theory, conception and design of statically balanced spring mechanisms*. PhD Thesis, Delft University of Technology: Delft, 2001.

Herder, J. L.; van der Wijk, V. Delta Robot. U. S. 0103124, 2012.

Hesseleach, J.; Helm, M. B.; Kunzmann, H. Workspace Enlargement for Parallel Kinematic Machines. *CIRP Annals-Manufacturing Technology* 2003, 52(1), 343-346.

Hexcel Prepreg Technology, 2013. https://www.hexcel.com/user_area/content_media/raw/Prepreg_Technology.pdf, (accessed July 29, 2019).

Holy, F.; Steiner, K. Machining System with Movable Tool Head. U.S. 6,161,992, Dec. 19, 2000.

Huang, T.; Wang, P. F; Mei, J. P.; Zhao, X. M.; Chetwynd, D. G. Time Minimum Trajectory Planning of a 2-DOF Translational Parallel Robot for Pick-and-place Operations. *CIRP Annals-Manufacturing Technology* 2007, 56(1), 365-368.

Huang, T.; Liu, S.; Mei, J.; Chetwynd, D. G. Optimal Design of a 2-DOF Pick-and-place Parallel Robot Using Dynamic Performance Indices and Angular Constraints. *Mechanism and Machine Theory* 2013, 70, 246-253.

Ilia, D.; Sinatra, R. A Novel Formulation of the Dynamic Balancing of Five-bar Linkages with Applications to Link Optimization. *Multibody System Dynamics* 2009, 21(2), 193-211.

International Fedaration of Robotics, Robot History. https://ifr.org/robot-history, (accessed Feb 13, 2019).

Johnson, R. H; Milenkovic, V. 1958-62- "VERSATRAN" Industrial Robot- Harry Johnson&Veljko Milenkovic, 2013, cyberneticzoo.com: a history of cybernetic animals and early robots. http://cyberneticzoo.com/early-industrial-robots/1958-62-versatran-industrial-robot-harry-johnson-veljko-milenkovic/, (accessed Feb 10, 2019).

Joubair, A.; Slamani, M.; Bonev, I. A. Kinematic Calibration of a Five-bar Planar Parallel Robot Using All Working Modes. *Robotics and Computer-Integrated Manufacturing* 2012, 29(4), 15-25.

Kiper, G.; Dede, M. İ. C., Uzunoglu, E., Kinematik Olarak Artıksıl Düzlemsel Lazer Kesme Makinası Tasarmı. SanTez Project Report 2-3, Project No: 01668.STX.2012-2, Turkey, 2012-2014.

Kiper, G.; Dede, M. İ. C.; Uzunoğlu, E.; Mastar, E. Bakışımsız Bir Düzlemsel 5R Eyleyicisinin Bağlama Açısına Göre Tasarımı. *Proceedings of Uluslararası Katılımcılı 17. Makina Teorisi Sempozyumu*, İzmir, Turkey 2015, June 14-17.

Kiper, G.; Dede, M. İ. C.; Uzunoğlu, E.; Mastar, Use of Hidden Robot concept for Calibration of an Over-Constrained Mechanism, *Proceedings of the 14th IFToMM World Congress*, Taipei, Taiwan 2015, Oct. 25-30.

Kiper, G.; Dede, M. İ. C., Uzunoglu, E., Methodologies for Increasing the Positioning Accuracy of High-Acceleration Parallel Robots Used in Industrial Applications, TÜBİTAK Project Report 1, Project No: 116M272, Turkey, 2018.

Kumar, V. Instantaneous Kinematics of Parallel-Chain Robotic Mechanisms. *Journal of Mechanical Design* 1992, 114(3), 349-358.

Kurfess, T. R. Robotic and Automation Handbook, CRC: Boca Raton, FL, 2005.

Lee, Y. Y.; Chen, D. Z. Determination of Spring Installation Configuration on Statically Balanced Planar Articulated Manipulators. *Mechanism and Machine Theory* 2014, 74, 319-336.

Lin, P. Y.; Shieh, W. B.; Chen, D. Z. Design of Statically Balanced Planar Articulated Manipulators with Spring Suspension. *IEEE Transactions on Robotics* 2012, 28(1), 12-21.

Liu, X.; Wang, Q.; Wang, J. Kinematics, Dynamics and Dimensional Synthesis of a Novel 2-dof Translational Manipulator. *Journal of Intelligent and Robotic Systems* 2004, 41(4), 205-224.

Li-xin, X.; Yong-gang, L.; Investigation of Joint Clearance Effects on the Dynamic Performance of a Planar 2-DOF Pick-and-place Parallel Manipulator. *Robotics and Computer- Integrated Manufacturing* 2014, 30(1), 62-73.

Lowen, G. G.; Berkof, R. S. Survey of Investigations into the Balancing of Linkages. *Journal of Mechanisms* 1968, 3(4), 221-231.

Lowen, G. G.; Tepper, F. R.; Berkof, R. S. Balancing of Linkages- an uptade. *Mechanism and Machine Theory* 1983, 18(3), 213-220.

McCloy, D. Some Comparisons of Serial-driven and Parallel-driven Manipulators. *Robotica* 1990, 8(4), 355-362.

Menschaar, H. F.; Ariens, A. B.; Herder, J. L. Five-bar Mechanism with Dynamic Balancing Means and Method for Dynamically Balancing a Five-bar Mechanism. W.O. 080846, 2006.

Merlet, J. Parallel Robots: Solid Mechanics and Its Applications, 2nd ed.; Springer: Netherlands, 2006; Vol. 128.

Patel, Y. D.; George, P. M. Parallel Manipulators Applications- A Survey. *Modern Mechanical Engineering* 2012, 3(2), 57-64.

Pierrot, F.; Krut, Sebastien; Baradat, C.; Nabat, V. Par2: A Spatial Mechanism for Fast Planar Two-degree-of-freedom Pick-and-place Applications. *Meccanica* 2011, 46, 239-248.

Pietrantonio, A. F.; Chesna, A.; Elmoli, H.; Gilchrist, U. Dual Scara Arm, U.S. 8,376,685, Feb. 19, 2013.

Pollard, W. L. V. Position Controlling Apparatus. U.S. Patent 2,286,571, June 16, 1942.

Rircard, R.; Gosselin, C.M. On the Development of Reactionless Parallel Manipulators. In Design Engineering Technical (onference and Computers and Information in Engineering Conference: Proceeding of DETC'00 ASME 2000, Baltimore, Maryland, Sept 10-13, 2000.

RP-1AH, 3AH, 5AH- Standard Specifications Manual, http://suport.siriustrading.ro/90.PgSWeb/02.DocArh/DocArhRi.htm (accessed April 9, 2019).

Russo, A.; Sinatra, R; Xi, F. Static balancing of Parallel Robots. *Mechanism and Machine Theory* 2005, 40(2), 191-202.

Schütz, D., Budde, C.; Raatz, A.; Hesselbach, J. Parallel Kinematic Structures of the SFB 562. *Robotic Systems for Handling and Assembly*, Springer: Berlin 2010, 109-124.

Stewart D. A Platform with Six Degrees of Freedom. *Proceedings of the Institution of Mechanical Engineers* 1965, 180(1), 371-386.

Todd, D. J. Fundamentals of Robot Technology, Kogan Page Ltd: London, 1986.

Tsai, L. -W. The Mechanics of Serial and Parallel Manipulators, John Wiley& Sons, Inc: Canada, 1999.

van der Wijk, V. Balancing Low Mass and Low Inertia Addition. *Mikroniek* 2009, 49(3), 60-64.

van der Wijk, V.; Herder, J. L. Guidelines for Low Mass and Low Inertia Dynamic Balancing of Mechanisms and Robotics. *In Advances in Robotic Research* 2009, Springer: Berlin, Heidelberg, 21-30.

van der Wijk, V.; Herder, J. L.; Demeulenaere, B. Comparison of Various Dynamic Balancing Principles Regarding Additional Mass and Additional Inertia. *Journal of Mechanisms and Robotics* 2009, 1(4), 041006.

van der Wijk, V.; Wşj, J. L. Synthesis of Dynamically Balanced Mechanisms by Using Counter-rotary Countermass Balanced Double Pendula. *Journal of Mechanical Design* 2009, 131(11), 111003.

van der Wijk, V.; Krut, S.; Pierrot, F.; Herder, J. L. Generic Method for Deriving The General Shaking Force Balance Conditions of Parallel Manipulators with Application to a Redundant Planar 4-RRR Parallel Manipulator. *In IFToMM 2011 World Congress: The 13th World Congress in Mechanism and Machine Science*, Jun 2011, Guanajuato, Mexico, pp A12-523.

van der Wijk, V.; Demeulenaere, B.; Gosselin, C.; Herder, J. L. Comparative Analysis for Low-mass and Low-inertia Dynamic Balancing of Mechanisms. *Journal of Mechanisms and Robotics* 2012, 4(3), 031008.

van der Wijk, V.; Krut, S.; Pierrot, F.; Herder, J. L. Design and Experimental Evaluation of a Dynamically Balanced Redundant Planar 4-RRR Parallel Manipulator. *The International Journal of Robotic Research* 2013, 32(3), 744-759.

van der Wijk, V, Methodology for Analysis and Synthesis of Inherently Force and Moment-balanced Mechanisms. PhD Thesis, Faculty of Engineering Technology, University of Twente: Holland, 2014.

Wang, L.; Wu, J.; Li, T.; Wang, J; Gao, G. A Study on the Dynamic Characteristics of the 2-dof Redundant Parallel Manipulator of a Hybrid Machine Tool. *International Journal of Robotics and Automation* 2015, 30(2).

Wenger, P.; Gosselin, C.; Maille, B. A Comparative Study of Serial and Parallel Mechanism Topologies for Machine Tools. *International Workshop on Parallel Kinematic Machines:* Proceedings PKM'99, Milan Italy 1999, pp 23-32.

Wu, J.; Wang, J.; Li, T.; Wang, L. Dynamic Analysis of the 2-DOF Planar Parallel Manipulator of a HeavyDuty Hybrid Machine Tool. *The International Journal of Advanced Manufacturing Technology* 2007, 34(3-4), 413-420.

Wu, Y.; Gosselin, C. M. On the Dynamic Balancing of Multi-DOF Parallel Mechanisms with Multiple Legs. *Journal of Mechanical Design* 2007, 129(2), 234-238.

Zhou, H.; Ting, K. Path Generation with Singularity Avoidance for Five-bar Slider-crank Parallel Manipulators. *Mechanism and Machine Theory* 2005, 40(3), 371-384.

APPENDIX A

DETAILS OF COMPOSITE LINKS

Fibermak Company was consulted on the use of composite materials for the links of the mechanism because of the fact that the use of composite materials is not widespread for these types of mechanisms. Fibermak Company is one of the leading companies in Izmir providing composite product support to many corporate companies. The questions posed to the company are as follows:

- What are the alternatives of composite materials for the links of the mechanism?
- How should be tests or analysis to be performed to see the strength of the selected composite material?

First of all, the company proposed carbon-fiber material which is produced from prepreg form. The prepreg is especially used for aerospace and industrial applications to obtain high strength material with light weight. For the mechanism which is selected for the thesis has 2-dof planar motion. Therefore, the links of mechanisms are under the influence of bending and tensile forces. For this reason, fabric woven (0° - 90°) carbon-fiber composite material was selected. In addition, the company mentioned two types of fabric woven (0° - 90°) carbon-fiber composite material in terms of cross-section which are tube and plate.

Figure A.1. A composite link for a high acceleration robot.

The composite tube which can be seen in Figure A.1 is shown as an example. It is manufactured for a high acceleration robot which is available in a company in Turkey. It was connected to two metal parts with a special glue (which is used for connection of metal with composite parts). In this connection, the composite tube is inserted into the metal parts. Otherwise, it is more difficult to achieve a combination due to the diameter tolerance of composite tube caused by the production method.

The composite plate which can be seen in Figure A.2 can be also used if the links of mechanism is designed with rectangular cross-section. It can be machined with a CNC router. It can also be produced from mold. This way is better option than machining with CNC router. Because when the parts are machined with CNC router, the composite structure of the material can be damaged due to small size of the link parts. Also, the links designed from the plate are heavier than the links designed as carbon-fiber tubes. In addition, both options are more costly according to use of standard composite tube. Due to these reasons use of composite tubes is preferred over use of composite plates for the links.

Figure A.2. A composite plate.

Composite materials have different matrices, fibers, woven structures, manufacturing methods and etc. Therefore, it is difficult to calculate mechanical properties of composite materials. For this reason, the company stated that the analysis of composite material is quite complex. If the composite tube which is available in markets is used, the available information of mechanical properties can be used for the fabric

woven (0° - 90°) carbon-fiber composite material. It was stated that it would be sufficient to make the analysis with the maximum forces affecting the links.

As a result, composite tubes are selected for six links of the mechanism except the links which are connected to the actuators. It is decided to test the links within facilities of the university and basically perform the static analysis.

Firstly, a preliminary prototype of the composite link with Al 5000 series metal parts was manufactured to perform some tests. A tensile test is performed with MTS 647 Hydraulic Wedge Grips device in Composite Research Laboratory of Mechanical Engineering Department at IzTech. In this way, bonding of metal parts with composite tubes has been tried and it is seen how the composite tube-metal combination reacted to higher tensile forces.

The bonding process was carried out with use of epoxy glue after manufacturing the composite tubes (with 1 mm thickness, inner-outer diameter: 14 mm -16 mm) and metal parts. A jig (Figure A.3 (a)) was produced to ensure that the joint axes are parallel to each other. Firstly, epoxy glue is applied to the composite tube and two metal parts, separately. The parts are assembled to each other and split pins are mounted to the holes. Then the link is placed on the jig to dry (Figure A.3 (b)).

The tensile test is applied with forces up to 4000 N. No separation between metal parts and the composite tubes was observed. Tensile test setup with the device and test results are shown in Figure 4.A (a)-(b). As can be seen in the stress-strain graph, the link shows a linear behaviour and its elastic modulus is approximately 42 GPa.

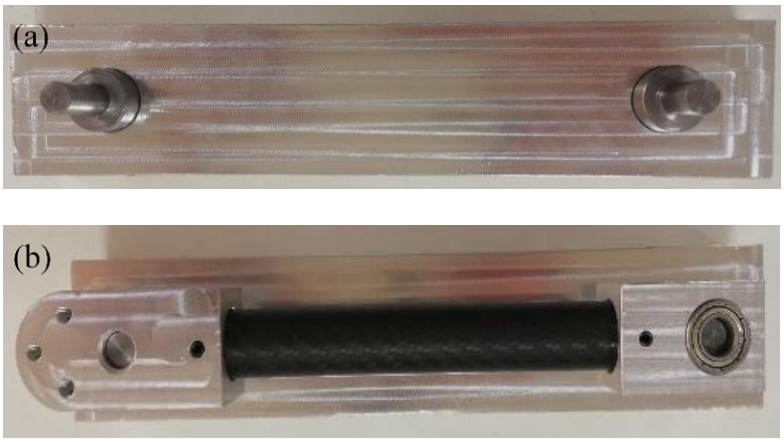

Figure A.3. (a) A jig for the bonding process, (b) the composite link on the jig.

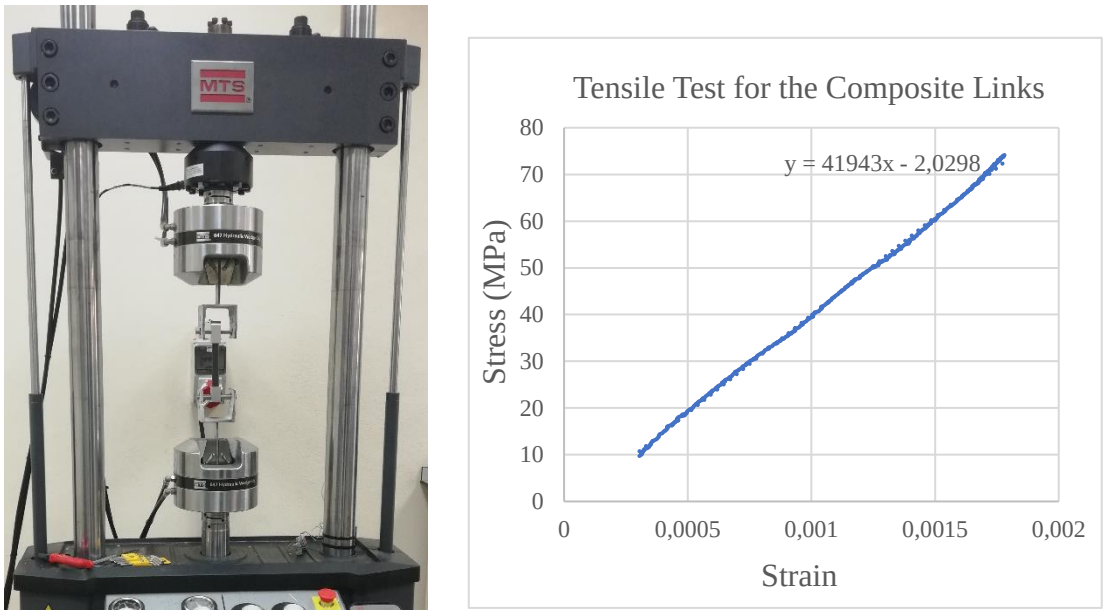

(a) (b)

Figure A. 4. (a) Tensile test setup, (b) stress-strain graph of the composite link.

The static force analysis is performed to obtain reactions of the link to applied force in terms of elongation. APEX (finite element analysis program) and ADAMS (multi-body dynamics simulation program) are used to obtain elongation of the link. The methodology is as follow:

1) Modelling the link using APEX.
2) Preparing file extension (as a mnf. file) of the flexible model of link parts to transfer from APEX to ADAMS.
3) Assembling with the flexible model of link parts and the mechanism is run for the static analysis on ADAMS environment.

The Solidworks assembly file of the link is used to create APEX model. The mechanical properties of Al 5000 series for the metal parts is taken from the literature. The catalogue of Hexcel company (HexPly Prepreg Technology, 2013) is used to decide the mechanical properties of the carbon-fiber composite tube. A ratio is calculated between the obtained elasticity modulus of the link (42 GPa) from the test and the elastic modulus in the Hexcel catalogue. The rest of the mechanical properties of the link is calculated with multiplying this ratio (Table A.1) for describing in APEX. Solidmesh is used for aluminium metal parts on the APEX environment. For the composite tube, a surface is created to locate layers oriented by 0° - 90°. Glue patch tolerance tool is used

to model the glue which is used for the connection between the composite tube and the metal parts (in Figure A.5).

Table A.1. Mechanical properties of carbon-fiber composite material.

Elasticity Structure	2D Orthotropic	
Elasticity Modulus		
Ex	45398	MPa
Ey	35000	MPa
Shear Modulus		
Gxy	3500	MPa
Gyz	3500	MPa
Gzx	3500	MPa
Poisson Ratio	0.05	
Density	1.59×10^{-6}	kg / mm^3
Structural Damping Ratio	4×10^{-4}	
Fracture Limit Stress		
Tensile (X)	685	MPa
Tensile (Y)	600	MPa
Compression (X)	600	MPa
Compression (Y)	550	MPa
Shear in XY plane	80	MPa

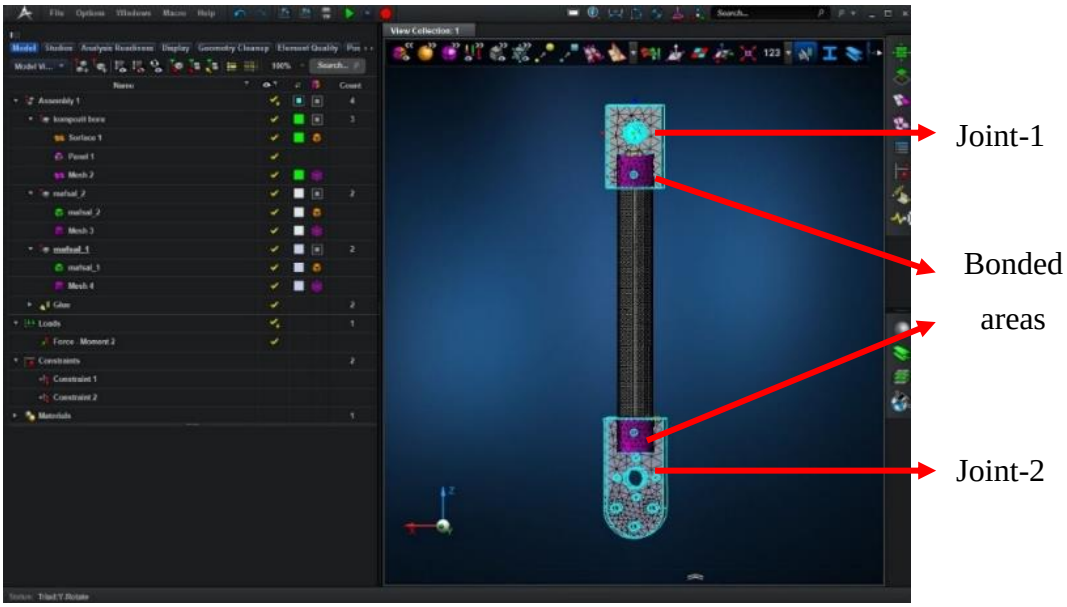

Figure A.5. APEX environment.

It is necessary to describe interface points for the flexible link model. These interface points, which are pointed with indicated red arrows in Figure A.6, provide easier assembly of link parts on the ADAMS environment.

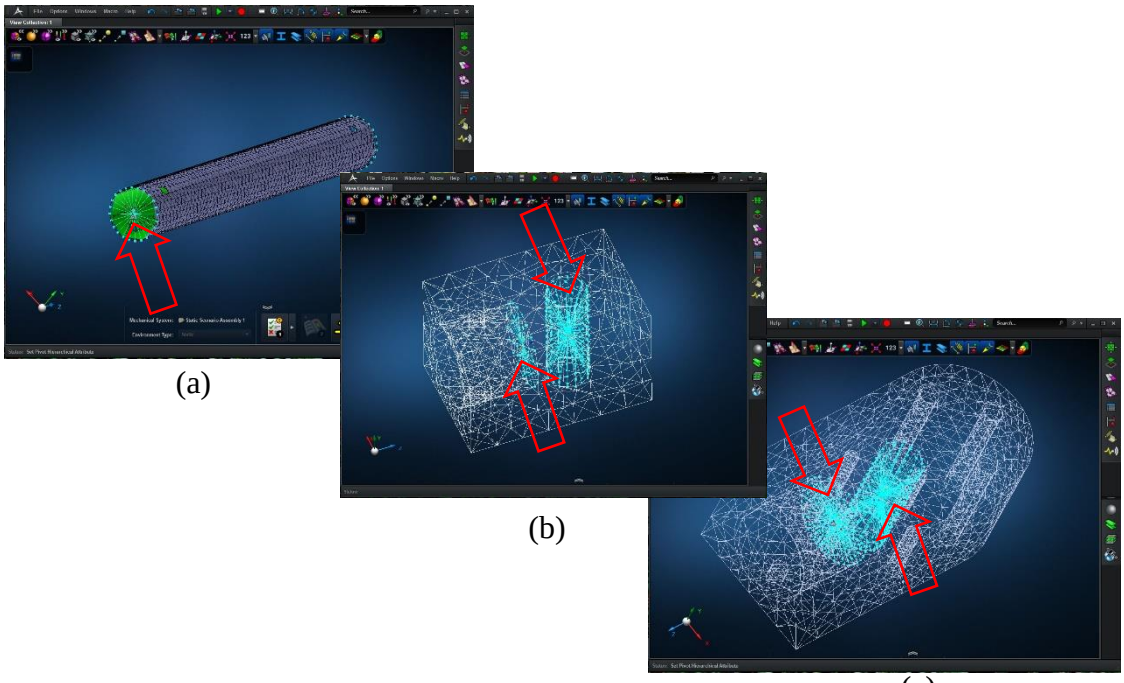

(a) (b) (c)

Figure A.6. Interface points of (a) the composite tube, (b) Joint-1, (c) Joint-2.

Simulation of the static analysis is performed in ADAMS for one link with bending and tensile forces. The coordinate system is shown in Figure A.7. When the tensile force is applied on the z- axis, the bending force is applied on the x-axis. The linear increase in the obtained results of elongation is obtained with the increase of forces.

The result of tensile forces shows a linear behaviour as seen in Figure A.8 (a). The tensile force is applied up to 2000 N and the elongation is obtained as 0.14 mm. The slope of graph which is given in Figure A.8 (a) gives stiffness coefficient as approximately 15500 N/mm. The result of bending forces shows an approximate linear behaviour as seen in Figure A.8 (b). The bending force is also applied up to 2000 N and the elongation is obtained as 26.9 mm. The slope of graph (in Figure A.8 (b)) gives stiffness coefficient as approximately 73.8 N/mm. Due to the results obtained for bending forces, the thickness of the carbon-fiber tubes are increased for the main mechanism.

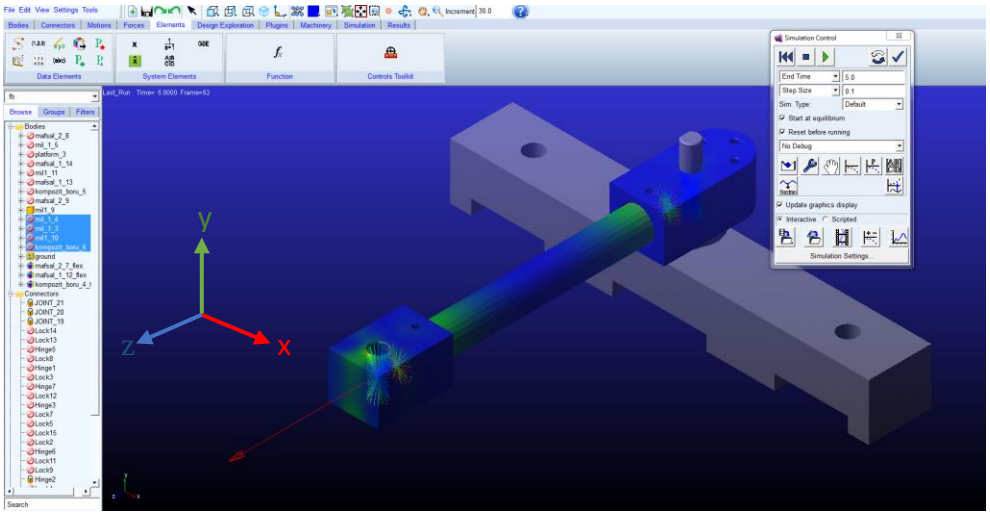

Figure A.7. Simulation of one link on ADAMS environment.

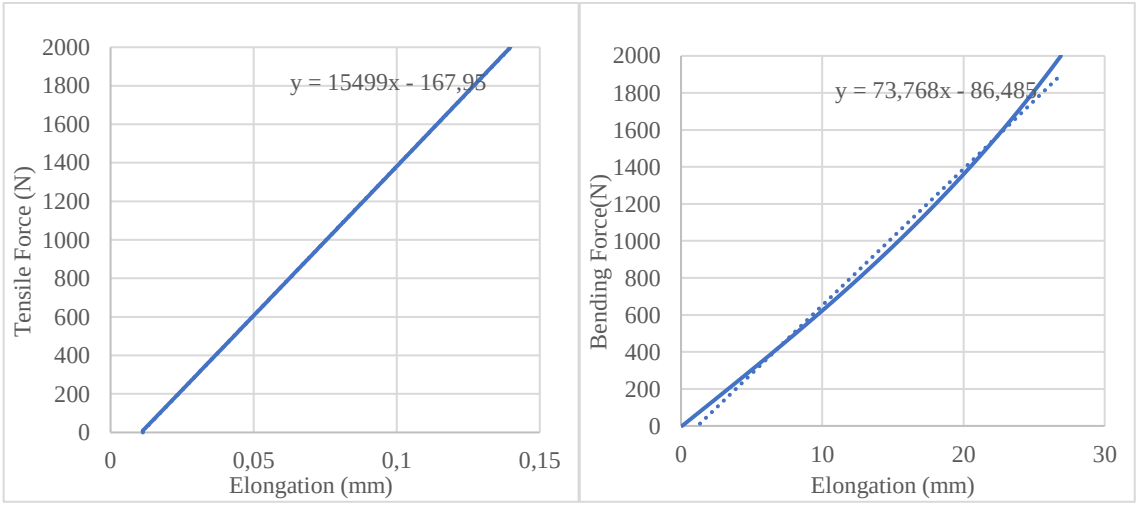

(a) (b)

Figure A. 8. The curve of: (a) tensile force-elongation on the z-axis, (b) bending force-elongation on the x-axis.